ICE SHELF MELT RATES AND 3D IMAGING

By

©2015
Cameron Scott Lewis

Submitted to the graduate degree program in Electrical Engineering and Computer Science and the Graduate Faculty of the University of Kansas in partial fulfillment of the requirements for the degree of Doctor of Philosophy.

_____
Chairperson: Prasad Gogineni

_____
Chris Allen

_____
Carl Leuschen

_____
Fernando Rodriguez-Morales

_____
Rick Hale

Date Defended: May 8, 2015

This Dissertation Committee for Cameron Lewis certifies that this is the approved version of the following dissertation:

Ice Shelf Melt Rates and 3D Imaging

_____

Chairperson: Prasad Gogineni

Date Approved:

Abstract

Ice shelves are sensitive indicators of climate change and play a critical role in the stability of ice sheets and oceanic currents. Basal melting of ice shelves plays an important role in both the mass balance of the ice sheet and the global climate system. Airborne- and satellite-based remote sensing systems can perform thickness measurements of ice shelves. Time-separated repeat flight tracks over ice shelves of interest generate data sets that can be used to derive basal melt rates using traditional glaciological techniques. Many previous melt rate studies have relied on surface elevation data gathered by airborne- and satellite-based altimeters. These systems infer melt rates by assuming hydrostatic equilibrium, an assumption that may not be accurate, especially near an ice-shelf's grounding line. Moderate bandwidth, VHF, ice-penetrating radar has been used to measure ice-shelf profiles with relatively coarse resolution. This study presents the application of an ultra-wide bandwidth (UWB), UHF, ice-penetrating radar to obtain finer resolution data on the ice shelves. These data reveal significant details about the basal interface, including the locations and depth of bottom crevasses and deviations from hydrostatic equilibrium. While our single-channel radar provides new insight into ice-shelf structure, it only images a small swatch of the shelf, which is assumed to be an average of the total shelf behavior. This study takes an additional step by investigating the application of a 3D imaging technique to a data set collected using a ground-based multi-channel version of the UWB radar. The intent is to show that the UWB radar could be capable of providing a wider swath 3D image of an ice-shelf. The 3D images can then be used to obtain a more complete estimate of the bottom melt rates of ice shelves.

Acknowledgements

I want to thank my husband, Jimmy, for his unwavering love, support, enthusiasm, and patience. I would not have made it through all the field deployments, late nights in the lab, and dissertation writing marathons without his support and encouragement. I owe my success to him. I want to thank my parents, Angelia and Jeff, for their love and encouragement during my entire educational career. My parents have always pushed me to challenge myself with unconditional support.

I want to thank my advisor and mentor, Dr. Prasad Gogineni, for guidance, support, and extreme patience through my entire graduate education, for this I am extraordinarily grateful. Dr. Gogineni has afforded me many experiences that I will never forget, including the opportunity to travel to Greenland and Antarctica. I want to thank my mentor, Dr. Fernando Rodriguez-Morales, for his guidance and support. Fernando has always been there to answer my questions (even dumb ones) and offer thoughtful advice.

I want to thank my colleague John Paden for believing in me when I was a young undergraduate researcher. John helped shape my beginnings at CReSIS and has always provided me with sound advice and guidance through my studies. I want to extend a special thank you to my friends and colleagues Ben Panzer, Theresa Stumpf, and Logan Smith for their contributions to my research. The support (both physical and emotional) we give each other as fellow students is critical to our success, both in school and beyond. I also want to thank Jenna Collins and Rachel James for helping edit this dissertation document, Judith Riley for her tremendous support preparing for field deployments (and listening to my ramblings), and the

rest of the CReSIS administrative staff, past and present, for their hard work that make research like this possible.

Finally, I want to thank all the members of my committee for their support and guidance through my dissertation and my entire graduate education.

Table of Contents

Table of Figures

Chapter 1: Introduction

The work presented in this dissertation focuses on remote sensing tools and techniques for imaging ice shelves, estimating their thickness, and inferring basal melt rates. Ice shelves are sensitive indicators of climate change and play a critical role in the stability of ice sheets and oceanic currents. Basal melting of ice shelves plays an important role in both the mass balance of the ice sheet and the global climate system [Doake, 2001; Corr and others, 2002]. While over 80% of the Antarctic grounded ice drains through ice shelves, it is not fully understood how ice shelves regulate the flow of ice off the land on a continental scale [Doake, 2001; Pritchard and others, 2012]. Ice shelves are thought to have a buttressing effect on nourishing ice streams [Horgan and others 2011], directly regulating their flow velocities, which are sensitive to the ice-shelf's size [Rott and others, 2002] and thickness [Dupont and Alley, 2005].

Catastrophic ice-shelf collapse has the potential to generate unchecked ice-sheet mass loss [Schoof, 2007]. Basal melt rates are a function of local ocean temperatures and shelf thickness and are subject to positive feedback: warmer ocean temperatures increase basal melt and the thinning ice leads to greater warm-water permeation and accelerated shelf retreat [Jacobs and others, 2011; Rignot and Jacobs, 2002]. Significant ice-shelf retreat in the Pine Island Glacier region of West Antarctica has led to increased glacial flow rates [Joughin and others, 2010]. Ice shelves in other location around Antarctica also appear to be thinning [Shepherd and others, 2010]. Also, basal melting and refreezing influence the development of Antarctic Bottom Water, which helps drive the oceanic thermohaline circulation [Doake, 2001; Orsi and others, 1999], a critical component of the global climate system.

Basal melting is estimated to account for more than 20% of the ice-shelf mass loss; however, uncertainty in the individual parameters that feed this cumulative estimate could result in an error as large as 50% in the estimated results [Jacobs and others, 1992]. Oceanographic measurements can be made where the ice-shelf meets open ocean, the ice front, to estimate basal melt rates. These measurements use conservation of heat and salinity to determine the flux of freshwater between the ocean and the ice-shelf over a broad region. These measurements are made under the assumption that the water beneath the ice-shelf is not experiencing a flux of heat or salt during the period of observation [Corr, 2002], an assumption that is difficult to satisfy in real-world conditions.

Traditional glaciological techniques can also be employed; relying on conservation of mass and assuming the ice is incompressible, the mass balance can be defined as:

$$\frac{\partial H}{\partial t} + \nabla \cdot \mathrm{H}\vec{v} = \dot{M}_s - \dot{M}_b$$

Where H is the ice thickness, **v** = (v_x,v_y) is the two-dimensional velocity vector, $\dot{M}_s$ is the net surface mass balance (expressed as a rate, positive for accumulation, negative for ablation), and $\dot{M}_b$ is the net basal mass balance (expressed as a rate, positive for melting, negative for freezing). The velocity vector assumes that the velocity is constant or averaged through the entirety of the ice column. The spatially averaged basal melt rate can be estimated knowing: the average ice-shelf thickness, the horizontal ice flux into and out of the region of interest, and the surface accumulation rate. Error in the assumed or measured average accumulation, ablation, velocity, or thickness contribute to error in the estimated basal melt rate and these errors can grow as the area of interest or the measurement interval is reduced [Corr, 2002].

Boreholes are a method for direct and accurate measurement of basal melt rates. However, these *in situ* measurements are difficult and expensive to execute, as evidenced by their scarcity, and only provide point estimates [Corr, 2002]. Using this method to provide a wide spatial and temporal coverage is impractical. Significant temporal and spatial variability in melt rates estimated from boreholes [Grosfeld and others, 1994] would likely invalidate the assumptions needed for the oceanographic and glaciological techniques described above.

Measurement of basal melt rates using remote sensing platforms can take on many forms. As with boreholes, *in situ* ground-penetrating radar measurements are difficult and expensive to perform due to the remoteness of the locations of interest. While ground-based radar systems have the potential to cover a wider area with fine spatial resolution, they still only provide localized coverage. Coverage issues can be overcome by using an airborne- or satellite-based platform. While wide coverage of the whole ice-shelf is desired, there is particular interest in the thickness and melt rate measurements close to the grounding line [Griggs and Bamber, 2011]. Airborne platforms excel in this realm, balancing the need for wide coverage with the ability to achieve fine spatial resolution over grounding-line regions where surface slopes are the largest [Griggs and Bamber, 2011]. The relatively coarser spatial resolution provided by satellite-based instruments leads to interpolation errors of the surface elevations in the grounding-line regions [Griggs and Bamber, 2011; Bamber and others, 2009]. For example, the European Remote-sensing Satellite (ERS-1) radar altimeter has an effective along-track spacing of 335 m and a cross–track spacing of 2 km [Lingle and others, 1990]; in comparison, the Ice, Cloud, and Land Elevation Satellite (ICESat) Geoscience Laser Altimeter

System (GLAS) has a finer along track spacing of 172 m, but a much coarser cross-track spacing of about 20 km [Schultz and others, 2005].

Airborne- and satellite-based remote sensing systems can perform thickness measurements indirectly. Ground-penetrating radars measure the time difference between the surface and basal interfaces. To convert this time to a thickness requires knowledge of the density of the intervening firn and ice, specifically the thickness and density profile of the firn; this is often referred to as the firn correction. Radar or laser altimeters are used to measure surface elevation, and thickness can be inferred using the principle of hydrostatic equilibrium, geoid models, and tide models [Bamber and Bentley, 1994; Griggs and Bamber, 2011]. In recent decades, improved estimates of firn densities and the geoid make accurate estimates of ice thickness via remote sensing methods a viable prospect [Griggs and Bamber, 2011]; however, the hydrostatic equilibrium assumption may breakdown in close proximity to the grounding line [Griggs and Bamber, 2011] where the most accurate estimates are desired.

The work presented in this dissertation addresses the need for a method that can provide an accurate estimate of ice-shelf basal melt rates with fine spatial and temporal resolution. This investigation has three primary components: (1) development and refinement of a fine-resolution radar system; (2) the demonstration of a technique for estimating ice-shelf basal melt rates using airborne radar data while separating the effects of ice motion and surface accumulation; and (3) the demonstration of three-dimensional imaging of bed topography via parametric processing techniques, and the evaluation of the efficacy of the processing algorithm using overlapping data lines. This work also sets an important precedent for future

data collection efforts on surface and airborne platforms, potentially including unmanned aerial system (UAS).

The dissertation is organized as follows. Chapter 2 presents background information for this investigation, including a brief discussion of previous remote sensing system used for ice-shelf thickness and melt rate measurements, a review of reported melt rates and the time cycles over which they were measured, and a discussion of the minimum radar system requirements to measure expected melt rates. Chapter 3 provides a description of the radar system developed and a discussion of its performance. Chapter 4 focuses on a technique for estimating ice-shelf basal melt rates. Chapter 5 discusses the generation and validation of 3D imagery of the ice-basal interface. Finally, chapter 6 presents a summary, concluding remarks, and recommendations for future work.

Chapter 2: Background

Remote sensing techniques have been adapted over the past few decades to improve the estimation of ice-shelf thickness and basal melt rates. Satellite-based sensors have been used extensively to monitor ice-shelf integrity and thickness. This constellation of instruments include: a K_u-band radar altimeter aboard the European Remote Sensing Satellites (ERS-1 and ERS-2) [Shepherd and others, 2004], a dual band (K_u-band and S-band) radar altimeter aboard Envisat [ESA, 2007], the SAR Interferometer Radar Altimeter (SIRAL) aboard CryoSat-2, the Geoscience Laser Altimeter System (GLAS) aboard the Ice Cloud and Land Elevation Satellite (ICESat) [Zwally and others, 2002], and the Gravity Recovery and Climate Experiment (GRACE). Ice-shelf thickness can be estimated from surface elevation data collected via satellite, but requires the assumption that the shelf is floating in hydrostatic equilibrium [Bamber and Bentley, 1994] and *a priori* knowledge of the firn density profile, elevation of the geoid [Griggs and Bamber, 2011], and surface accumulation.

Even with newly available, ground-truthed density and geoid estimates, satellite-data derived ice-shelf thickness (and by extension, ice-shelf melt rates) suffers from relatively course spatial resolution and interpolation-induced error [Schultz and others, 2005; Bamber and others, 2009]. Finer spatial resolution can be achieved using airborne-based radar and laser instruments at the expense of wide coverage; however, this typically is not an issue as aircraft can focus their data collection efforts on specific ice shelves that have limited extent. Ice-shelf thickness and basal melt rate estimates derived from airborne altimetry still suffer from the same limitations as satellite altimetry-derived estimates that require the assumption of

hydrostatic equilibrium and *a priori* knowledge of firn density, geoid elevation, and surface accumulation.

Densely-gridded i*n situ* borehole and radio-echo sounding (RES) measurements still provide the most accurate thickness and melt-rate estimates [Griggs and Bamber, 2011]. Direct measurements of thickness and melt rates are most accurate via boreholes, but these measurements are sparse. Non-destructive RES measurements are the next best solution, only requiring *a priori* knowledge of firn density and net surface accumulation. The observation of bottom melting via RES measurements has been noted as early as the 1970s. Neal [1979] made note of distinguishing regions of basal melting from airborne RES measurements of the Ross Ice Shelf using a pulsed, very high frequency (VHF) radar. Corr and others [2002] appear to be the only RES experiment conducted to date with specific interest in precise measurements of ice-shelf melt rates. This ground-based, stepped-frequency, vector network analyzer (VNA)-based system measured thickness changes at a fixed point by comparing the phase history of radar pulses reflected from the base of the ice-shelf. Only a pair of wide-beam antennas were used (one for transmit, one for receive), meaning that the measured thickness change was an average over a wide footprint.

Some measured and inferred ice-shelf melt rates have been reported in the literature. Examples are presented here to help establish boundaries on typical ice-shelf characteristics. These characteristics will help drive the basic radar system requirements needed to accomplish the goal of this study. Ice shelves exist with in a wide range of circumstances. The Ross and Ronne-Filchner ice-shelves in Antarctica are expansive, relatively stable, fed by numerous glacial streams, and are underlain by a relatively cold ocean current atop a continental shelf. By

contrast, the Petermann glacier ice-shelf in northern Greenland extends from the end of a single glacial stream, lies with a relatively narrow fjord, and is underlain by a relatively warm ocean current fed by the neighboring Nares Strait. Table 1 presents some typical ice-shelf thickness and melt rates.

Table 1. Melt rates and thickness for select ice shelves

Region	Melt Rate	Thickness	Reference
George IV, Southern Antarctica peninsula	0.091 ± 0.003 m, measured over 12 days 2.78 ± 0.08 m/yr equivalent	450 m average	Corr and others, 2002
Rutford Ice Stream grounding line, Ronne-Filchner ice shelf	1-4 m/yr	1.4 km average	Jenkins and Doake, 1991
Ronne-Filchner ice shelf, 30 km from ice front, 50 km NW of Filchner Station	1.41 ± 0.45 m/yr, measured at a single point over 2 years 1.5 ± 0.15 m/yr, the mean of measurements from a 10 km square grid over 26 days	240 m average	Grosfeld and others, 1992
Pine Island Glacier	44 ± 6 m/yr at grounding line	1 km average	Rignot and Jacobs, 2002
Petermann Glacier	30 m/yr at grounding line 10 m/yr at ice front	300 m average	Rignot and Steffen, 2008
Petermann Glacier	10-13 m/yr, spatially averaged	300 m average, 600 m maximum	Münchow and others, 2014
Ross Ice Shelf, near Mercer ice stream grounding line	2.5 ± 0.7 m, measured over 1 month	900 m average	Anandakrishnan and others, 2014 (AGU, unpublished)

A variety of techniques were used to measure thicknesses and melt rates. Corr and others [2002] used a phase-sensitive, VNA-based radar, as discussed above. Grosfeld and others [1992] used a combination of temperature sensors and time-domain reflectometry (TDR) cable pairs inserted into boreholes. Rignot and Jacobs [2002] and Rignot and Steffen [2008] inferred shelf thickness and melt rates using mass conservation techniques and assuming steady-state

conditions, relying on repeat satellite-altimeter data. Studies by Jenkins and Doake [1991], Munchow and others [2014], and Anandakrishnan and others [2014] used ice penetrating radar, performing repeat *in situ* measurements within the same field season or relying on annual repeat airborne measurements.

While no single radar system will be able to capture the entire range of ice-shelf characteristics, Table 2 summarizes the science and radar parameters proposed to allow the radar system to cover the widest reasonable range of possibilities while providing advancement over previous measurements.

Table 2. Measurement goals and translated radar parameters.

Science Parameter	Measurement Goal	Translated Radar Parameter
Ice thickness	Up to 1 km, from 500 m airborne platform altitude	Maximum PRF: 58 kHz Minimum P_t: 30 dBm
Melt rate	As small as 1 m change between measurements with a 1 year repeat cycle	Minimum BW: 85 MHz Minimum P_t: 30 dBm
Ice-surface spatial resolution	Finer than 1 km satellite data-based DEMs [Bamber and others, 2009; Griggs and Bamber, 2009]	SAR capable Cross-track array and post-processing beam steering

The proposed radar parameters are meant to reflect goals to collect data in the most challenging circumstances. An ice thickness of 1 km was chosen to cover the average grounding line depth of major ice shelves in Antarctica, including the Ross Ice Shelf (RIS) and the fast-flowing Pine Island glacier. This study will leverage the CReSIS UHF radar with a center frequency of 750 MHz and a pulsed-chirp transmission scheme. This basic system topology was found to be adequate for this study. Previous studies conducted by Kanagaratnam [2002] found that this frequency provided adequate firn and ice penetration with significant backscatter from internal layering and shallow basal interfaces, allowed for a wider

programmable bandwidth range than ice-penetrating VHF radars, fit into a frequency range that did not interfere with typical communication and navigation equipment found aboard science aircraft (e.g. NASA P-3 Orion), and facilitated system design due to the availability of cellular telephone commercial-off-the-shelf (COTS) components.

For the timing analysis, the most complex scenario was assumed: 1 km thick ice (ε_r = 3.15) and a 500 m platform altitude. Assuming a 2-µs pulse width, the maximum pulse repetition frequency that provides an adequate receive time window is approximately 58 kHz. Basic link budget analyses presented by Lewis [2010] and Lewis and others [2015] show that a minimum transmit power of 30 dBm (1 W) is sufficient to receive a 10 dB signal-to-noise ratio (SNR) return from the basal interface assuming the maximum expected depth and platform altitude. A one meter range resolution in ice with an accuracy of 20 cm should be a sufficient threshold for detecting melt rates of one meter with a one year measurement repeat cycle. For areas that have exhibited extreme melt rates, such as Pine Island Glacier and the Mercer ice stream region of RIS, much shorter measurement repeat cycles of one month could be used. A basal echo return with 10 dB SNR is sufficient to provide 20-cm accuracy.

A moving platform and cross-track antenna array will allow for 3D imaging of basal topography from single-pass data through synthetic aperture radar (SAR) processing and parametric cross-track direction of arrival (DOA) techniques. A ground-based system with a 12 or 16 phase-center array will be used. Shendkar and others [2013] have shown that arrays of 8 elements or more provide the best results from parametric DOA algorithms.

Chapter 3: Radar system

This chapter presents an overview of the radar system developed and employed for this investigation. The design considerations and requirements are described along with a discussion of its integration with different airborne and surface-based platforms in both single and multi-channel configurations.

3.1 Hardware description

A custom ultra-wideband chirped-pulse radar was designed and built with 300 MHz of bandwidth at a center frequency of 750 MHz. It was designed to profile interfaces within polar firn and glacial ice. Analysis of field data revealed the radar was capable of sounding shallow ice and ice shelves. Table 3 provides a summary of pertinent nominal radar parameters. Figure 1 shows a simplified block diagram of the system.

Table 3. Summary of important radar system parameters

Parameter	Value	Unit
Center frequency	750	MHz
Bandwidth	300	MHz
Waveform	Pulsed Chirp	
Pulse duration	2.048	µs
Peak transmit power	5	W
Pulse repetition frequency (PRF)	50	kHz
Sampling frequency	1	GHz
Coherent integrations	1280	
Samples per trace	10000	
Data rate	3.9	MB/s
ADC dynamic range	44	dB
Post-processing dynamic range	103	dB
Antenna element	Twin Otter: Vivaldi P-3: Elliptical dipole Surface: PCB dipole	
Antenna cross-track 3 dB beamwidth	Vivaldi: 46 Elliptical dipole: 20 PCB dipole: 60	degrees
Antenna polarization	VV	

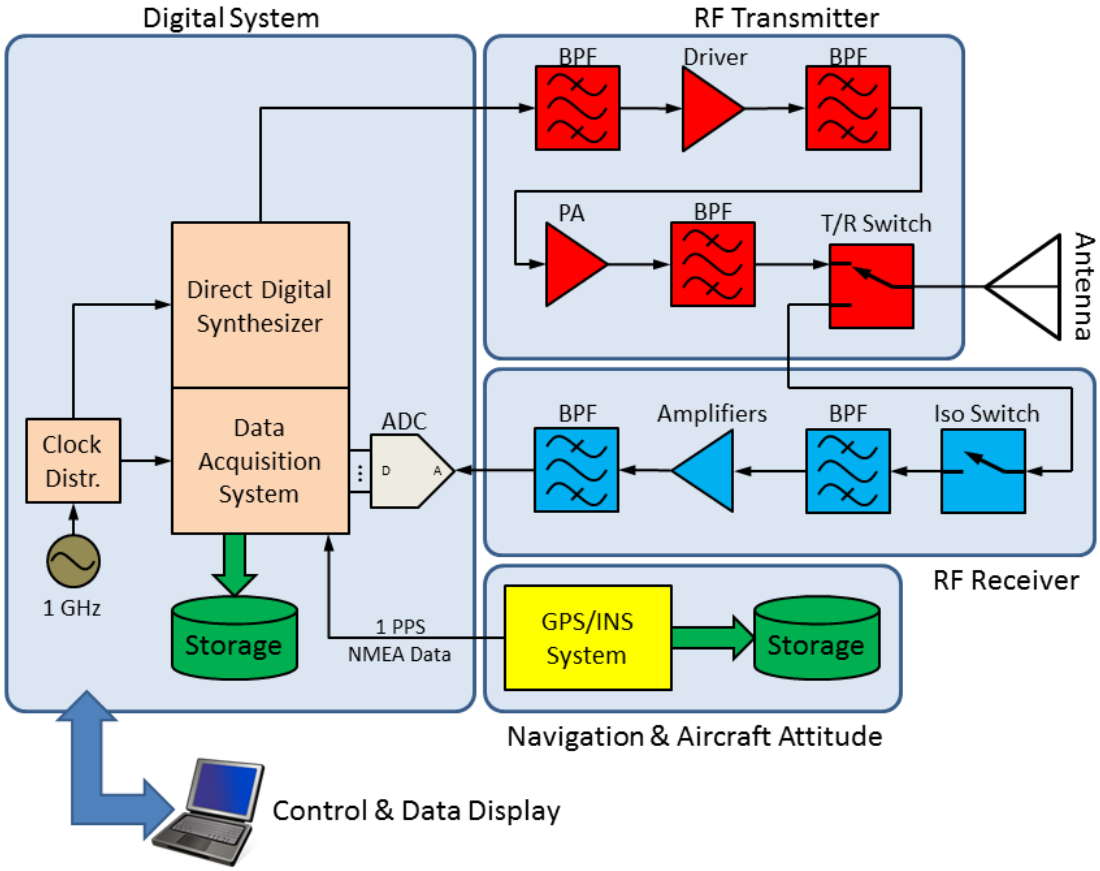

Figure 1. Airborne single-channel system block diagram.

The frequencies of operation were selected to obtain fine resolution without interference with the communication and navigation equipment aboard the NASA P-3 aircraft [Kanagaratnam, 2002]. A pulsed-chirp transmission scheme obtained pulse compression gain while allowing for single-antenna operation by using a transmit/receive (T/R) switch. The pulse repetition frequency (PRF) provided an unambiguous range of one kilometer in ice while accounting for the pulse width, software hold times, and platform altitude. The available space on the aircraft guided the antenna design choices. A high input-bandwidth analog-to-digital converter (ADC) allowed for the direct digitization of received returns by means of band-pass sampling [Vaughan and others, 1991]. This eliminated the need for the synthetic range

profiling [Lord and Inggs, 1996; 1997] techniques used in previous revisions [Lewis, 2010]. The received signals were pulse-compressed digitally to generate time and range profiles.

When operating in single-channel mode, the radar system is composed of a user interface, a digital section, an analog RF section, and the antennas. When operating in multi-channel mode, a switch section is added. Global positioning and inertial navigation (GPS/INS) information is ingested from an external system. Aboard the Twin Otter, a NovAtel SPAN-CPT GPS+IMU system was used. Aboard the NASA P-3, the navigation and orientation data were provided by an Applanix POS AV 510 [Rodriguez-Morales and others, 2013]. For ground-based experiments, a simple Trimble GPS module was employed.

3.1.1 Digital section

The digital section comprises the clock distributor, waveform and timing signal generator, data acquisition, and high-capacity data storage. The clock distributor provides a 1-GHz, low phase-noise sampling clock signal to the remaining digital hardware. The waveform generator produces the transmit chirp using an off-the-shelf Direct Digital Synthesis (DDS) chip controlled by a field programmable gate array (FPGA). The waveform generator produces a baseband chirp over the frequency range of 100-400 MHz. The 900-600 MHz image frequency is selected using a reconstruction filter located in the RF section. The chirp amplitude is weighted to compensate for the sinc roll-off, amplitude variations through the transmitter, receiver, and the insertion loss of the antennas. A Tukey window is applied to the waveform envelope to reduce range sidelobes [Kowatsch and Stocker, 1982]. The data acquisition (DAQ) subsection front-end employs ADC with 7 effective bits and 840-mVpp (2.5 dBm) input range, operated at a 1-GHz sampling

frequency. Bandpass sampling [Vaughan and others, 1991] is used to directly digitize the received UHF chirp. Following digitization, the data are coherently averaged and streamed to the control computer; they are tagged with GPS/INS data and radar system parameters and written to a storage device, typically a solid-state hard drive. The computer hosts a graphical user interface (GUI) that allows the operator to control the radar parameters. Samples of the data stream received by the computer are pulse-compressed, and an auto-refreshed amplitude-scope (a-scope) and scrolling echogram are displayed to the operator in near real time, allowing the operator to evaluate the radar system performance. The computer and DAQ are PCI eXtensions for Instrumentation – Express (PXI-e) modules housed in a National Instruments (NI) chassis.

3.1.2 Analog RF section

The transmitter comprises a driver amplifier stage, a power amplifier (PA), and a T/R switch. The driver amplifier circuit begins with the aforementioned reconstruction filter, followed by a series of off-the-shelf cascadable gain-blocks. Additional bandpass filters follow the driver amplifier stage to suppress out-of-band noise and spurious frequency components. A 10-watt peak-power PA module further amplifies the conditioned signal for transmission, followed by a medium-power bandpass filter used to suppress higher-order harmonics produced by the PA. The final stage is a medium-power T/R switch, implemented with two Gallium Nitride (GaN) single-pole, double-throw (SPDT) switches. The use of a GaN switch allows for faster switching times, lower control voltage requirements, and video feed-through signal levels (in comparison with high-power

switches based on PIN diodes). The two switches are configured to provide 40 dB of isolation during transmission and 70 dB of isolation during receive.

The receiver is comprised of an isolation switch and an amplifier stage. The isolation switch follows the receive-half of the T/R switch. This switch protects the receiver chain from damage by signals that leak across the T/R switch during transmit mode and reduces video feed-through, effectively providing an isolation of 90 dB between transmit and receive paths. A low-noise amplifier and bandpass filter condition the signal prior to reaching the ADC. Control signals for the T/R and isolation switches are generated by the waveform and timing signal generator.

3.1.3 Multi-channel switch section

As development time and cost are always a factor, the single-channel radar system was modified to accommodate multi-channel data collection through the addition of a multiplexer (mux) at the receiver front-end. To increase the number of virtual phase centers, the switch was added at the output of the transmitter to accommodate transmission from the left and right side of the antenna array, commonly referred to as "ping-pong" transmission. Aboard the NASA P-3, a four-element cross-track array is used; the outer two elements are used for transmit and receive, and the inner two elements are used for receive only. This results in seven unique phase centers. Figure 2 is a simplified block diagram of the airborne multi-channel system.

The introduction of the receive-mux and transmit-choose switches requires additional control signals. The T/R and isolation switch-control signals are generated by the waveform and timing signal generator and do not change from pulse to pulse, both in single and

multi-channel mode. The receive-mux and transmit-choose change from pulse to pulse and require a separate timing signal generator. An NI PXI-e timing/control module, driven by the data ingest software, generates the control. This software tags each recorded waveform with its corresponding transmit/receive antenna pair identifier. The data is written to memory in a serial fashion and parallelized in post-processing using the antenna pair identifier in the record header.

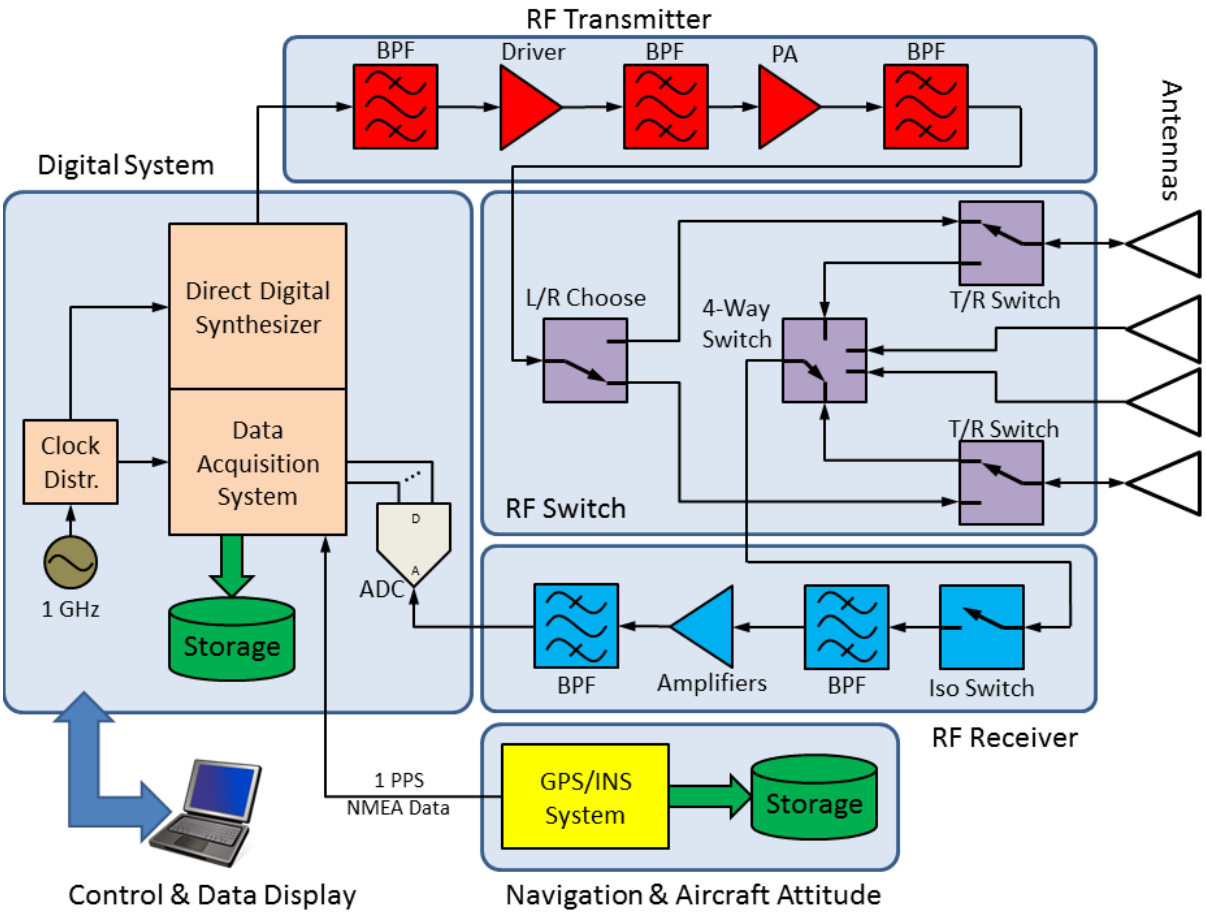

Figure 2. Airborne multi-channel system block diagram.

3.1.4 Airborne platforms and antennas

This UHF radar has been flown aboard short-range aircraft (de Havilland DHC-6 Twin Otter) and long-range aircraft (Lockheed P-3 Orion). The Twin Otter is a two-engine

propeller aircraft, with an average survey cruise speed of about 60 m/s and a survey range of about 1000 km. This translates to a maximum survey time of roughly 5 hours; most surveys conducted with this aircraft averaged 4.5 hours. The range and maneuverability of this aircraft suit it to short-range and tightly-gridded surveys [Rodriguez and others, 2013]. The available antenna space is a nadir-facing, 21”x19” elliptical opening in the aft portion of the aircraft. The antenna array is protected from the outside environment with a Kydex 100 radome, which is transparent at the frequency band of interest. A compact, 4-element array of Vivaldi antennas met the need for a simple, wide-bandwidth, electrically-small antenna and eliminating the need for a metallized back-plane. An all-metal vivaldi antenna [Weedon and others, 2000] was implemented for this application. Figure 3(a) shows the 4-element array in its custom mounting structure. A 4-to-1 power divider/combiner was used to create a single antenna. Figure 3(c) shows the measured array return loss. Figure 3(e) shows the measured H-field (cross-track) antenna pattern at the lower, middle, and upper ends of the operational frequency band. The antenna has an average cross-track half-power beamwidth of 46°.

The Lockheed P-3 Orion is a four-engine, propeller aircraft with an average survey cruise speed of 130 m/s and an average survey range of 3800 km. This translates to an average survey time of 8 hours. The long range and maneuverability make this aircraft well-suited for low-altitude, large grids [Rodriguez and others, 2013]. A 3’x4’ area was available for antennas in the forward bomb bay. A wide-bandwidth printed circuit board (PCB) elliptical dipole antenna was developed. A separate balun circuit board, hosting a miniature ceramic balun, fed the antenna. Metal posts connected the balanced side of the balun to each half

of the antenna. A BNC coaxial connector on the unbalanced side allowed for easy connection of the antenna cables during installation. An 8-element array fit in the available space in this aircraft, arranged in 2 rows of 4 elements with 2 rows oriented in the cross-track dimension and the dipole axis of each antenna oriented in the along-track dimension. The element spacing fell between 0.5λ and 0.75λ across the frequency band of interest, where λ is the wavelength at the operating frequency. The array was glassed to a fiberglass radome with a 0.5-inch thick layer of low-dielectric constant foam (Rohacell 71) between the elements and the radome; this additional spacing reduces the dielectric loading the radome exerts on the antennas. Figure 3(b) shows the array installed on the aircraft panel. A metal backplane was installed λ/4 (10 cm) above the array to improve directivity. Holes in the backplane allow for short cable runs, reducing electrical loading to the elements. Figure 3(d) shows the measured return loss of the array. Figure 3(f) shows the measured H-field (cross-track) antenna pattern at the lower, middle, and upper ends of the operational frequency band. The antenna exhibited an average cross-track half-power beamwidth of 20°. For single-channel operation, an 8-to-1 power divider/combiner created a single antenna. For multi-channel operation, pairs of along-track oriented elements were combined using 2-to-1 power divider/combiners, resulting in a 4-element cross-track array. The outboard 2 elements of the array are shared for both transmit and receive via a T/R switch, while the inboard 2 elements are used for receive only. A SPDT switch is used to choose between transmitting from the left or right outboard antenna. A 4-to-1 multiplexer is used to choose the receive antenna.

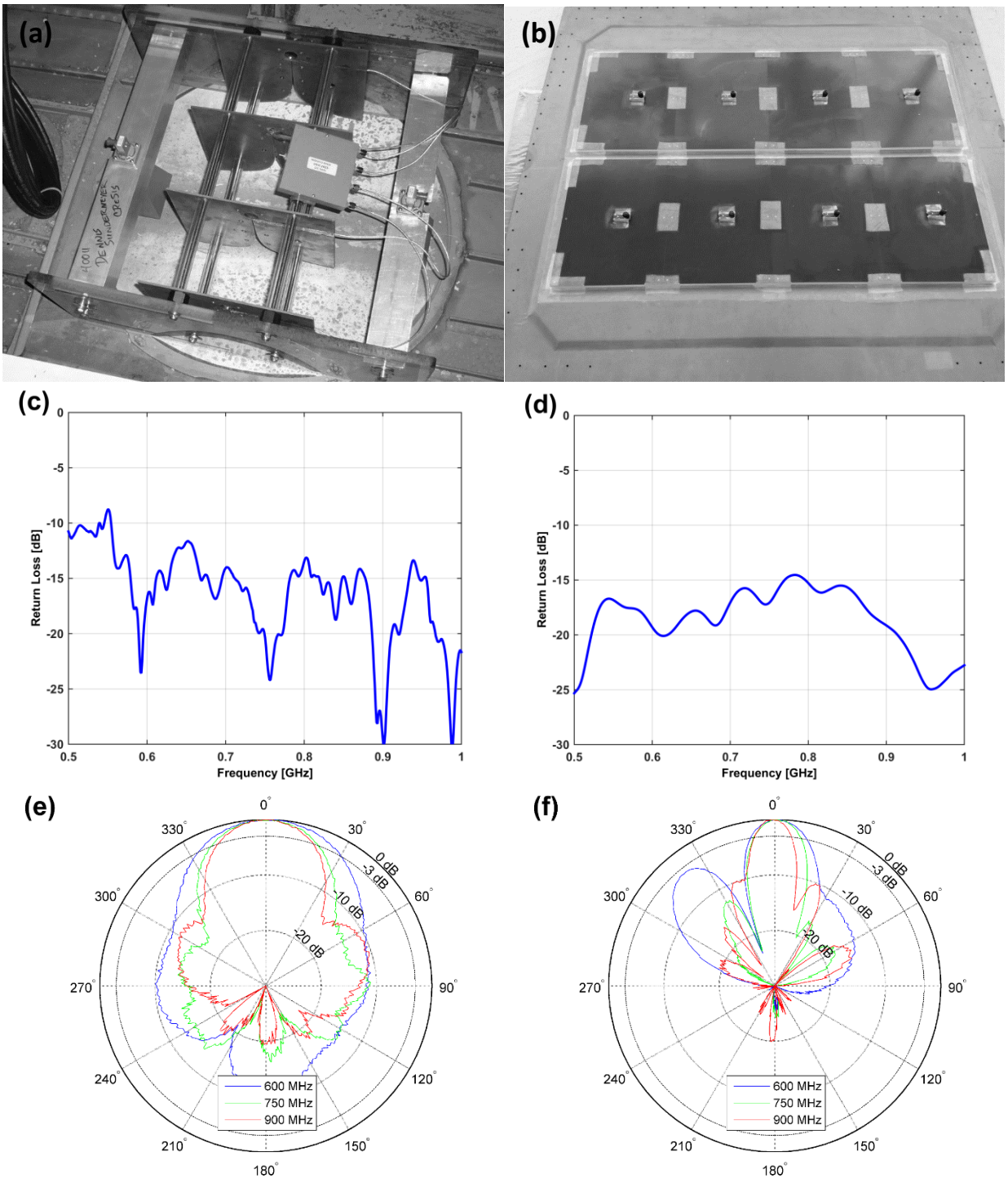

Figure 3. UHF radar mounted antennas, measured return losses, and measured normalized H-field (cross-track) directivity patterns. (a) 4-element Vivaldi array and custom mounting structure installed in Twin Otter nadir port. (b) 8-element elliptical dipole array installed on P-3 aircraft panel. (c) Twin Otter Vivaldi antenna array return loss. (d) P-3 elliptical dipole antenna array return loss. (e) Twin Otter Vivaldi antenna array normalized directivity pattern. (f) P-3 elliptical dipole antenna array normalized directivity pattern.

HFSS simulations were performed on the basic antenna structure for both the Vivaldi and elliptical dipole elements. These simulations were compared to laboratory measurements to evaluate the performance of the individual elements and the simulation. Figure 4(a) shows these comparisons for the Vivaldi element and Figure 4(b) for the elliptical dipole element.

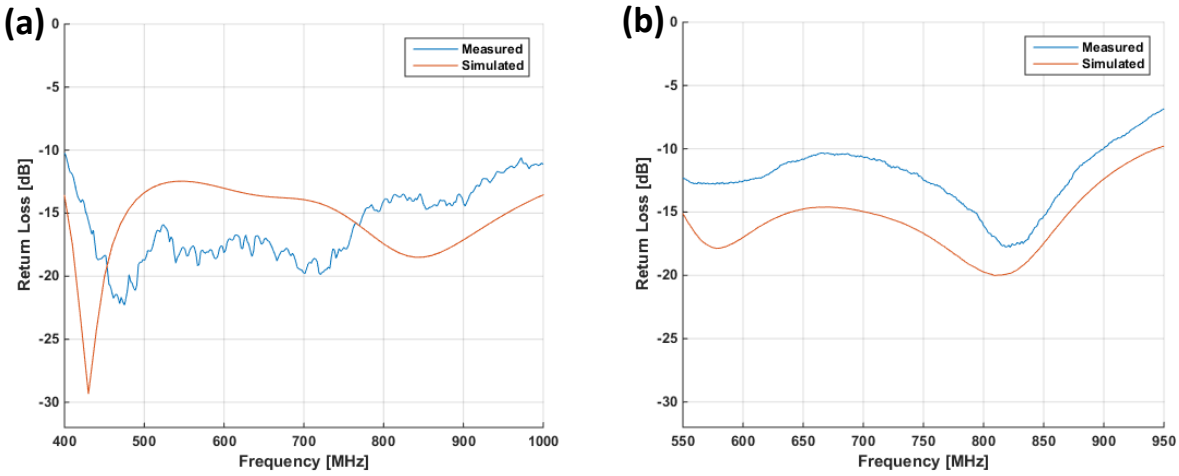

Figure 4. Single element simulation versus measured return loss. (a) Vivaldi element. (b) Elliptical dipole element.

Two resonances can be seen in simulated and measured return losses for both antennas. The simulated return loss for the Vivaldi element predicted a wider resonance spacing, off by ~50 MHz at the lower frequencies and ~130 MHz at the higher frequencies (compared to the measured return loss). This difference is likely attributed to manufacturing tolerances as the lower resonance is controlled by the width of the aperture at the mouth and the upper resonance is controlled by the width of the aperture near the feed. The width of the aperture near the feed is very narrow and difficult to manufacture with high precision. Nevertheless, the resulting manufactured element performed has acceptable return loss. The simulated and measured return losses for the elliptical dipole

exhibit good resonance alignment. After the element was simulated in HFSS, ADS was used to incorporate the measured balun board response to produce the final simulated result. The return loss amplitude difference is likely attributed to an unaccounted for coupling between the antenna element and the balun board.

3.1.5 Surface platform and antennas

A surface-based radar system was developed to support data collection using a larger antenna array than could be fit on the airborne platforms. This radar is similar to the multi-channel airborne radar, but uses a larger receive mux and separate transmit antennas in lieu of T/R switches. Figure 5 shows a block diagram of the ground-based multi-channel system.

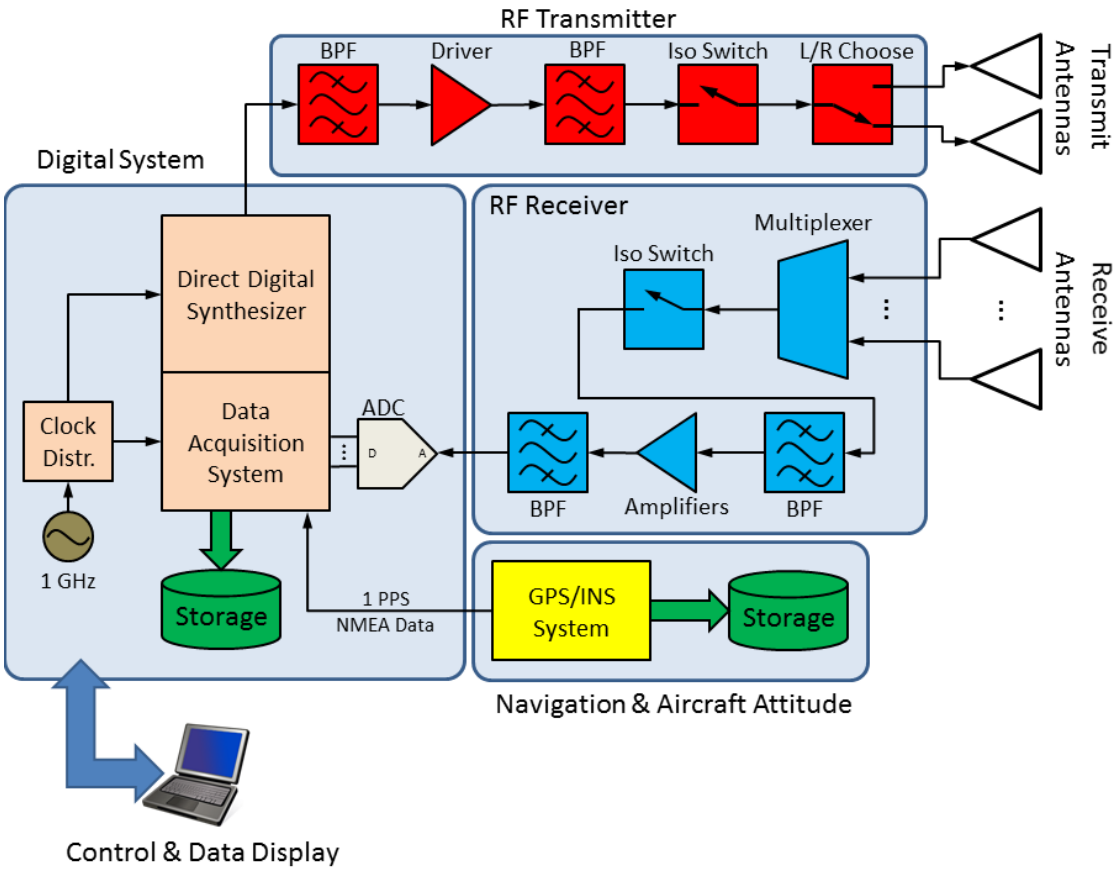

Figure 5. Surface-based multi-channel system block diagram.

The platform consists of a triangle shaped aluminum truss structure mounted to small snowboards. A lumber deck constructed on top of the sled holds the radar hardware and generator while providing a mounting platform for the cantilevered antenna array structure. The array structure was cantilevered off the back of the sled to reduce antenna loading by the metal sled structure. Figure 6 shows the assembled sled with the cantilevered antenna array structure and the radar chassis.

Figure 6. Assembled sled platform with antenna array and radar case.

The antenna element is a scaled and optimized version of a printed circuit wideband microwave dipole developed by Behera and Harish [2012]. A printed circuit balun was designed to attach perpendicular to the element. This balun board also serves to mount the element to the backplane, with its length used to set the optimal distance between the backplane and the element. A metal backplane was used to improve element directivity. Figure 7 provides a close-up view of the installed element, with the horizontal circuit board being the antenna element and the vertical circuit board being the balun/spacer. The feed and ground of the balun were soldered to the lobes the antenna where the circuit boards meet. Delrin braces (white) were used to reinforce the connection of the circuit boards and

stabilize the element to the ground plane. Simulations and testing found that the presence of small metal screws and nuts did not adversely affect the response of the antenna and were used for mounting in lieu of nylon screws/nuts or glue to improve rigidity.

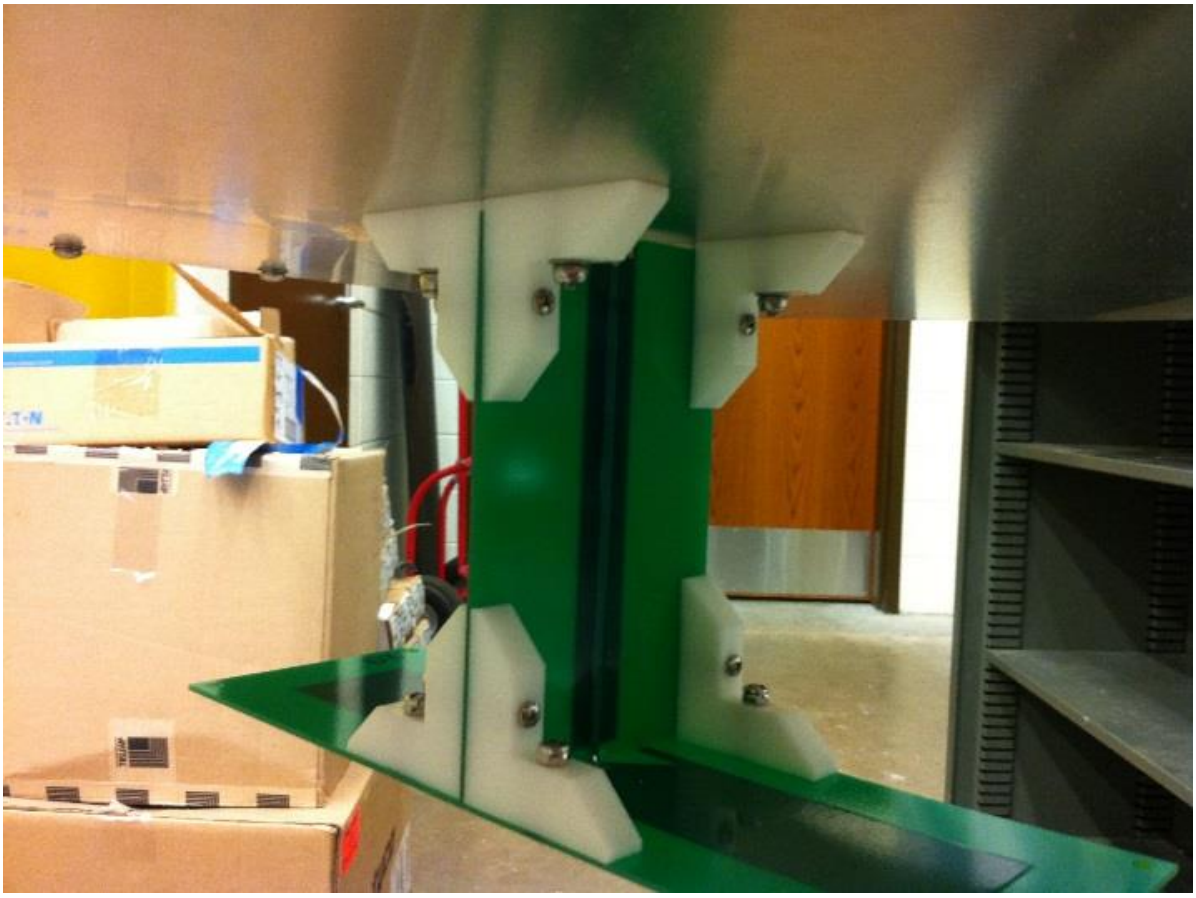

Figure 7. Close-up of mounted dipole element.

Figure 8 shows the measured and simulated return loss for a single element. The measured and simulated return loss have good agreement in the passband. Figure 9 shows the cross-track (H-field) antenna pattern for a single element. The antenna has a return loss better than 10 dB over the entire band of interest, and exhibits an average 3-dB beamwidth of ±40°.

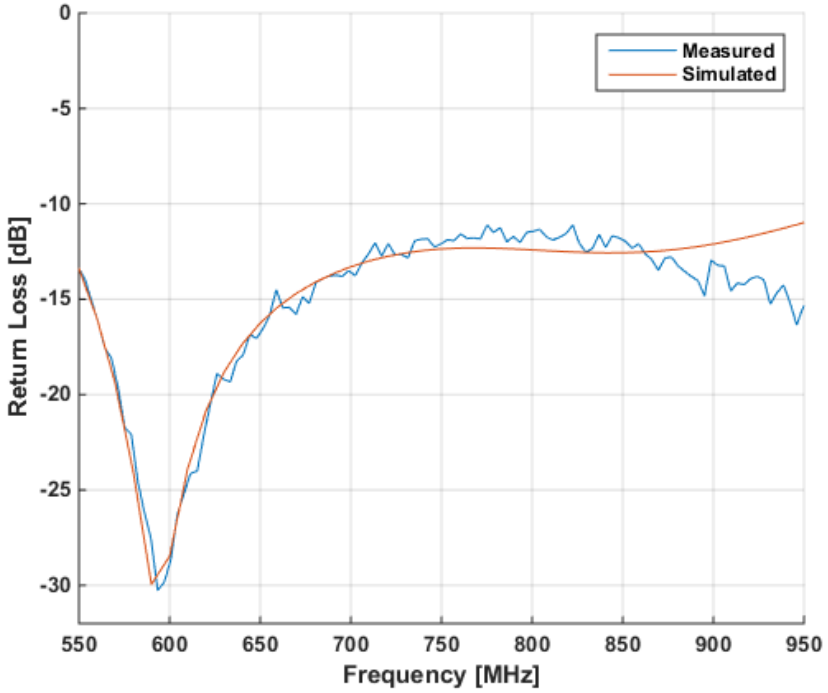

Figure 8. Measured and simulated return loss of PCB dipole element.

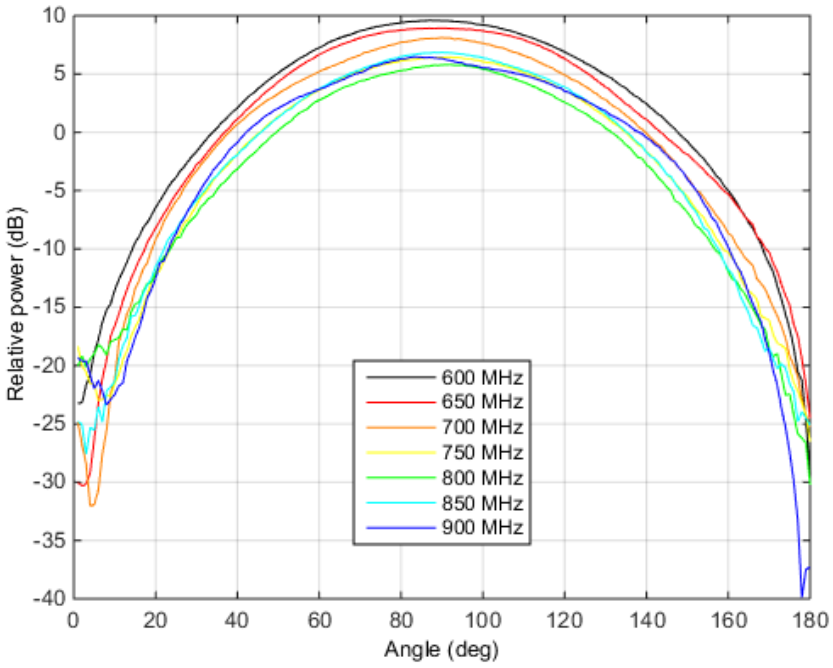

Figure 9. Measured cross-track antenna pattern of PCB dipole element with boresight at 90°.

The array is a linear configuration, with six or eight elements for receive and two transmit elements (one outboard on either end of the receive array). Spacing between the receive elements is 30 cm or 0.9λ at 900 MHz. The transmit elements were spaced 60 cm from the neighboring end receive elements to provide extra isolation. Figure 10 shows the array configuration, with the top row depicting the physical configuration and the bottom row depicting the resulting virtual array configuration spaced 0.45λ at 900 MHz.

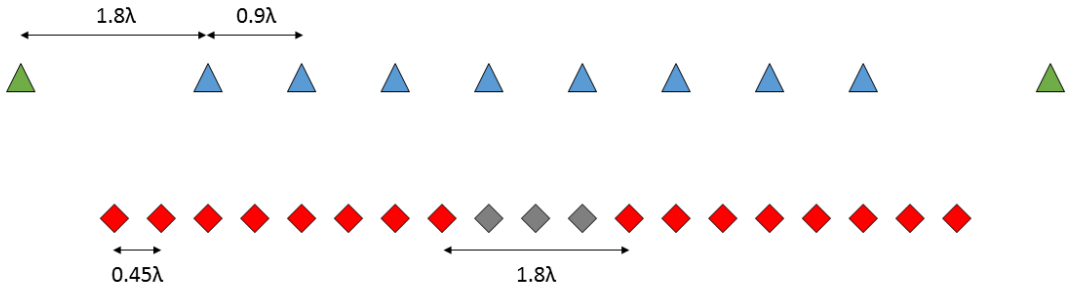

Figure 10. Array configuration. Top row: green triangles for transmit antennas and blue triangles for receive antennas. Bottom row: red diamonds depict the resulting virtual array and grey diamonds represent missing virtual elements. Horizontal spacings are defined at 900 MHz.

This configuration was chosen to simplify the mounting of the antenna array, but the placement of the transmit antennas outboard of the receive array resulted in a set of missing phase centers in the center of the virtual array. The proposed cross-track direction of the arrival algorithm can handle uneven element spacing.

3.2 System performance

To begin, the performance of the radar can be quantified by calculating the theoretical range resolution and accuracy. The range resolution ΔR defines the minimum distance for resolving two interfaces, and the range accuracy δ_r defines the maximum error of a measured

interface depth based on the signal-to-noise ratio (SNR) of the received return. These figures of merit are defined by

$$\Delta R = \frac{ck}{2B\sqrt{\varepsilon_r}}$$

and

$$\delta_r = \frac{\Delta R}{\sqrt{2SNR}}$$

where c is the speed of light, B is the bandwidth, ε_r is the dielectric constant of the medium and k is the window-widening factor. For typical operating parameters where k = 1.54, this radar has a theoretical range resolution of 77 cm in air (ε_r = 1), 53 cm in firn (ε_r = 2.1) [Ulaby and others, 1986b; Panzer and others, 2013] and 43 cm in ice (ε_r = 3.15) [Ulaby and others, 1986b]. For a smooth land ice surface, the expected SNR is 70 dB and the range accuracy δ_r is 0.16 mm. For a deep internal layer return at a depth of ~250 m, the expected SNR is 10 dB and δ_r is 8.9 cm.

The performance was further quantified in terms of the SNR using a link budget. Since the target ice interfaces are sufficiently flat within two or more Fresnel zones, we may consider them to be specular targets [Ulaby and others, 1986a]. In this case, the received power appears to originate from an image point at twice the range; therefore, the SNR for the interface is

$$SNR = \frac{P_T G^2 \lambda^2 (1 - |\Gamma_A|^2)^2 |\Gamma_L|^2 G_{RX} G_{PC} G_N}{\left(8\pi(R_A + R_I)\right)^2 L_I P_{N\_ADC}}$$

where P_T is the transmitted, G is the measured antenna gain, λ is the wavelength at the center frequency, Γ_A is the voltage reflection coefficient of the antenna, Γ_L is the voltage reflection

coefficient of a layer at depth, G_{PC} is the pulse compression gain, G_N is the coherent integration gain, G_{RX} is the receiver gain, R_A is the radar platform altitude, and R_I is the range between in the ice surface; in the target layer, L_I is the ice extinction, and P_{N_ADC} is the effective noise floor of the ADC.

Laboratory tests were conducted using an optical delay line together with an electro-optical transceiver to simulate a specular target at a distance of 500 m (the nominal operational altitude). RF attenuators are included in the loop to simulate attenuation of the transmit signal. Figure 11 shows a sample pulse-compressed waveform obtained from this test. The peak response agrees with the theoretical SNR of ~42 dB. The inset shows that the 3 dB width of the peak response is ~5 ns (or a range resolution of ~75 cm), matching well with theory.

The system performance was also verified in flight by recording data over smooth sea ice. The root-mean-square surface roughness of the sea ice have been measured to be <0.03 cm at C-band [Panzer and others, 2013], which means it is smooth at UHF frequencies. Figure 12 shows a sample compressed waveform from smooth sea ice off the east coast of Greenland. The dielectric constant of pure ice ($\varepsilon_r = 3.15$) [Ulaby and others, 1986b] was used as the surface density to calculate a surface voltage reflection coefficient of -5.5 dB and a surface return SNR of 77.2 dB. This agrees well with the 75 dB surface return SNR seen in Figure 12. A close-up of the surface response is shown in the figure inset. The 3 dB width of the surface response is ~5 ns (or a range resolution of ~75 cm), matching well with theory.

The system performance was further quantified using data collected over the dry snow zone. Within the dry snow zone, average surface snow densities are 0.3 g/cm^3 [Paterson, 1994] and therefore have an average dielectric constant of $\varepsilon_r = 1.53$ [Ulaby and others, 1986b] and a

voltage reflection coefficient of -9.3 dB. This results in a calculated surface return SNR of 69.5 dB; this agrees well with the surface return SNR of 70 dB over central Greenland, shown in Figure 13. Again, the 3 dB width of the surface response is ~5 ns (or a range resolution of ~75 cm), matching well with theory.

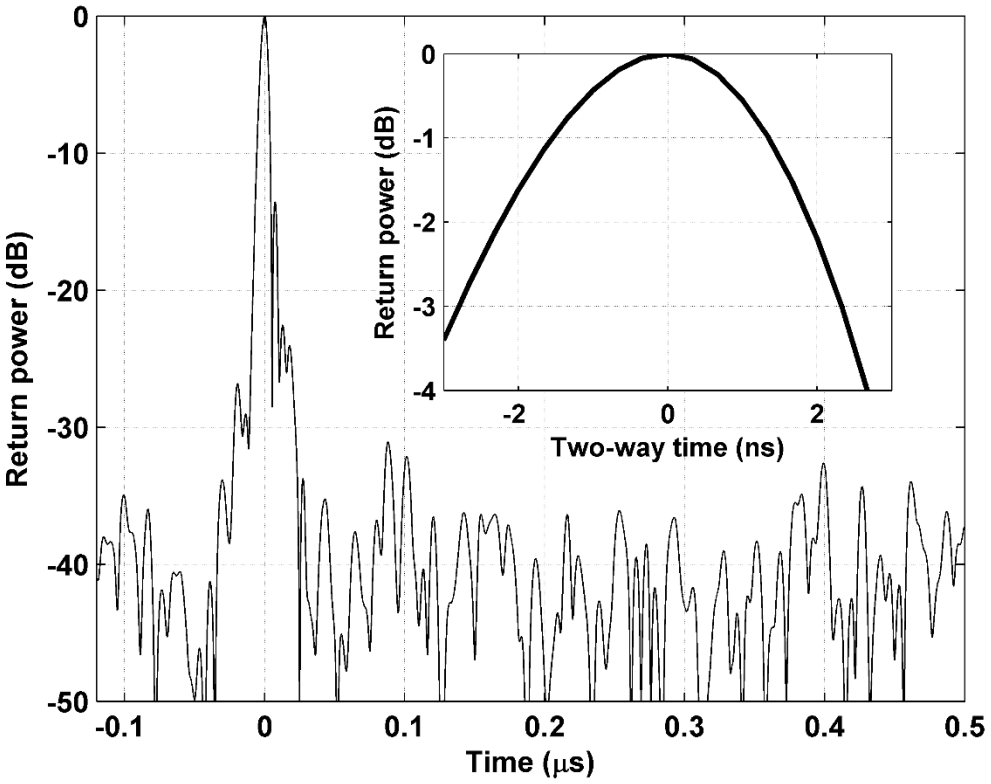

Figure 11. Time domain response obtained using an optical delay line as a simulated specular target. Inset shows a close-up of the response around the main peak.

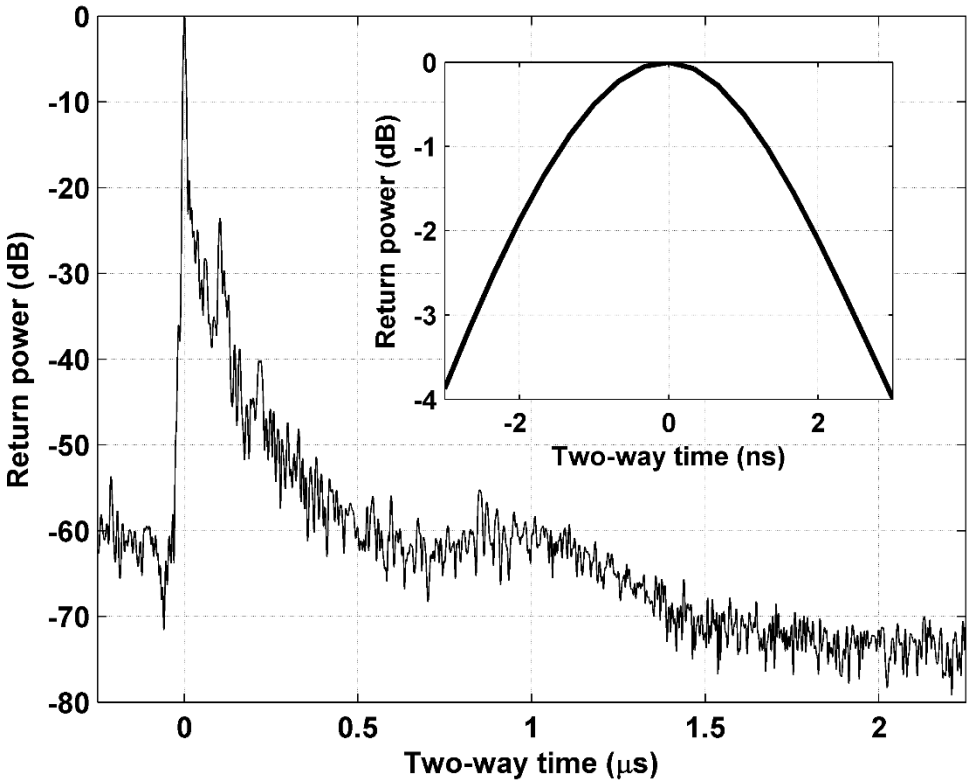

Figure 12. Time domain response from smooth sea ice. Inset shows a close-up of the response around the main peak.

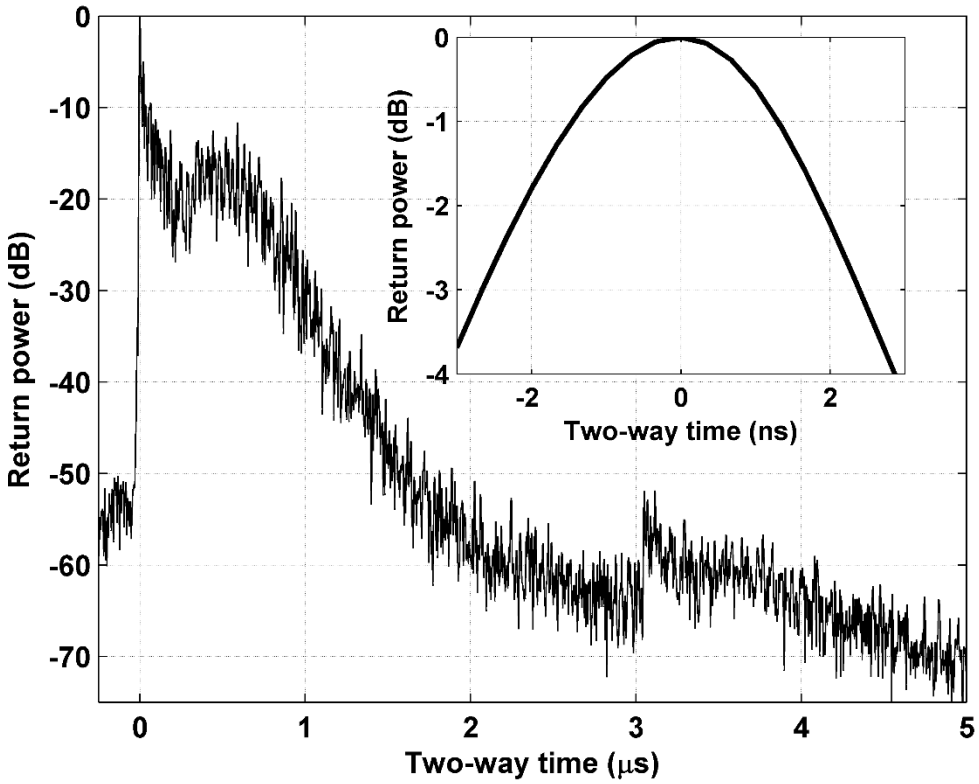

Figure 13. Time domain response from interior land ice. Inset shows a close-up of the response around the main peak.

3.3 System simulation

Qualification of system performance can be extended into the circuit simulation world. To gain an additional understanding of the factors that can influence the expected radar system response, a linear circuit simulation was conducted using Keysight's (formerly Agilent's) Advanced Design System (ADS) software. The goal of this exercise is to compare loopback data collected in the laboratory (Figure 11) with a similar configuration in simulation. Figure 14 shows the system simulation block diagram and Figure 15 shows the simulation setup in ADS. Full 2-port VNA measurements were collected for the transmit path (including the transmit half of the T/R switch), the receiver path (including the receive half of the T/R switch), and the

fiber-optic transceiver (delay line). Measurements of the delay line were performed with a sufficiently large number of points (longer time, smaller frequency delta) to properly characterize the full delay (~3.38 µs) seen through the optical line. The transform (time-domain) display was observed on the VNA to verify that the full delay had been characterized. The simulation setup was tailored to include all of the attenuation used in the loopback setup of 137 dB. The transmitter and receiver measurements both included 30 dB of attenuation. The nominal in-band (600-900 MHz) attenuation of the delay line is 32 dB. The coupler mainline has a loss of ~1 dB and the coupler coupled-line loss is 6 dB. The insertion loss of the isolator set is ~1 dB. Cascaded SMA attenuators are used for the remaining 37 dB of attenuation.

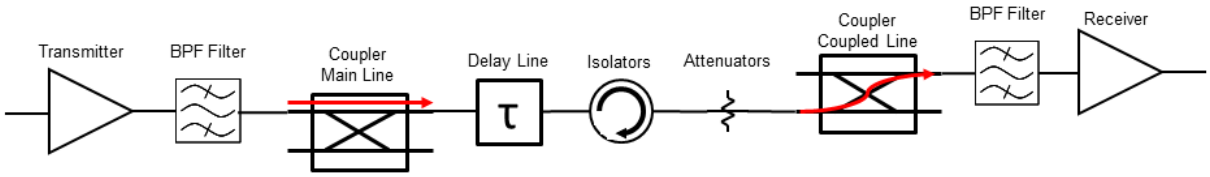

Figure 14. System simulation block diagram.

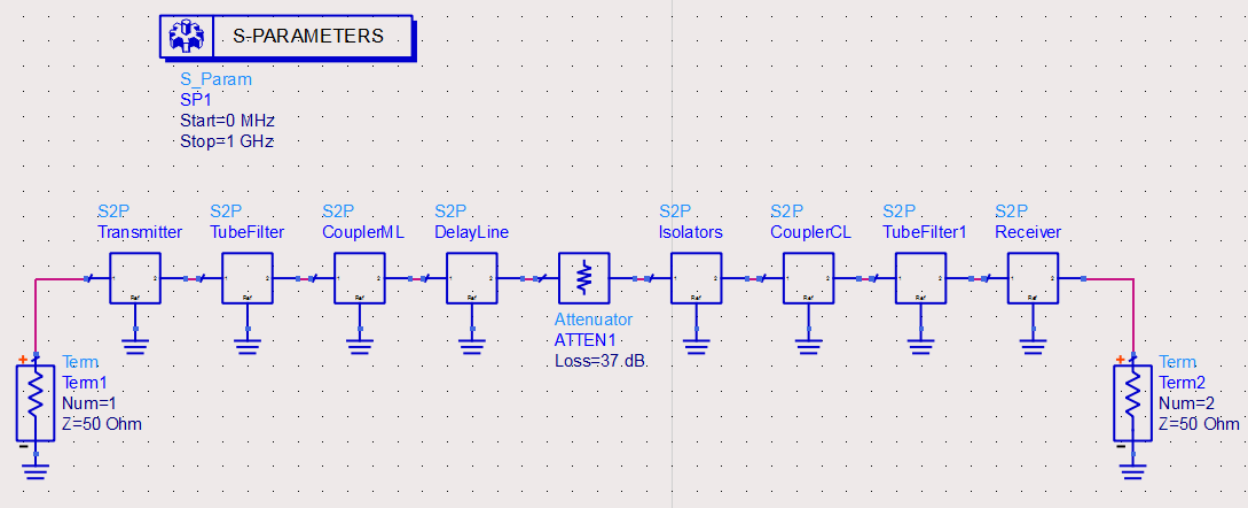

Figure 15. ADS radar simulation setup.

A linear scattering (S) parameter simulation was performed; this generated a full loop impulse response. A 600-900 MHz pulsed-chirp (with a pulse width of 2.048 µs, a power level of -26 dBm, and a 20% Tukey window) was generated in Matlab; this pulse is an ideal representation of the pulse generated by the DDS in the radar hardware. The simulated impulse response and ideal pulse were multiplied in the frequency domain and transformed back to the time domain. White noise equivalent to the receiver noise floor was added to the simulated signal. The resulting signal is analogous to the signal recorded by the radar ADC.

The delay line target was characterized alone. A single port S-parameter measurement (S_{11}) was performed, again using a sufficiently large number of points to fully characterize the delay line. Figure 16 shows the block diagram of this setup; the green arrow highlights the measurement interface and the red arrows show the signal path. This measurement was also driven with the ideal chirp signal using Matlab.

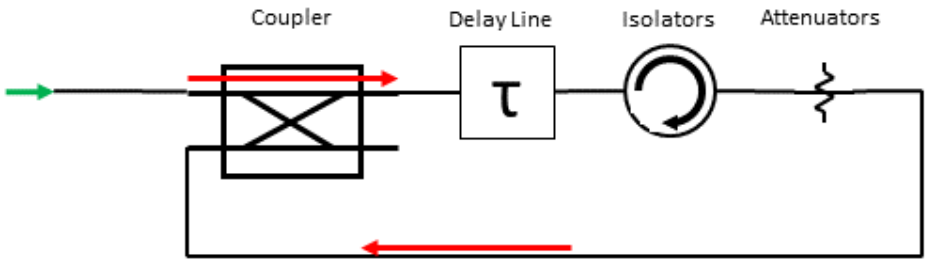

Figure 16. "Target" single port (S11) measurement setup.

The laboratory loopback data, simulated loopback, and measured target impulse response were windowed, pulse compressed and compared. Figure 17 shows this comparison. There is good agreement between the laboratory loopback and simulated responses. The SNR is ~40 dB. It was observed that the mainlobe and first trailing sidelobe are a result of the delay line target, while the remaining sidelobes are a result of the radar system (i.e. transmitter and

receiver) response. The mainlobe exhibits some very minor asymmetrical broadening; this is attributed to the amplitude taper of the driving chirp [Doerry, 2007]. With the first trailing sidelobe attributed to the target response, the highest sidelobe of the radar system is ~21 dBc. Sidelobe pairs (equal spacing from the mainlobe) have been highlighted. Sidelobe amplitude asymmetry is due to an uncompensated dispersion and phase non-linearity; the tubular bandpass filter used at the transmitter output (which is also the receiver input port) is likely a significant contributor. The insertion loss, return loss, and group delay of the bandpass filter are shown in Figure 18 and the passband edges have been highlighted. Amplitude differences below -21 dB are less than $1/125^{th}$ of the main peak power. However, improved sidelobe performance is necessary as sidelobes can mask closely spaced interface reflections. Compensating for phase non-linearities and amplitude modulation can improve sidelobe performance.

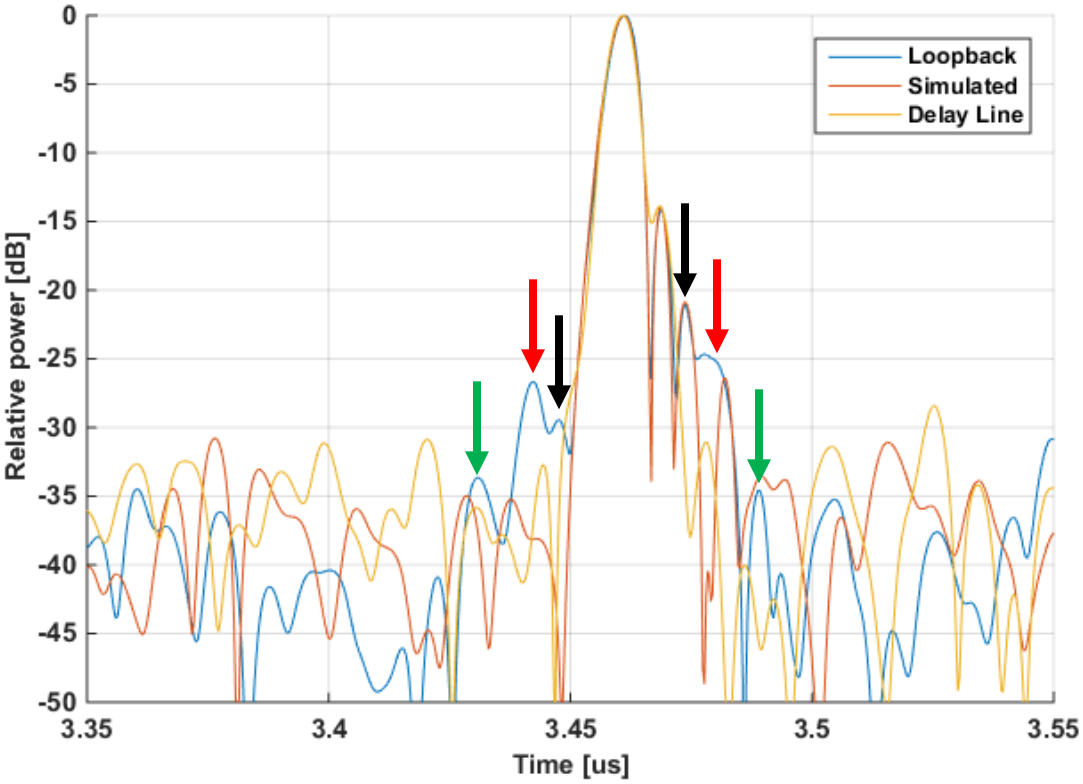

Figure 17. Time domain loopback response versus simulate response.

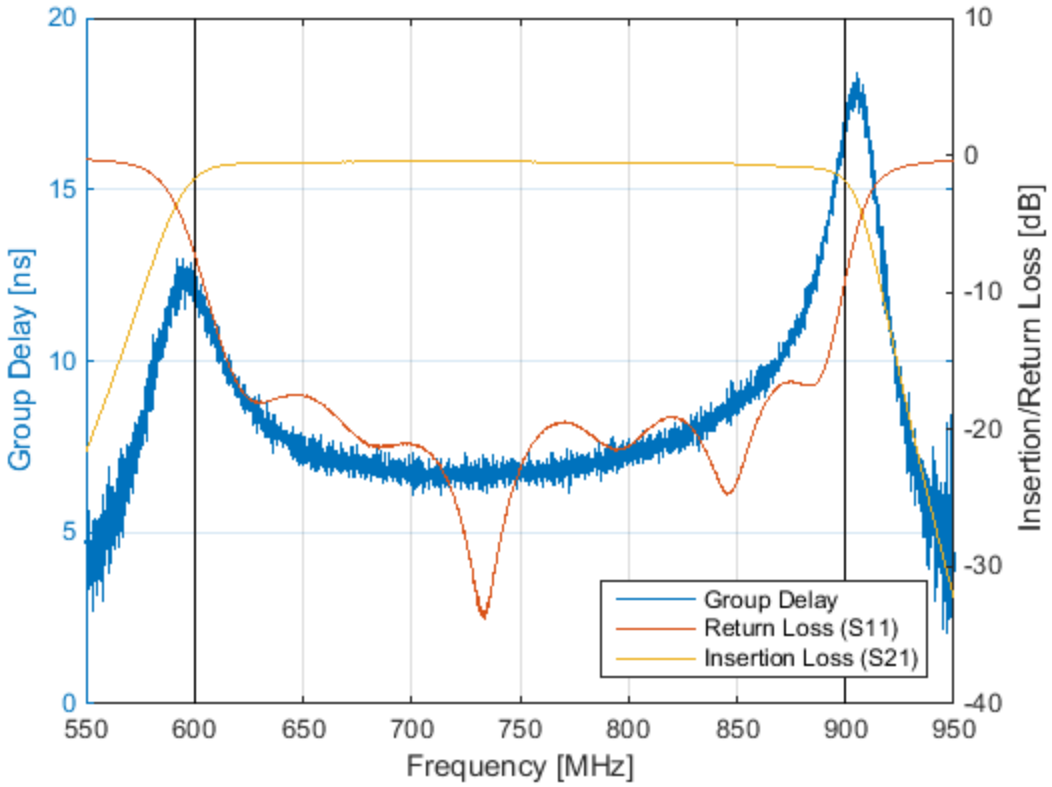

Figure 18. Insertion loss, return loss, and group delay of the tubular bandpass filter. Passband edges have been highlighted.

These simulations can be used to predict the system response, based on S-parameter measurements or simulations of individual components. Phase and amplitude distortions caused by system components can be compensated for by pre-distorting the initial chirp generated by the DDS using the predicted system response. Gomez-Garcia [2014] performed in-flight system measurements to generate a pre-distorted chirp. This resulted in significantly lower sidelobes. Figure 19 shows two example returns from open water using the pre-distorted transmit chirp. Sidelobes have been suppressed to approximately 40 dBc.

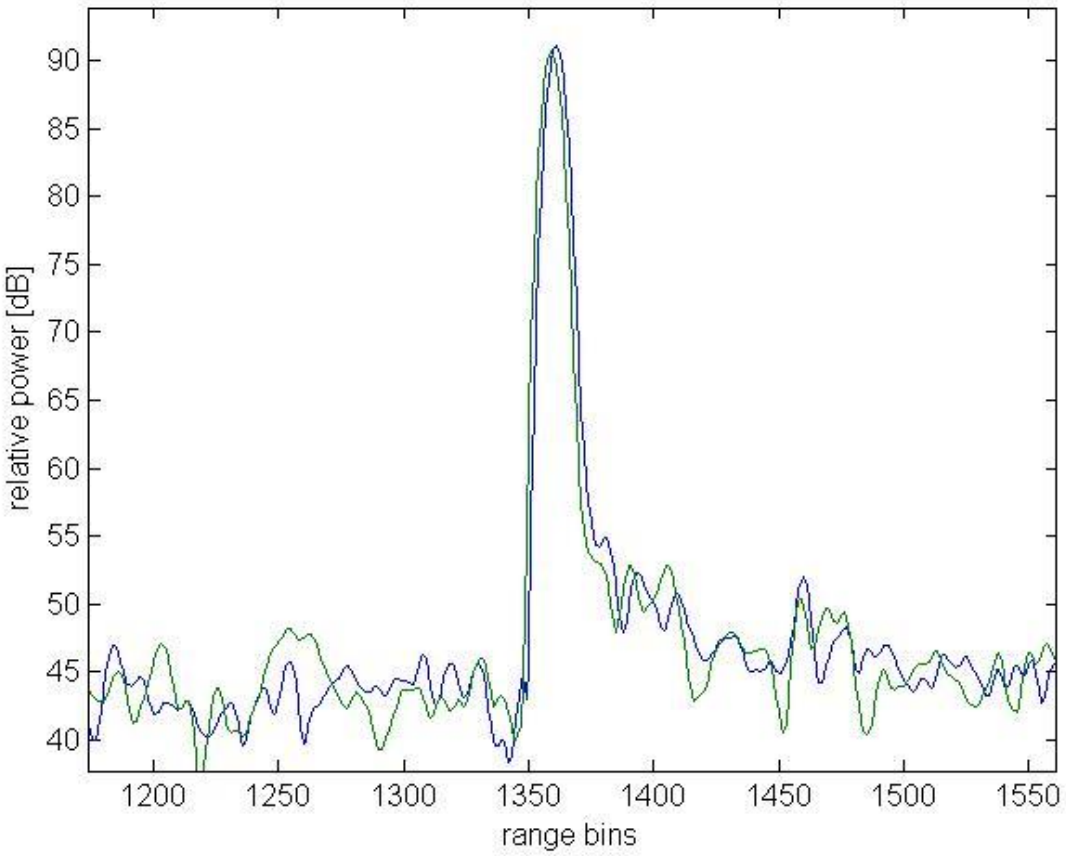

Figure 19. Open water returns showing lower sidelobes after applying chirp pre-distortion calculated from system response [Gomez-Garcia, 2014].

3.4 Field validation

Several field measurement programs were completed with the UHF radar. First, the radar was flown aboard a Twin Otter in Antarctica during the 2009/2010 austral summer season, supported by the U.S. Antarctic Program and based primarily at Byrd Camp in West Antarctica. Survey flights focused on the Thwaites and Pine Island glaciers in West Antarctica, including fine-scale grids on the Thwaites glacier near concurrent seismic measurements performed by Penn State University. Since 2010, the radar has been flown aboard the NASA P-3 as part of Operation Ice Bridge (OIB), collecting data over many regions of central Greenland and select major outlet glaciers. In spring 2011, the radar was flown aboard a Twin Otter concurrent with

the spring OIB campaign, but focused on fine-scale grids over Jakobshavn and Helheim glaciers, and Kangiata Nunaata Sermia. The radar was flown aboard a Twin Otter for the final time during the 2011/12 Antarctic season, focusing on the Byrd Glacier and its catchment. Sample multi-channel airborne data was collected over RIS as part of the 2013 NASA P-3 Antarctica campaign. Additional samples of multi-channel data were collected with the ground-based radar on RIS near the Mercer Ice Stream during the 2013/14 austral summer Antarctic season. Table 4 summarizes the field campaigns in which the radar was deployed. Figure 20 and Figure 21 show the flight lines where valid radar data were collected in Greenland and Antarctica, respectively, through spring 2013. The flight lines are segregated by year and platform. All airborne missions were flown at a nominal altitude of 500 m.

Table 4. Accumulation radar field campaign summary

Year	Season	Continent	Platform	No. of Missions
2009	Austral summer	Antarctica	Twin Otter	31
2010	Spring	Greenland	NASA P-3	23
2011	Spring	Greenland	NASA P-3	28
	Spring	Greenland	Twin Otter	9
	Austral summer	Antarctica	Twin Otter	16
2012	Spring	Greenland	NASA P-3	38
2013	Spring	Greenland	NASA P-3	27
	Austral summer	Antarctica	NASA P-3	6
	Austral summer	Antarctica	Ground sled	10
2014				

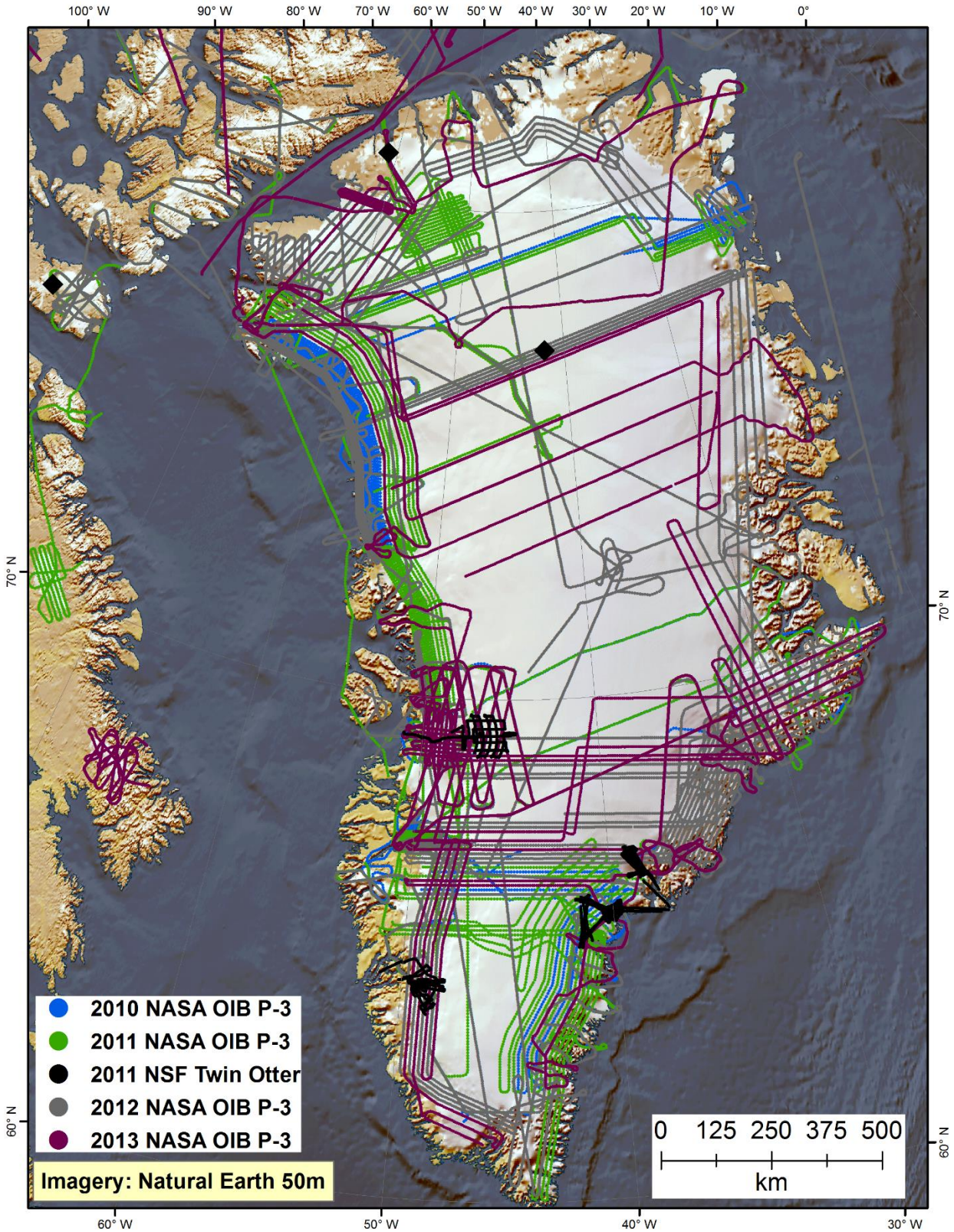

Figure 20. Flight lines where valid Accumulation Radar data were collected over Greenland and the Arctic during the 2010-2013 P-3 and 2011 Twin Otter field experiments.

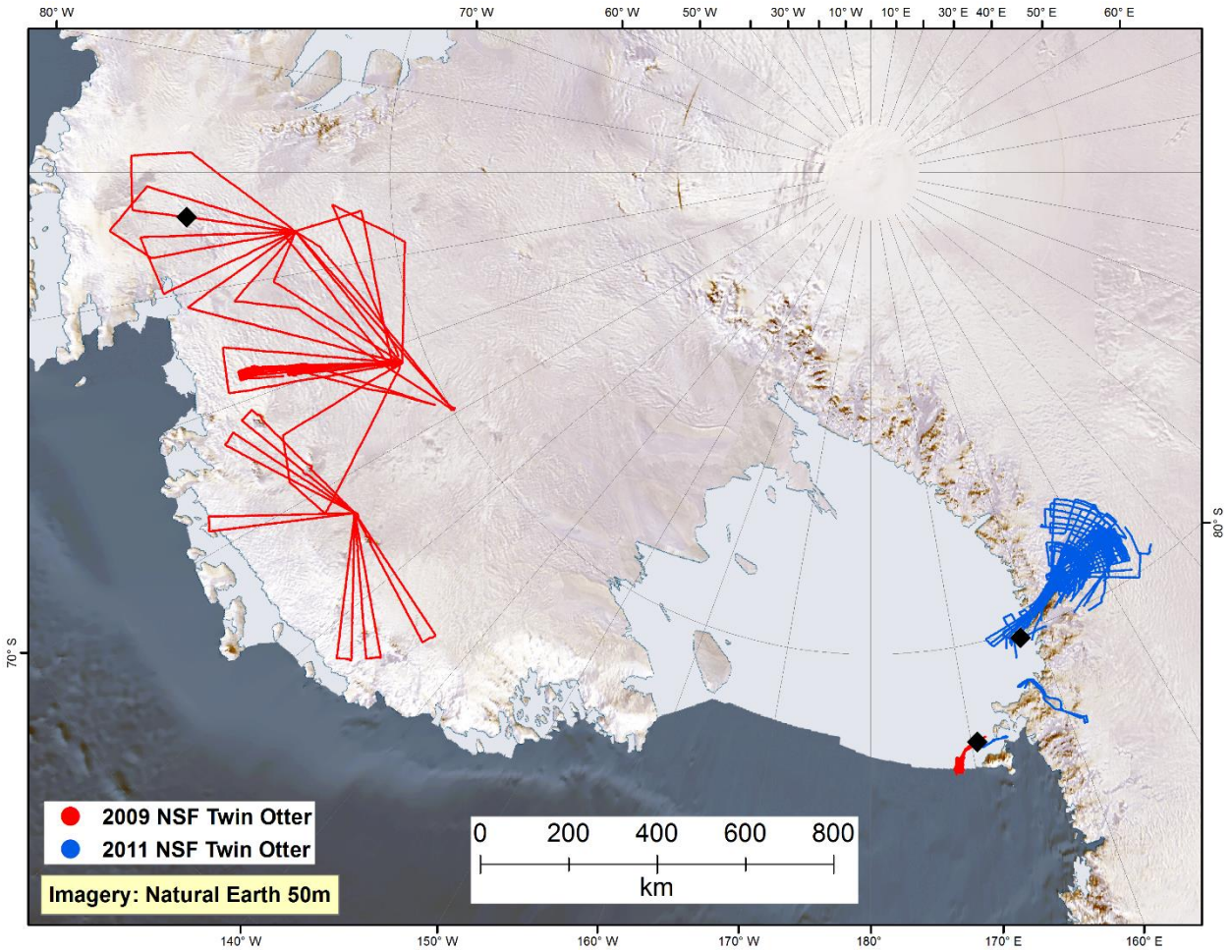

Figure 21. Flight lines where valid Accumulation Radar data were collected over Antarctica during the 2009/2010 and 2011/2012 Twin Otter field experiments. Inset shows location of ground-based multi-channel radar data collection.

3.5 Data examples and discussion

Data examples are presented to further quantify the performance of the radar and illustrate its capabilities. These examples are framed within the context of traditional glaciological issues: englacial reflections, firn compaction, and radiowave attenuation rates. Comparisons between surface tracking and OIB Airborne Topographic Mapper (ATM) surface elevation data are shown to verify accuracy. Shallow ice and ice-shelf sounding examples are included; significant basal return SNR suggests that parametric imaging algorithms should be applicable and accurate. The information presented in this section is largely taken from Lewis and others [2015].

3.5.1 Englacial reflections

Reflections from internal interfaces have been recorded with this radar system over regions of central Greenland and West Antarctica. Over cold regions of central Greenland where ice temperatures are -20°F or colder [Robin, 1972] and signal attenuation is relatively low, reflections were often recorded from interfaces below the maximum expected firn-ice transition depth of 200 m. Figure 22 shows a radargram from central Greenland showing the presence of interface reflections at propagation velocity-corrected depths in excess of 600 m. These data were collected during the spring 2012 NASA Operation IceBridge (OIB) experiment. The diamond marker at 77.2°N, 42.6°W in Figure 20 indicates the approximate location of this radargram. The radargram is detrended to enhance the observation of deeper layering. A sample, normalized received power trace is shown on the right side of the radargram. The trace was not detrended to preserve the actual relative amplitudes. The position of this trace is marked by the vertical line, and the ice surface and surface multiple are annotated. The surface multiple is an artifact cause by the retransmission of the received surface return reflecting off the bottom of the aircraft. The surface multiple follows the change in altitude of the aircraft. At the nominal survey altitude of 500 m, we expect to see this multiple at an average depth of 270 m.

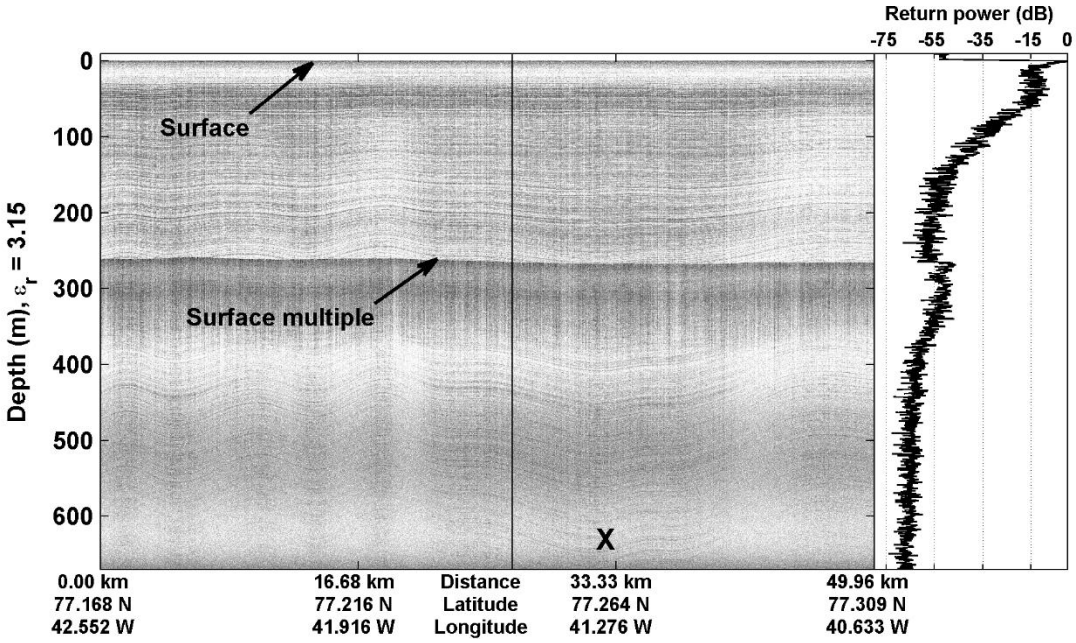

Figure 22. Radargram of Interior Greenland showing resolvable interface reflections.

Two mechanisms have been proposed as the cause of observed reflective interfaces in polar ice: variations in density and variation in loss tangent [Paren and Robin, 1975; Millar, 1982]. Density variations are the result of compression and recrystallization of snow particles. This mechanism dominates above the firn-ice transition depth, typically at a maximum of 200 m. Below this transition, the paradigm is that reflections result from changes in the loss tangent, which are believed to occur due to changes in conductivity [Millar, 1982; Hempel and others, 2000], where conductivity is product of the ion concentration (acidity) and mobility. Paren and Robin [1975] and Paren [1981] found that the reflection coefficient of a layer of acidic ice with a given thickness can be estimated from the deviation of the conductivity of the layer from the background conductivity of the surrounding ice. Using numerical modeling, Clough [1977] found that for a grouping of closely-spaced reflecting layers with varying thicknesses and conductivities, the total

reflection coefficient can be approximated as a single interface, with an averaged change in conductivity that is weakly dependent on the layer thickness. Therefore, the reflection coefficient of a given horizon can be approximated by

$$R = \frac{\Delta\sigma}{2\pi f \varepsilon_r \varepsilon_0}$$

where Δσ is the conductivity deviation and f is the radar frequency. Conductivity anomalies measured from ice cores in central Greenland have been found to be approximately 10-20 dB above the background conductivity of 10^{-6} S/m [Millar, 1982; Hammer, 1980]. Interface reflection coefficients range between -60 dB for larger anomalies at the lowest frequency of operation to -84 dB for small anomalies at the highest frequency of operation. Given the operational parameters of our radar system, the aircraft height, and the expected propagation loss: reflection coefficients as low as -80 dB can be detected near the maximum expected firn-ice transition, at a depth of 200 m. Reflection coefficients as low as -67 dB can also be detected at a depth of 650 m, with the deepest returns observed in the dataset. Conductivity anomalies are the dominant reflective mechanism observed by our radar below the firn-ice transition. Figure 23 shows an enlarged view of the deepest layers seen below 600 m. A custom bas-relief filter is applied to the image to enhance the layering visibility. The location of this view is marked with an X in Figure 22. At this point, the returns are just a few dB above the noise floor. The separation between adjacent bright interfaces was often found to be between 50 cm and 1.7 m.

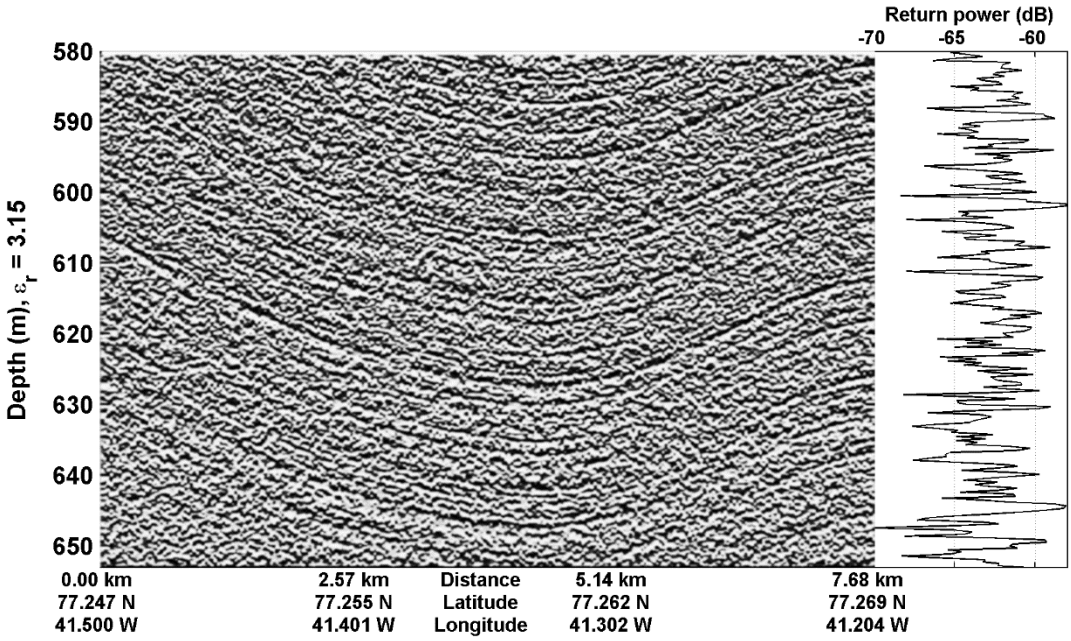

Figure 23. Enlarged portion of interior Greenland radargram around deepest reflections. A custom bas-relief filter was applied to enhance layering visibility.

Most of the data showing firn and ice stratigraphy were collected from ideally stratified areas. During the 2009/2010 Antarctic field season, data were collected over portions of the Pine Island Glacier (PIG) catchment in West Antarctica that exhibited significant undulating features. Figure 24 shows an example radargram from this region. The diamond marker at 76°S, 93.9°W in Figure 21 indicates the approximate location of this radargram. The surface was not artificially flattened to preserve the appearance of the surface topography. The maximum depth and SNR of received reflections are dependent on surface slope. Interface visibility is reduced with increasing surface slope and is likely a result of reflected energy being scattered off-vertical. Figure 25 shows an enlarged view of the region of layer pinching marked with an X in Figure 24. A custom bas-relief filter was applied to the image to enhance the layering visibility and highlighted a pair of pinched layers. Layering was resolved to a minimum spacing of approximately 55 cm.

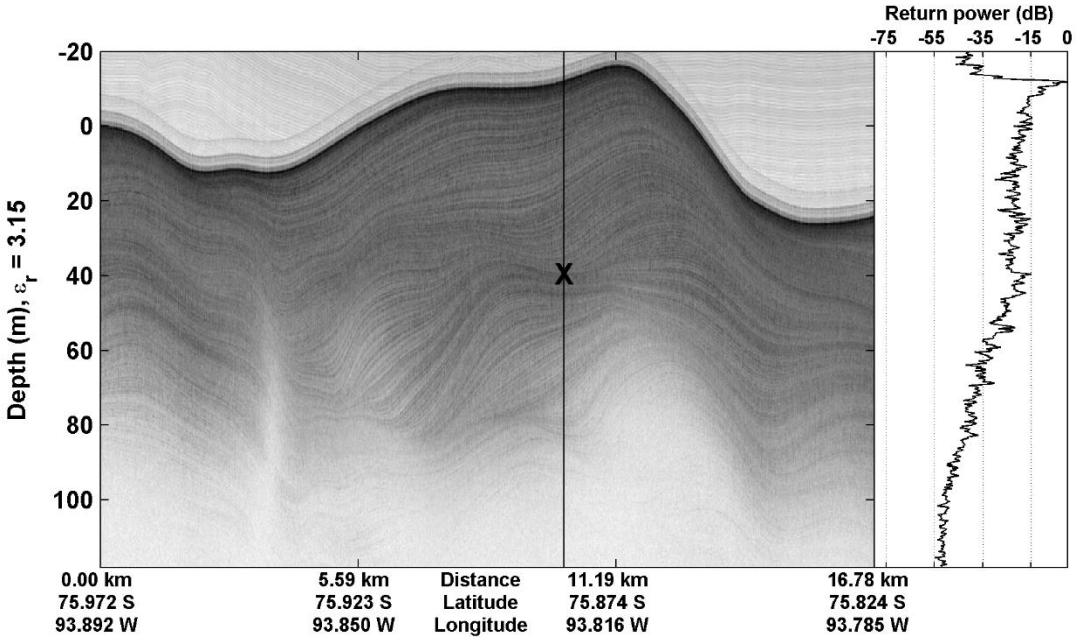

Figure 24. Radargram of Pine Island Glacier catchment showing significant undulations.

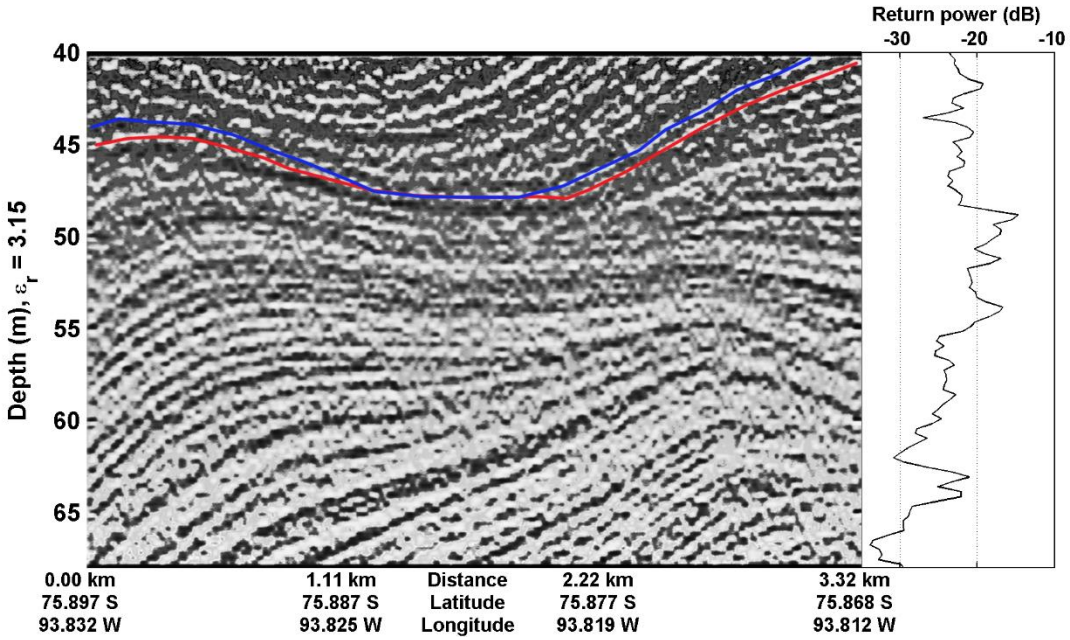

Figure 25. Enlarged portion of PIG radargram showing layer pinching. A custom bas-relief filter was applied to enhance layering visibility. An example of layer pinching is highlighted.

3.5.2 Firn compaction

In theory, the radar data can be used to derive an expected relative voltage reflection coefficient profile with depth and compared to a reflection coefficient profile derived from

the permittivity profile of an ice core. In practice, this direct comparison is difficult to achieve. In a few areas, the resolution of available core data can be two orders of magnitude finer than the radar resolution. A particular layer echo in the radar data may be a combined response of multiple variations that fall within the radar resolution [Harrison, 1973; Gudmandsen, 1975]. Harrison [1973] introduced a statistical approach for estimating the magnitude of the layer reflection coefficient. For a qualitative analysis, the variance of the fine-resolution ice-core permittivity profile was compared with the radar-derived reflection coefficients and found a positive correlation. As all of the interfacial two-way transmission coefficients are near unity, this result was expected. This means that each reflective horizon is receiving nearly the same incident energy; therefore, the shape of the reflectivity profile is tied to a variation in a physical parameter of the medium and is not simply a result of progressive incident energy loss. The dispersion of the permittivity profile is proportional to the potential reflection coefficient derived from it. A relatively large standard deviation implies a higher probability that neighboring permittivity measurements will have a large difference and therefore a large reflection coefficient while a relatively small standard deviation implies a higher probability that neighboring permittivity measurements will have a small difference and therefore a small reflection coefficient.

In Figure 26, the standard deviation of the Greenland B26 ice core [Miller and Schwager, 2000] is plotted with the radar data-derived reflection coefficients and scaled them accordingly to highlight their qualitative relationship. The closest available radar return was chosen, situated approximately 2.1 km from the core site. The standard deviation was calculated using a moving window with a width approximating the resolution of the radar.

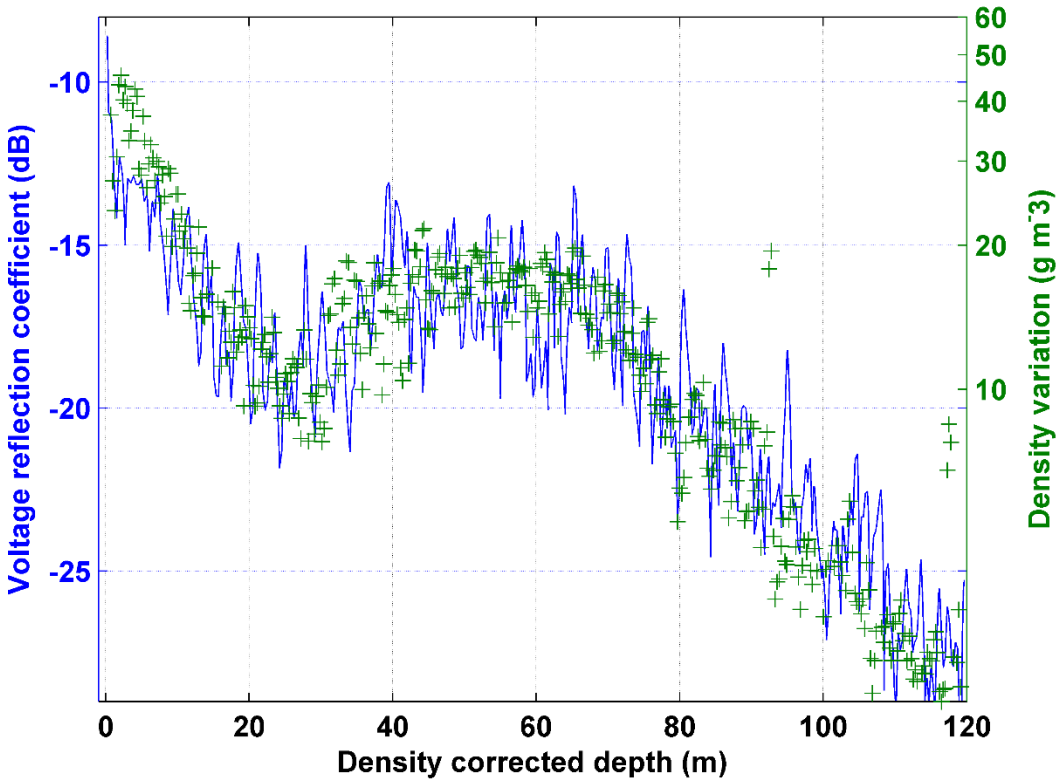

Figure 26. Radar-data-derived reflection coefficient compared with the measured B26 ice-core density variation.

Three distinct zones were observed within the top 100 m of the ice resulting from different firn densification mechanisms. The first zone occurs between the surface and the inflection point in the density standard deviation at a depth of roughly 25 m. Densities at the inflection point are approximately 550 kg/m^3 [Herron and Langway, 1980; Breton, 2011]. Random grain settling is the dominant densification mechanism [Herron and Langway, 1980; Hörhold and others, 2011; Breton, 2011]. High-density variability, resulting from seasonal changes in the crystal structure of accumulating snow, are observed near the surface [Hörhold and others, 2011]. Layers of different densities compact at different rates, with low-density layers compacting faster than high-density layers. This leads to a sharp decrease in the density variability to the minimum, where the layers have nearly the same

density [Hörhold and others, 2011]. The second zone occurs between the density variability inflection point and the point of pore close-off. Densities at pore close-off, at a depth of approximately 80 m, are approximately 830 kg/m^3 [Herron and Langway, 1980]. A cross-over in compaction rates is observed with low-density layers compacting slower than high-density layers. This leads to a zone of higher density variability [Hörhold and others, 2011] and a subsequent rise in the layer reflection coefficients in this zone. Inter-particle bond growth and particle deformation are the dominating densification mechanisms in the upper portion of the second zone, generally in the density range 550 to 730 kg/m^3 [Breton, 2011]. Particle deformation alone dominates densification in the lower portion of the second zone, generally in the density range 730 to 830 kg/m^3 [Breton, 2011]. The third zone occurs below pore close-off, where air-pore compression is the dominant densification mechanism [Herron and Langway, 1980]. Density variability quickly decreases with depth, as firn densities asymptotically approach pure ice. At this point, changes in the loss tangent begin to take over as the dominant mechanism for reflective interfaces.

3.5.3 Radiowave attenuation rates

For radar reflections from below the surface, signal extinction through the medium must be considered. Absorption has been found to be the dominating extinction factor, and values of roughly 19 dB/km are expected for our frequencies of operation at ice temperatures of -20°C [Goodman, 1975; Paden and others, 2005; Jacobel and others, 2009]. This is reasonable assumption for cold ice in the interior regions of the ice sheet. Attenuation rates through ice were further investigated by analyzing data collected over ice shelves, ice caps, and shallow glaciers. The depth-averaged attenuation was calculated by

taking the ratio of the received power between the surface reflection and the basal reflection where the attenuation L is the unknown component of the basal reflection received power. Solving for this loss results in:

$$L = \frac{P_S |\Gamma_B|^2 {R_S}^2}{P_B |\Gamma_S|^2 {R_B}^2}$$

where P_S and P_B are the received powers from the surface and basal reflections, respectively; Γ_S and Γ_B are the reflection coefficients of the surface and basal interfaces, respectively; and R_S and R_B are the ranges from the platform to the surface and basal interfaces, respectively.

The attenuation rate was calculated for the Petermann Glacier ice-shelf in northwestern Greenland. Figure 27 shows a radargram of the Petermann Glacier ice-shelf. A representative trace from near the terminus shows the relative amplitudes of the surface and basal reflections. The diamond marker at 80.9°N, 61.2°W in Figure 20 indicates the approximate location of this radargram. These data were collected aboard the NASA P-3 during the Spring 2013 OIB season. Photographic imagery from the OIB Digital Mapping System (DMS) [Dominguez, 2014] collected in concert with our radar data showed a snow-covered surface. Data collected by the CReSIS Snow Radar [Panzer and others, 2013], collected in concert with this radar, were investigated revealing that the snow cover thickness was typically less than the resolution of our radar and therefore unresolvable from the much denser ice below it. The density of this surface "interface" should fall between that of the snow (0.3 kg/m^3) and solid ice (0.92 kg/m^3), trending toward the higher value. For these calculations, an average surface interface density of 0.7 kg/m^3 was

assumed, which agreed with a link budget analysis. This corresponds to a dielectric constant of 2.5. An ice-water reflection coefficient was used for the basal return. The depth-averaged attenuation rate varied between 4.3 and 5.6 dB/km, with higher attenuation rates near the terminus and lower attenuation rates upstream.

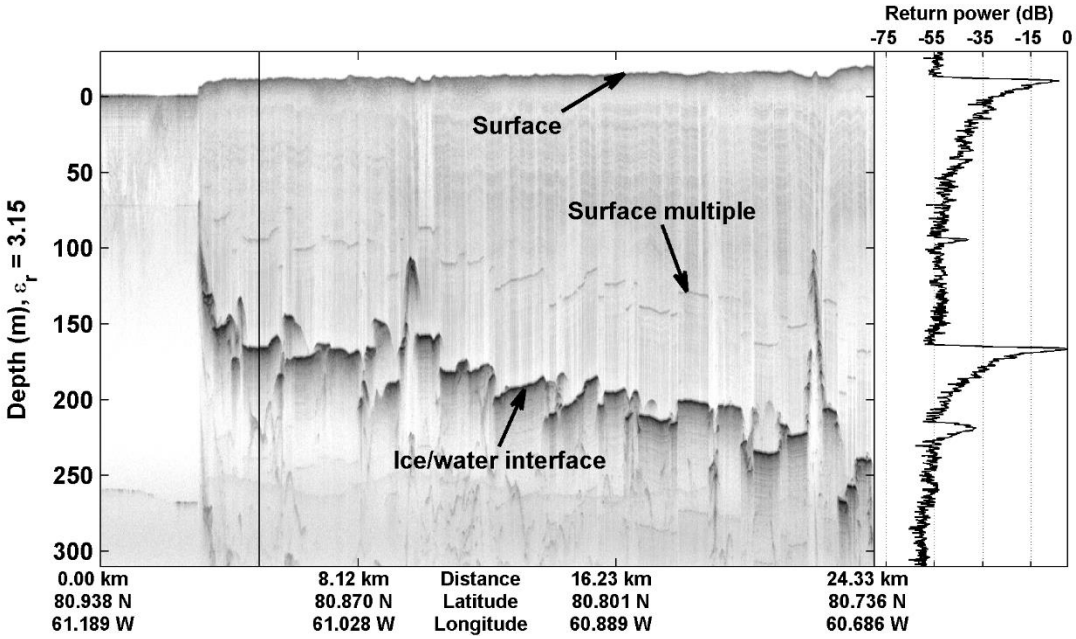

Figure 27. Radargram of the Petermann Glacier ice-self transect. A representative trace from near the terminus is provided.

The attenuation rate was calculated for two locations on RIS. The first location is a floating portion of the ice-shelf approximately halfway between the Pegasus runway and the Antarctic Geological Drilling (ANDRILL) site. Figure 28 shows a radargram of RIS at this location. A representative trace shows the relative amplitudes of the surface and basal reflections. Figure 29 provides an enlarged view of the top 50 m to highlight the firn layering. The diamond marker at 77.6°S, 171.6°E in Figure 21 indicates the approximate location of this radargram. These data were collected aboard the Twin Otter during the 2009/2010 Antarctic season. An average surface density of 0.7 kg/m^3 [Blaisdell and others,

1992; Arcone, 1996] and an ice-water basal interface were assumed. The average attenuation rate was found to be 16.4 dB/km. This value compares well with other reported RIS attenuation rates [Bentley and others, 1998; Peters and others, 2005; MacGregor and others, 2007].

The second location is a grounded portion of RIS near the base of the Mulock Glacier. Figure 30 shows a radargram of RIS at this location. A representative trace shows the relative amplitudes of the surface and basal reflections. The diamond marker at 79.5°S, 163.2°E in Figure 21 indicates the approximate location of this radargram. These data were collected aboard the Twin Otter during the 2011/2012 Antarctic season. An average surface density of 0.7 kg/m^3 was assumed. Granite rock and granite till are the reported bedrock conditions across many regions of Antarctica [Gow and others, 1968]. An average bedrock dielectric constant of 6 [Davis and Annan, 1989; Daniels, 1996; Zirizzotti and others, 2010] was assumed for the reflection coefficient calculations. Traces were investigated where there appeared to be a flat and level bedrock interface, indicated by a strong specular return. The average attenuation rate calculated was 16.3 dB/km.

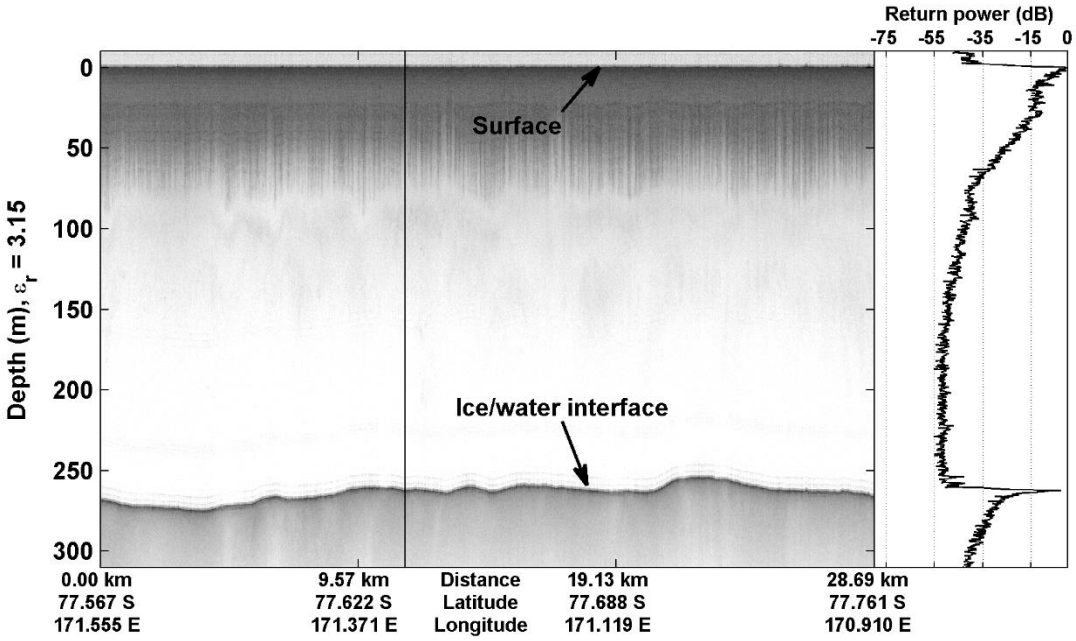

Figure 28. Radargram of a RIS transect located approximately halfway between the Pegasus runway and the ANDRILL site. A representative trace is provided.

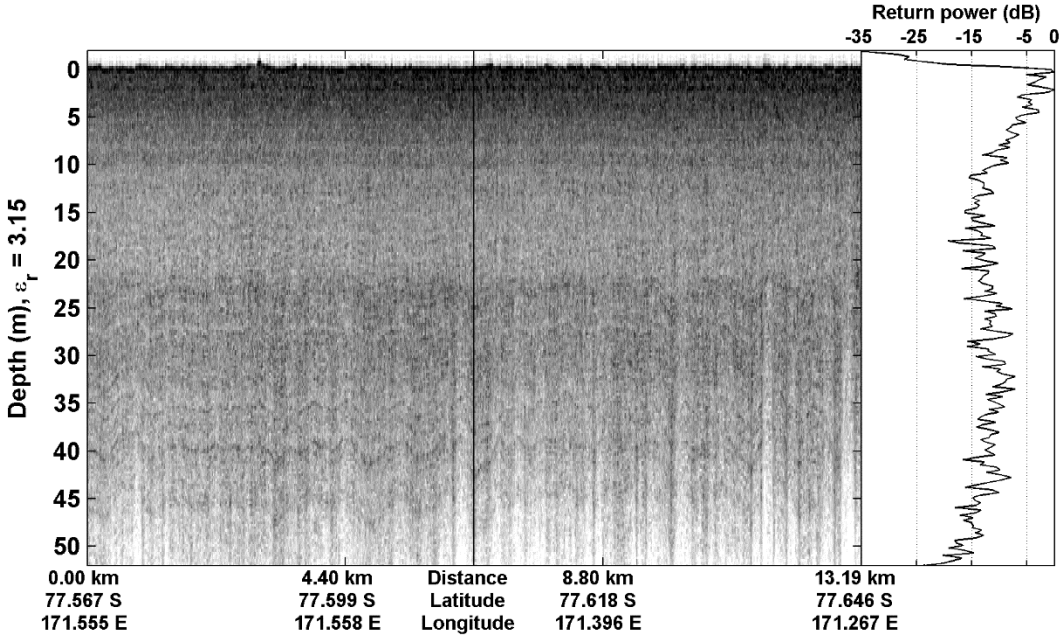

Figure 29. Enlarged portion of Ross Ice Self radargram to highlight firn layering.

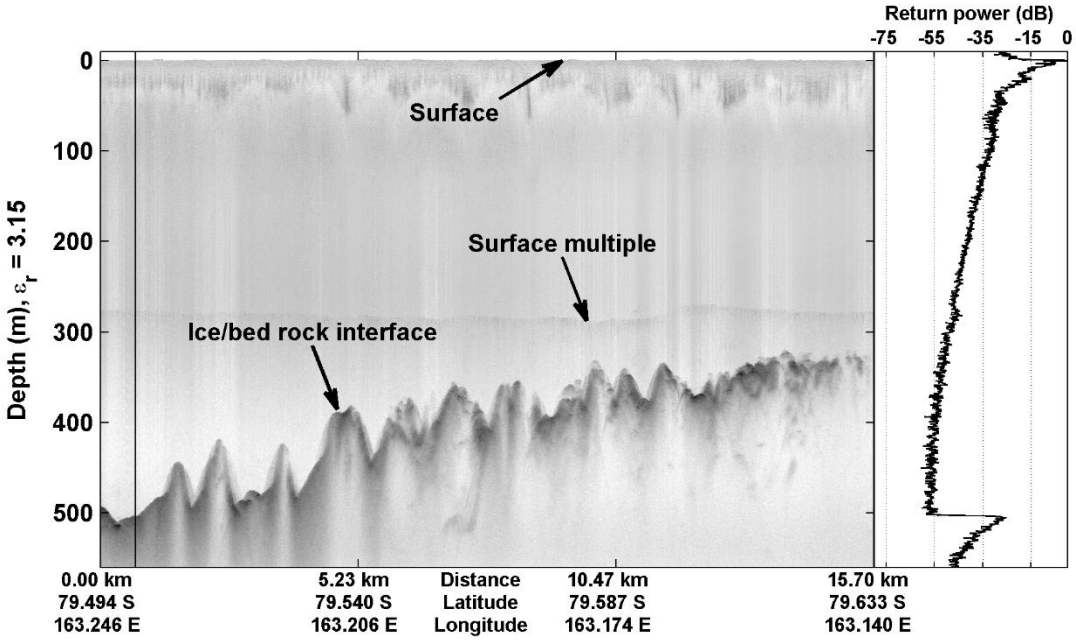

Figure 30. Radargram of a grounded portion of RIS located near the base of the Mulock Glacier. A representative trace is provided.

Attenuation rates through ice caps were also investigated. Figure 31 shows a radargram of data collected along the western edge of the Devon Island, Canada ice cap. The diamond marker at 75.1°N, 84.4°W in Figure 20 indicates the approximate location of this radargram. The radargram is corrected for platform elevation, but was not artificially flattened to preserve the appearance of the topography. False echoes seen below the bedrock are attributed to pulse resonance caused by strong returns. Overlapping features, as seen on the far right side of the radargram, are likely a result of a combination of off-nadir targets captured by the wide antenna beamwidth and pulse resonance of those returns from exposed bedrock. Significant near-surface banding may be attributed to varying degrees of summer melting, as reported by Clark and others [2007]. Traces were investigated where there appeared to be a flat and level bedrock interface, indicated by a strong specular return. An average surface density of 0.5 kg/m^3 [Clark and others, 2007] and a bedrock

dielectric constant of 6 were assumed. The average attenuation rate calculated was 6.6 dB/km.

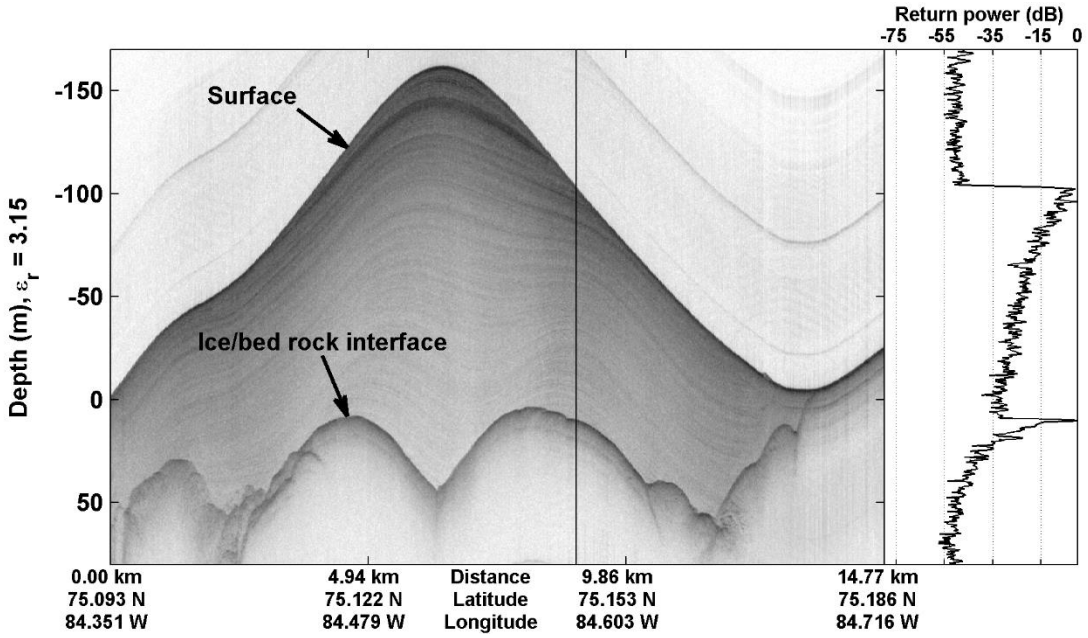

Figure 31. Radargram from along the western edge of Devon Ice Cap. A representative trace is provided.

3.5.4 ATM surface return comparison

The surface tracking accuracy of this radar was verified by comparing it ATM L2 elevation data [Krabill, 2015]. Surface elevations for two glacial ice shelves in northern Greenland were investigated. Figure 32(a) shows the elevation comparison for the Petermann glacier and Figure 32(b) shows the elevation comparison for the Academy glacier. Inset histograms show the distribution of elevation error. The mean error between the radar data surface and the ATM data surface is approximately 1 m. There is a good correlation of the broad elevation changes measured by both systems; error between the two can be attributed to differences in vertical resolution and beam footprint size.

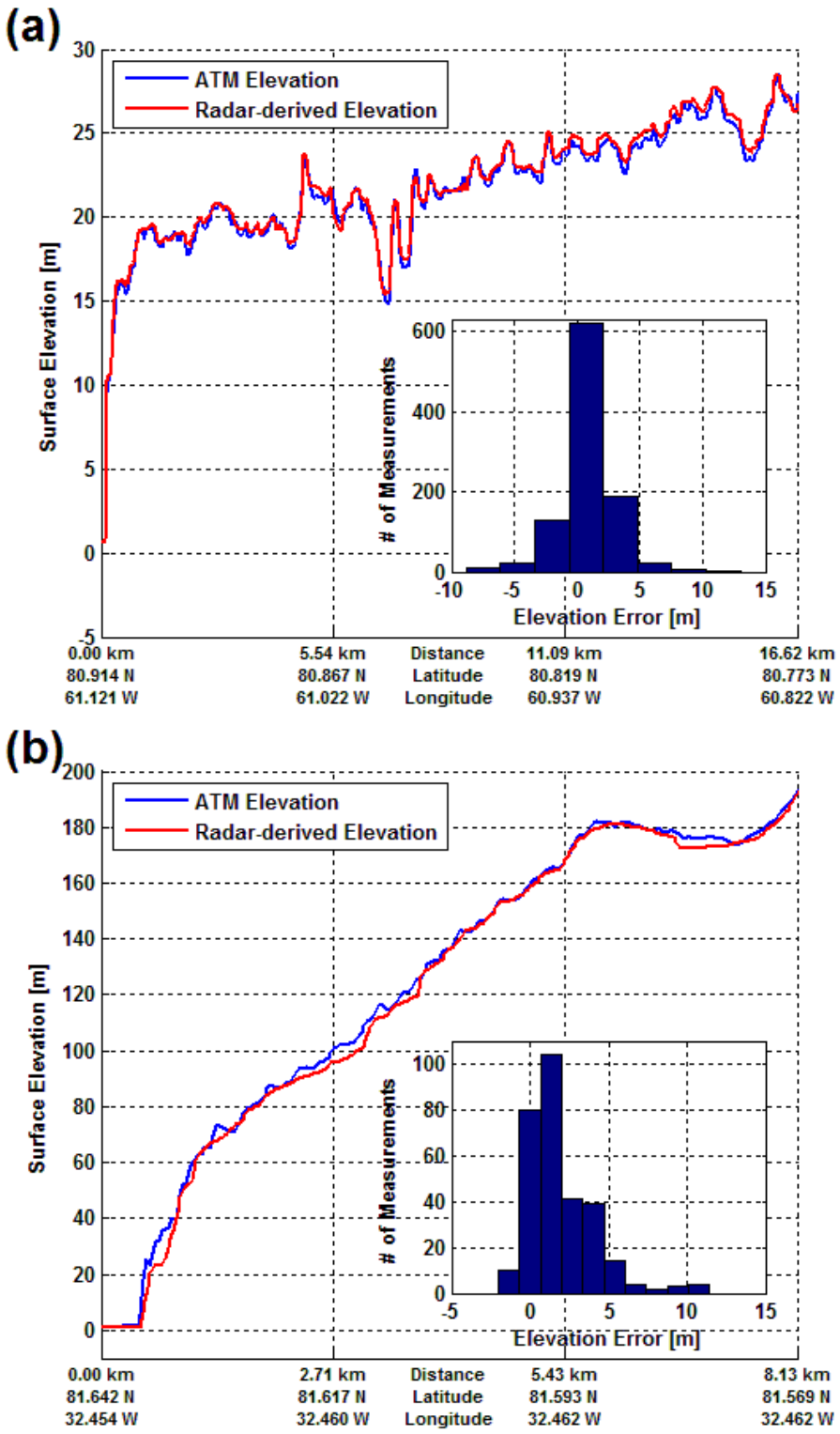

Figure 32. Comparing radar-derived surface elevations to ATM elevations for (a) Petermann glacier and (b) Academy glacier in northern Greenland. Inset histograms show the distribution of elevation error between the two instruments.

Chapter 4: Estimation of ice shelf melt rates

4.1 Background on Petermann Glacier

A central goal of this work is to demonstrate the ability to estimate ice-shelf basal melt rates using radar data, separating the effects of ice motion and surface mass balance. This study will focus on Petermann Glacier (referred to as PG through the remainder of this document) in northwest Greenland. The drainage and speed of PG have made it a prime target for study over recent decades. The plethora of data, particularly repeat penetrating-radar data, made it an obvious choice for this study. PG is a fast flowing, marine-terminating glacier responsible for ~69,000 km^2 of the Greenland ice sheet, or roughly 4% [Rignot and others, 2001]. PG lost over 40% of the ice-shelf area in two significant calving events in 2010 and 2012 [Johnson and others, 2011; Nick and others, 2013; Münchow and others, 2014]. The shelf terminuses lie ~56 km and ~45 km seaward of the grounding line in 2011 and 2013, respectively. Previous studies have reported an average shelf thickness of ~300 m, increasing to a thickness of ~600 m at the grounding line [Rignot and Steffen, 2008; Münchow and others, 2014]. PG moves toward the ocean at a reported average rate between 0.95 km/yr [Higgins, 1991] and 1.1 km/yr [Rignot and Steffen, 2008] with little seasonal modulation [Nick and others, 2012]. Annual surface accumulation has been reported to be negligible [Münchow and others, 2014], and the surface has been reported to have net mass loss of ~1.2 m/yr through winter sublimation and summer melting [Rignot and others, 2001; Rignot and Steffen 2008]. Previous studies have reported steady-state basal melt rates based on satellite altimeter-derived [Rignot and Steffen, 2008] and airborne laser-altimeter derived [Krabill and others, 2002] ice flux divergence and moderate bandwidth ice penetrating radar profiles

[Gogineni and others, 2001; Rodriguez-Morales and others, 2013]. Reported values have ranged from ~30 m/yr near the grounding line to ~10 m/yr at the shelf terminus [Münchow and others, 2014].

4.2 Data set

Data on nearly identical flight lines were collected as part of the OIB mission in the springs of 2011, 2013, and 2014. Flights were conducted on May 7th, 2011; April 20th, 2013; and May 12th, 2014. This provides time deltas of 714 and 387 days. The thickness change estimates discussed below are divided by these time deltas to estimate per-year rates. Figure 33 shows a map of the flight line position along the glacier ice-shelf. For the purposes of this study, we have restricted the view to the floating ice-shelf portion of the glacier, starting at the grounding line and extending to just beyond the 2011 terminus. The position of the grounding line is represented by the southernmost point of the flight lines seen in Figure 33.

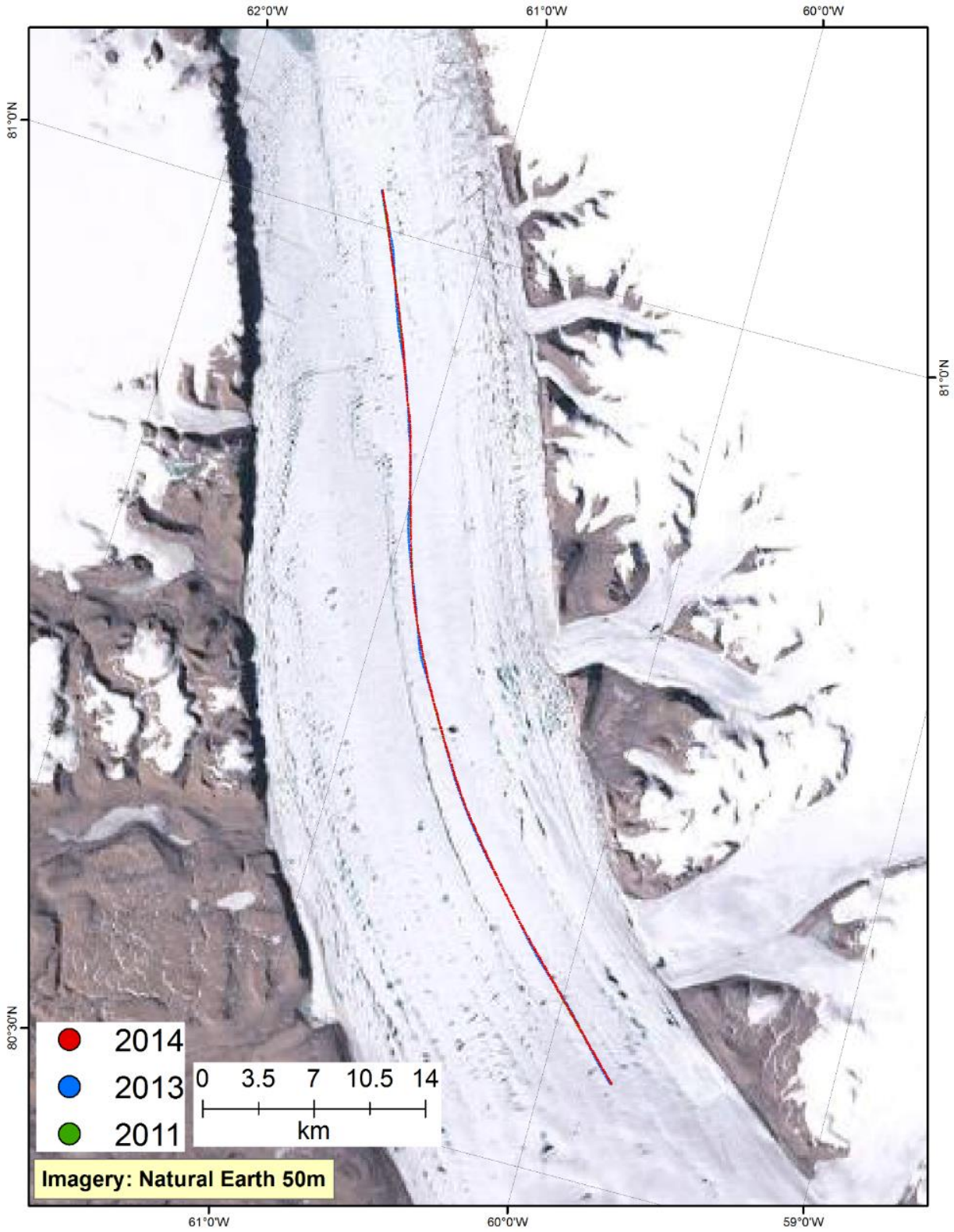

Figure 33. Satellite imagery of Petermann glacier with flight line overlays. The southern (bottom) edge of the flight line represents the approximate position of the grounding line.

Analysis was performed on the UHF radar data collected along these flight lines. Surface and basal interfaces were tracked using a local maximum tracker on the received power data matrix. A bright internal interface was tracked, where possible; this interface is assumed to be stable between measurement campaigns and is used to separate surface and basal melting from overall thickness changes. Analyses of thickness changes, surface and basal melt rates, and velocity will be presented, discussed, and compared with recent results presented in the literature. The results will be compared to hydrostatic balance calculations using both radar and ATM elevations.

4.3 Initial analysis

Before comparing data from each measurement campaign (i.e. 2011 to 2013 and 2013 to 2014), some steps were required to ensure a direct comparison in both the along-track and depth dimensions. Platform elevation changes were removed. Record window start time biases were removed using the open ocean surface as a reference. Platform velocity variations were removed using a spline interpolation in the slow-time dimension. Inter-campaign fast-time sampling frequency variations were removed using a spline interpolation in the fast-time dimension.

Figure 34 shows an echogram of the Petermann glacier ice-shelf as it appeared in the spring of 2011. An initial visual evaluation indicates the clear presence of definitive surface and basal returns with prominent internal layering near the surface. The basal interface has a disjointed appearance, suggesting the presence of significant basal crevassing. The location of major basal crevasses is well correlated with the location of surface crevasses.

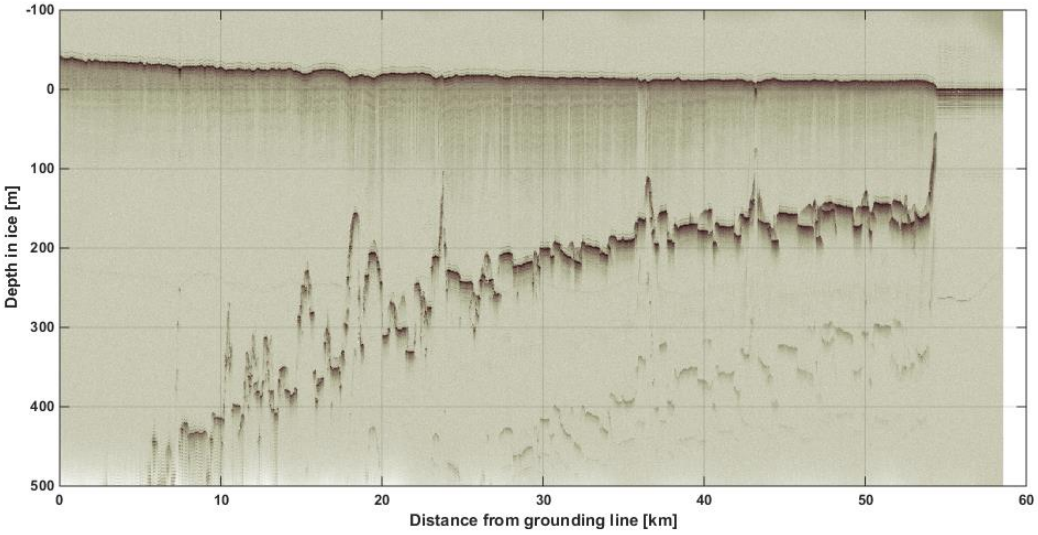

Figure 34. 2011 echogram of the Petermann glacier ice-shelf.

The crevasse seen at roughly 43 km in Figure 34 is the separation point of the major calving event that occurred during the summer of 2012 [Münchow and others, 2014]. This correlation suggests that these surface/basal crevasse pairs could indicate separation points of future calving events. Examples occur at roughly 38 km, 25 km, 20 km, and 9 km in Figure 34.

4.4 Ice draft and thickness profiles

Ice-shelf thickness profiles were generated for each year by tracking the surface and basal interfaces using a local maximum tracker on the radar received power matrix (echogram). To provide a more complete context compared to other studies of PG in the literature, thickness profiles were also generated from the radar and ATM-derived surface elevations by calculating the ice draft assuming hydrostatic equilibrium.

Figure 35 shows the radar-tracked interface profiles for each of the three measurement years (2011, 2013, and 2014) as they appeared at the time of measurement relative to the fixed along-track coordinate system. The along-track coordinate system follows the flight line, and

the flight lines are intended to follow a flow streamline of the glacier. The intended consequence is that it can be assumed that a parcel of ice advect only in the along-track dimension. The left edge of the graph represents the position of the grounding line. Basal interface returns in the radar set became sparse within 9 km of the grounding line. Basal returns for the remaining 9 km to the grounding line were tracked using the data collected by the Multi-Channel Coherent Depth Sounder/Imager (MCoRDS/I) [Rodriguez-Morales and others, 2013].

Average flow velocities of 1.14 km/yr and 1.2 km/yr during the periods of 2011 to 2013 and 2013 to 2014, respectively, were found by aligning significant features. This represents an average acceleration of 60 m/yr during the 3-year study period. This is a significant acceleration in flow in relation to the reported average flow velocities 0.95 km/yr in 1991 [Higgins, 1991] and 1.1 km/yr in 2008 [Rignot and Steffen, 2008]. A more thorough evaluation of shelf velocities is discussed later. Figure 36 shows the alignment of the studied profiles using the average flow velocities; the 2011 profile was kept stationary in the along-track coordinate system. There is significant correlation among basal crevasse features suggesting that these features likely form in the vicinity of the grounding line and advect largely unaltered, with the exception of melt on the surfaces exposed to seawater.

Shelf thickness ranges from ~170 m at the ice front to ~500 m at the grounding line, assuming a constant ice density of 917 kg/m^3 (dielectric constant, n = 3.15). Since the shelf maintains the same general profile with time, a first-estimate, linear, steady-state, along-track thinning rate of $\partial H/\partial y$ = 10 m/km can be inferred. When multiplied with the shelf velocity, a steady-state melt rate ($\partial H/\partial t$) can be estimated. Between 1991 and 2014, the steady-state

melt rate increased from roughly 10 m/yr to 12 m/yr. This will be discussed in detail in section 4.5.

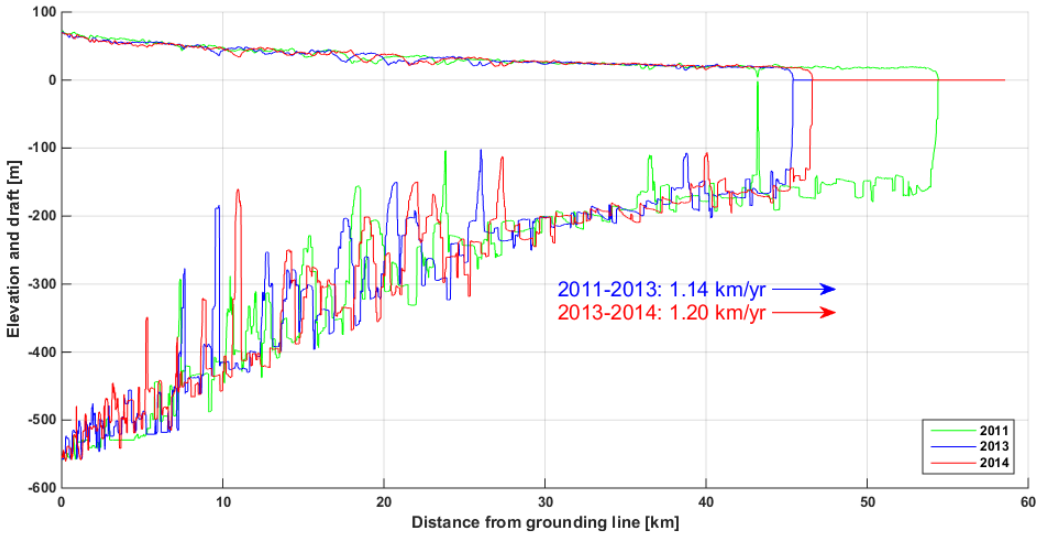

Figure 35. Elevation and draft of Petermann glacier ice-shelf as is appeared during each spring measurement campaign relative to a fixed coordinate. The left edge of the graph represents the position of the grounding line. Average velocities are shown.

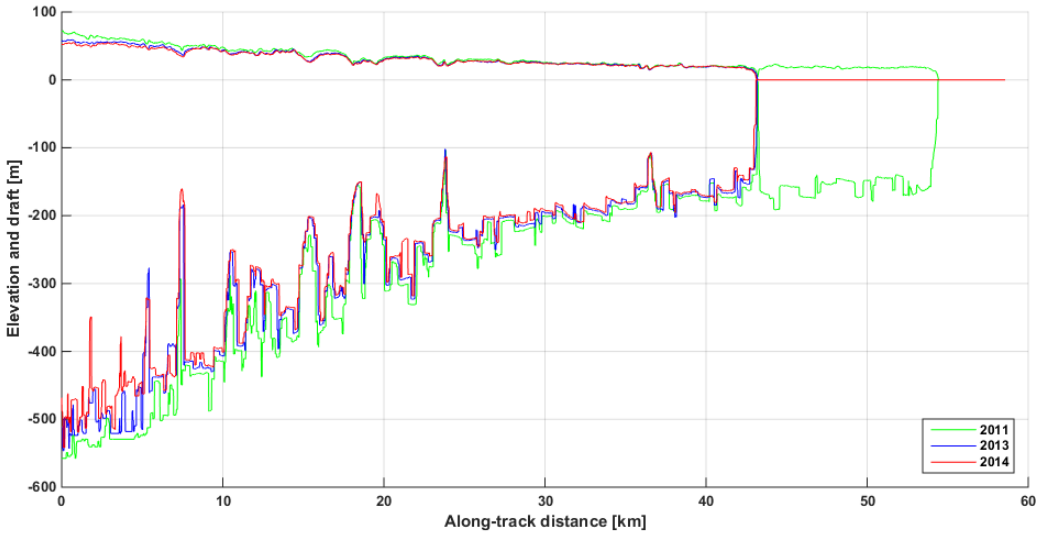

Figure 36. Elevation and draft of Petermann glacier ice-shelf with the 2013 and 2014 profiles shifted to align major features. The 2011 trace has been kept stationary within the coordinate system.

Previous studies of PG in the literature have relied heavily on surface elevation measurements and the hydrostatic equilibrium assumption to monitor shelf thickness [Rignot, 1996; Rignot and Steffen, 2008; Nick and others, 2012; Münchow and others, 2014]. The hydrostatic condition of the shelf can be examined by applying the relationship:

$$Z = \left(1 - \frac{\rho_i}{\rho_w}\right) H + \frac{\rho_i}{\rho_w} h_a$$

where Z is the surface elevation above the geoid (i.e. ocean surface), H is the total shelf thickness, and ρ_i and ρ_w are the densities of ice and seawater, 917 kg/m^3 and 1026 kg/m^3, respectively. The additional term represents a firn/air correction where h_a is the equivalent thickness of air within the firn [Bindschadler and others 2011]; this correction should be negligible for PG as annual snowfall is small compared to annual surface melting and sublimation [Münchow and others, 2014]. Figure 37 and Figure 38 show the observed and aligned shelf elevation and hydrostatic draft profiles, respectively. The general shape of the profile, basal features, and predicted mean velocities all agree well with the radar basal profile. From the aligned profile, it is clear that the hydrostatic assumption leads to greater predicted basal losses compared to the radar basal profiles, especially approaching the grounding line. This may suggest that hydrostatic balance is not a valid assumption near the grounding line and that using this assumption may over-predict basal melt rates.

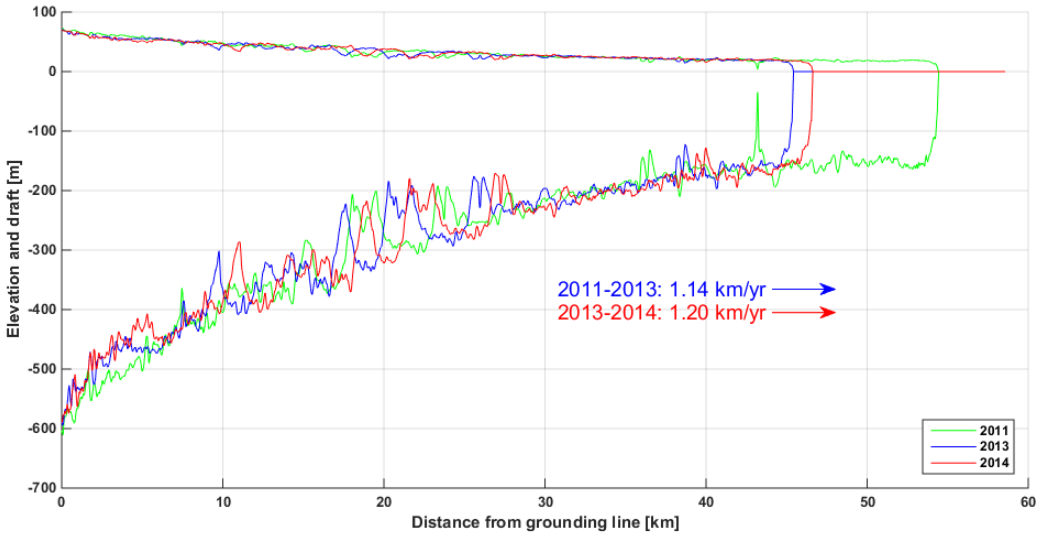

Figure 37. Elevation and draft of Petermann glacier ice-shelf as it appeared during each spring measurement campaign relative to a fixed coordinate. Ice draft was calculated using hydrostatic equilibrium. The left edge of the graph represents the position of the grounding line. Average velocities are shown.

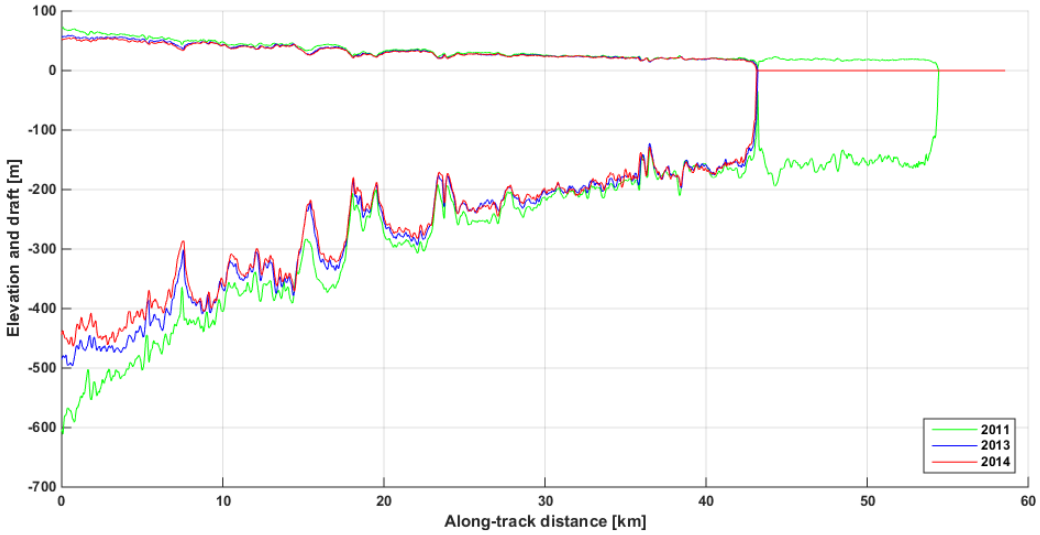

Figure 38. Elevation and draft of Petermann glacier ice-shelf with the profiles of 2013 and 2014 shifted to align major features. Ice draft was calculated using hydrostatic equilibrium. The 2011 trace has been kept stationary within the coordinate system.

Figure 39, Figure 40, and Figure 41 compare the radar-measured and hydrostatic-balance calculated ice draft for each year. In general, the ice-shelf can be said to be in hydrostatic balance, at least beyond 8 km from the grounding line. ATM surface elevation measurements

compared very well with radar measurements, and by extension, the hydrostatic basal interfaces. Mean error between ATM and radar surface elevations is ~3.3 cm, resulting in a mean hydrostatic basal error of ~0.55 m. ATM L2 elevation profiles were used [Krabill, 2015]. It is clear that the hydrostatic assumption breaks down on the smaller scale, as the vertical extent of many crevasses, and even the presence of smaller crevasses, are not reflected in the surface topography and therefore not well represented. The hydrostatic profiles also do not accurately predict the "blocky" nature of the basal interface. Hydrostatic equilibrium may well predict average basal melt rates, but would likely incorrectly predict small-scale melt rates, especially in the presence of significant crevasses.

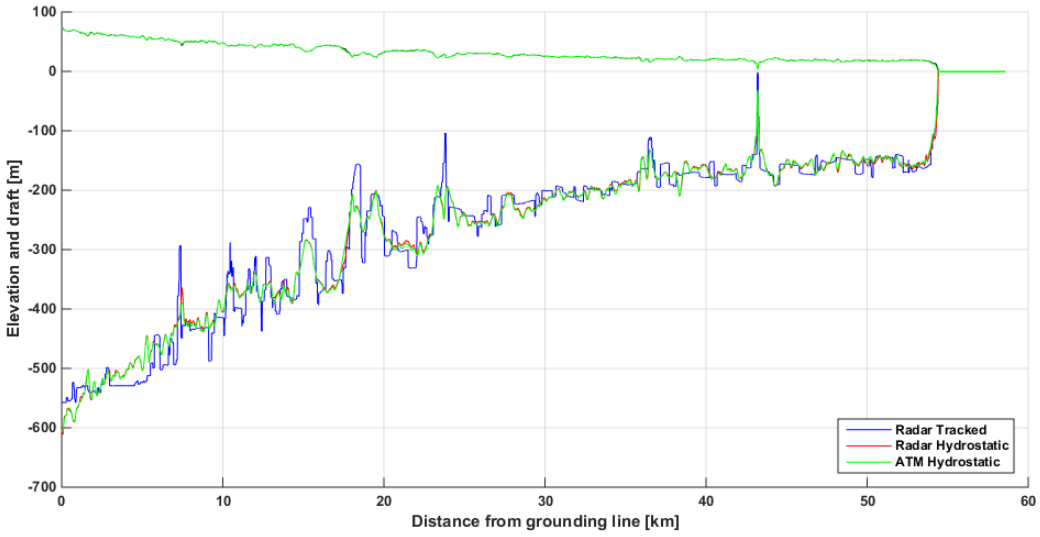

Figure 39. Radar-measured versus radar-derived hydrostatic versus ATM-derived hydrostatic ice draft for Petermann glacier as seen in 2011.

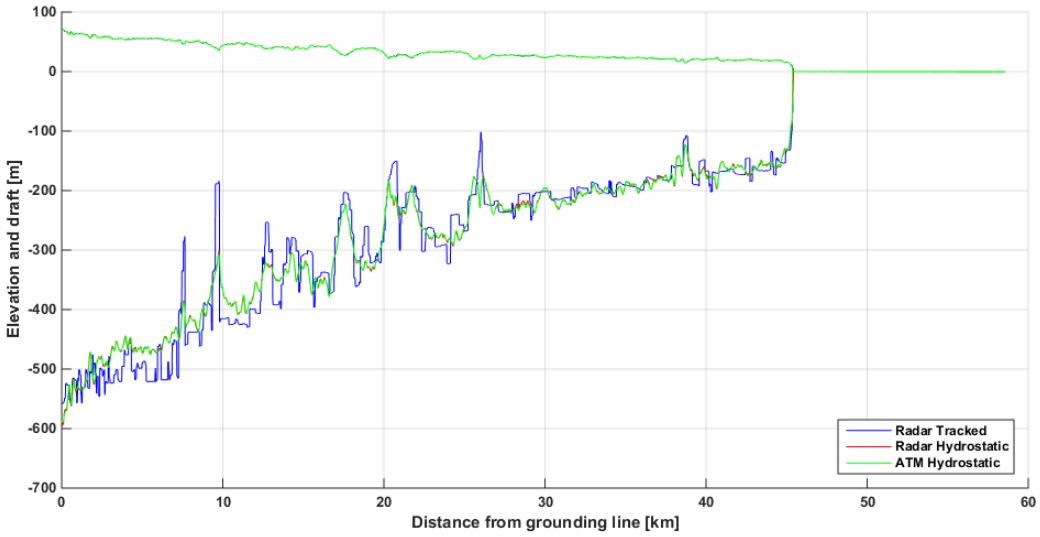

Figure 40. Radar-measured versus radar-derived hydrostatic versus ATM-derived hydrostatic ice draft for Petermann glacier as seen in 2013.

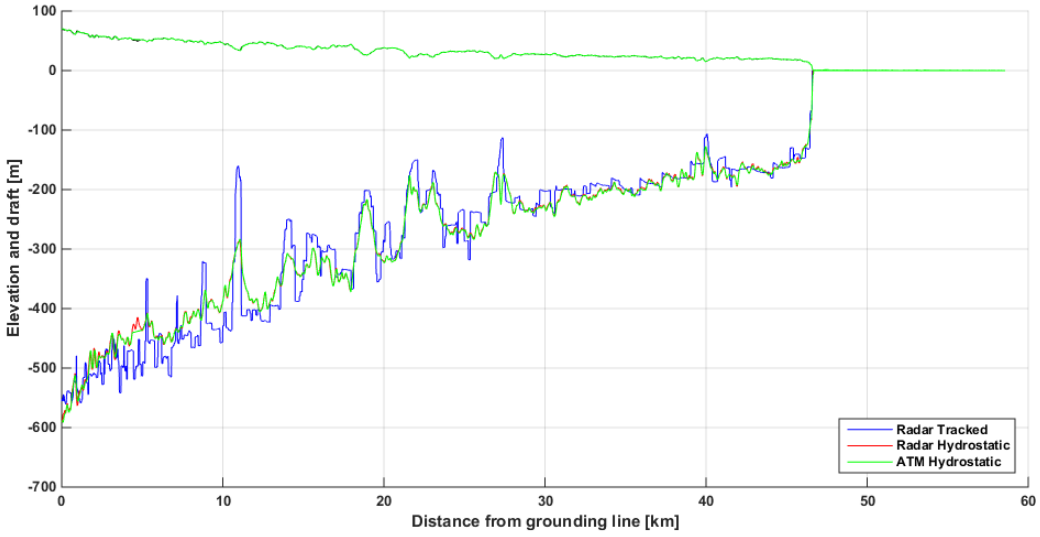

Figure 41. Radar-measured versus radar-derived hydrostatic versus ATM-derived hydrostatic ice draft for Petermann glacier as seen in 2014.

4.5 Thickness changes with time

The volumetric flow rate of ice-shelf mass can be described using the mass continuity equation, assuming a constant, vertically-averaged density:

$$\frac{\partial H}{\partial t} + \nabla(\vec{u}H) = \dot{a} - \dot{m}$$

where H is the ice thickness, $\vec{u} = (u, v)$ is the vertically averaged velocity vector with across-track and along-track dimension components u and v, $\dot{a}$ is the net surface mass balance, and $\dot{m}$ is the net basal mass balance. ∂H/∂t is the non-steady-state thickness change. The steady-state thickness change, $\nabla(\vec{u}H)$, can be rewritten as $\vec{u}\nabla H + H\nabla\vec{u}$. Cross-track flow is assumed to be negligible, reducing the mass flux divergence, $\vec{u}\nabla H$, to $v_0(\partial H/\partial y)$. Non-linear dynamic thinning, $H\nabla\vec{u}$, has been shown in the literature to be negligible [Higgins, 1991].

For any snapshot in time (∂H/∂t = 0) an ice-shelf exhibits a steady-state mass balance. The visible manifestation of this is the thinning trend of the shelf while moving in the along-track dimension from the grounding line to the ice front. Münchow and others [2014] defined an along-track cumulative average ice thickness profile to reduce the noise of point-by-point thickness comparisons:

$$\widehat{H} = \frac{1}{y_2 - y_1}\int_{y_1}^{y_2} H dy$$

where $\widehat{H}$ is the average ice thickness starting from a fixed point near the grounding line, y_1, to some point along the ice-shelf, y_2. Figure 42 and Figure 43 show the cumulative average thickness using both the tracked-interface radar thickness and the radar-derived hydrostatic thickness. As expected, the hydrostatic cumulative thickness is larger since the hydrostatic assumption over-estimates the shelf thickness near the grounding line. Both the tracked and hydrostatic thicknesses show the same general trend. From this "smoothed" perspective, it appears that the glacier was not in steady state (∂H/∂t = 0) between 2011 and 2013 and was nearly in steady state between 2013 and 2014.

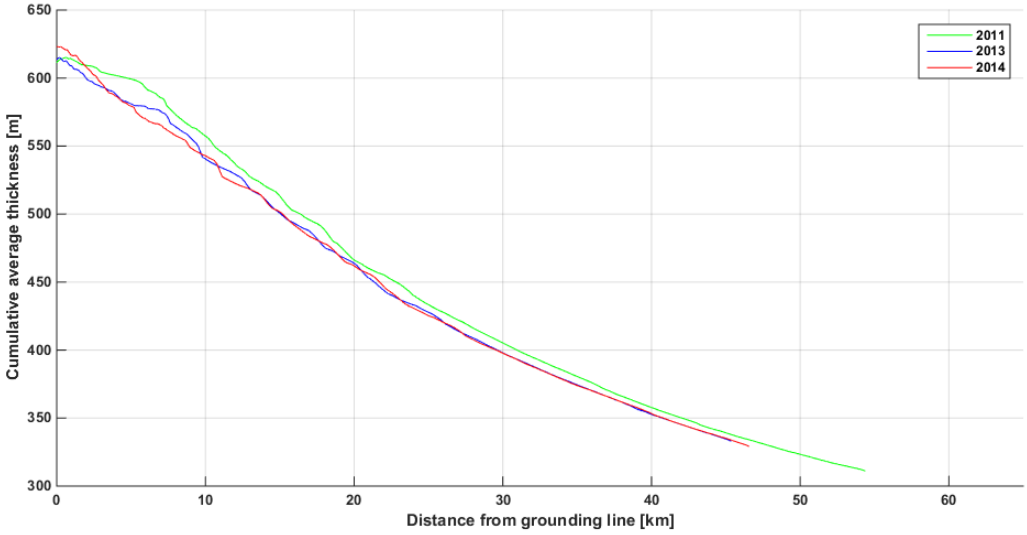

Figure 42. Cumulative average thickness using tracked radar thickness.

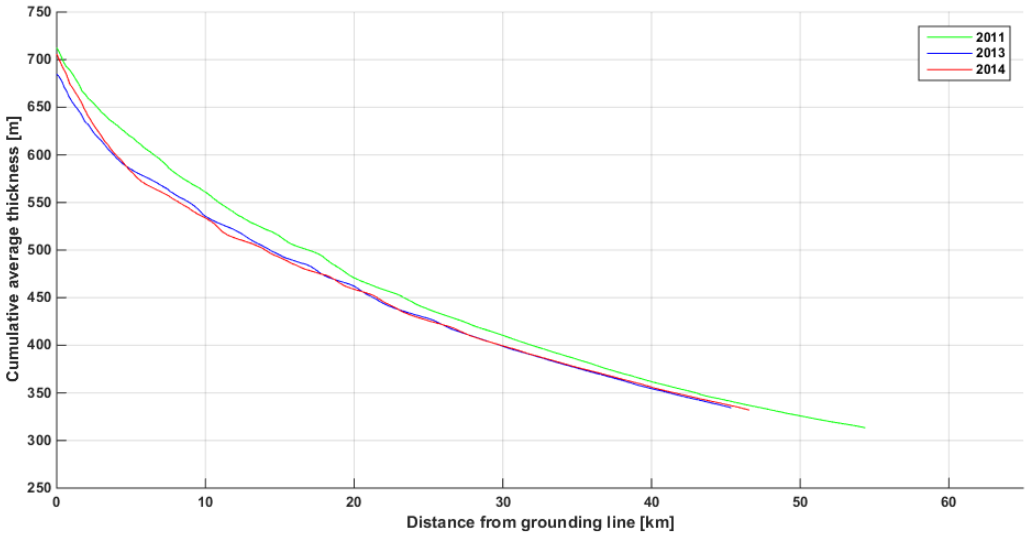

Figure 43. Cumulative average thickness using radar-derived hydrostatic thickness.

Figure 44 shows non steady-state melt rates (∂H/∂t) calculated from the cumulative average thicknesses above, with negative values indicating mass loss. The average non steady-state loss between 2011 and 2013 is 4.1 m/yr using the radar-tracked data, and 7 m/yr using the hydrostatic data. The hydrostatic overestimates the non steady-state melt rate by

more than a factor of two. The shelf was nearly in steady-state between 2013 and 2014 with an average loss of 0.7 m/yr using the radar-tracked data and an average loss of 1.1 m/yr using the hydrostatic data.

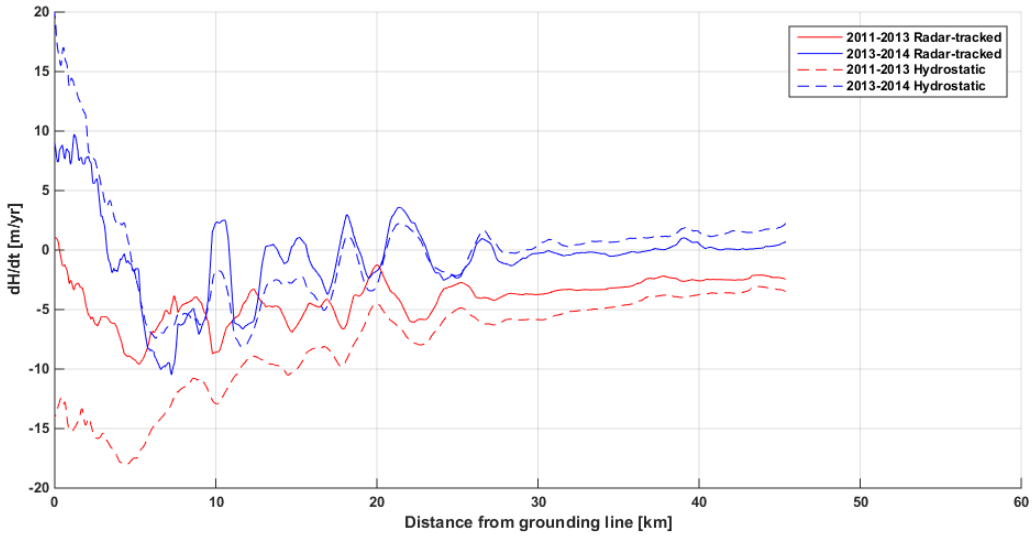

Figure 44. Non steady-state melt rates. Negative values indicate mass loss.

The mass flux divergence, $v_0(\partial H/\partial y)$, or steady-state mass balance, was estimated using the cumulative average thickness. Figure 45, Figure 46, and Figure 47 show the mass flux divergence for the years 2011, 2013, and 2014, respectively. The values shown are presented with mass loss as a positive value. The 2011-2013 average velocity was used for the 2011 and 2013 calculations and the 2013-2014 average velocity was used for the 2014 calculation.

In 2011, radar-tracked steady-state mass losses varied from ~3 m/yr at the ice front to ~10 m/yr within 5 km of the grounding line, decreasing to nearly zero at the grounding line. When the hydrostatic assumption is used, the steady-state mass loss erroneously increases to ~30 km/yr at the grounding line. As seen in the thickness values, the hydrostatic assumption appears to break down within ~10 km of the grounding line. Similar trends were observed in

2013 and 2014. Considering the ice front retreat due to the 2012 calving event, the ~4.5 km/yr steady-state mass loss observed at the ice front in 2013 and 2014 was also observed at the same location in 2011. Mass loss within 10 km of the grounding line increased in 2013 and 2014 compared to 2011. In 2013, mass loss appears to increase from ~4.5 km/yr at the ice front to ~8 km/yr at the grounding line. In 2014, mass loss appears to increase from ~4.5 km/yr at the ice front to ~10 km/yr at the grounding line. Again, hydrostatic balance appears to overestimate mass loss within 10 km of the grounding line. Increases in the mass loss and significant basal crevassing from year to year seen near the grounding line suggest an accelerated introduction of more heat from the underlying ocean. Mass loss and crevassing are likely not mutually exclusive and are also likely tied to the observed year-to-year increases in shelf velocity.

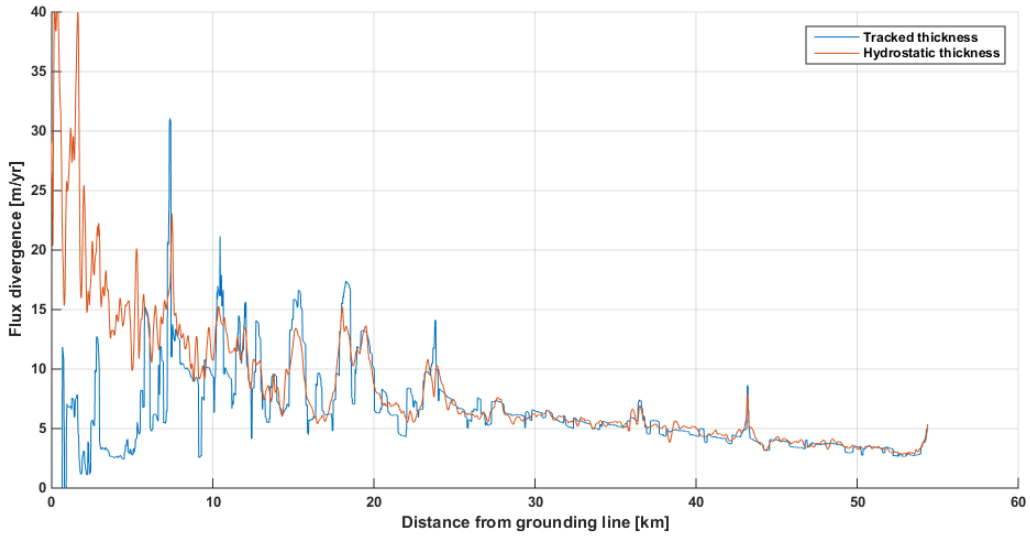

Figure 45. Petermann glacier mass flux divergence (steady-state mass balance) in 2011 using 2011-2013 estimated average velocity of 1.14 km/yr.

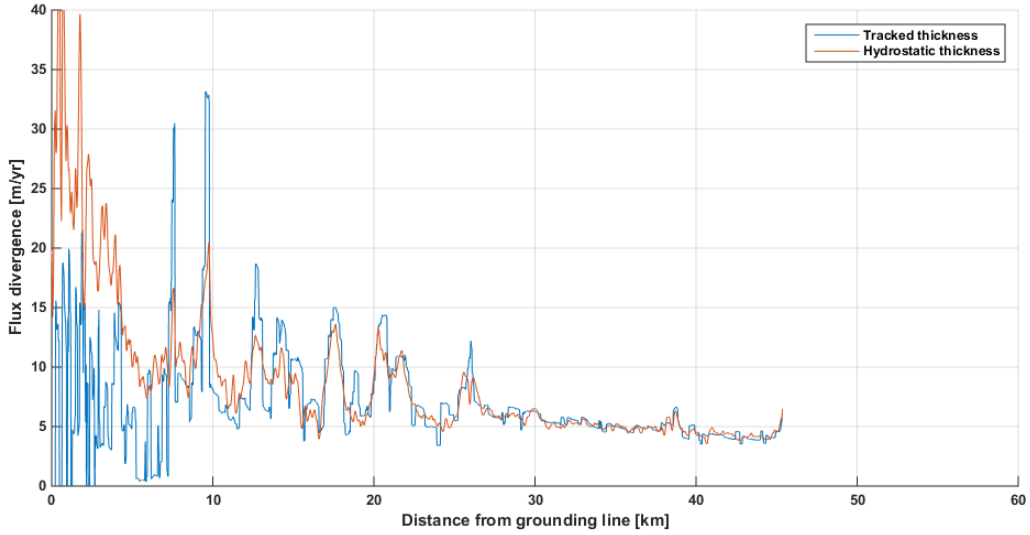

Figure 46. Petermann glacier mass flux divergence (steady-state mass balance) in 2013 using 2011-2013 estimated average velocity of 1.14 km/yr.

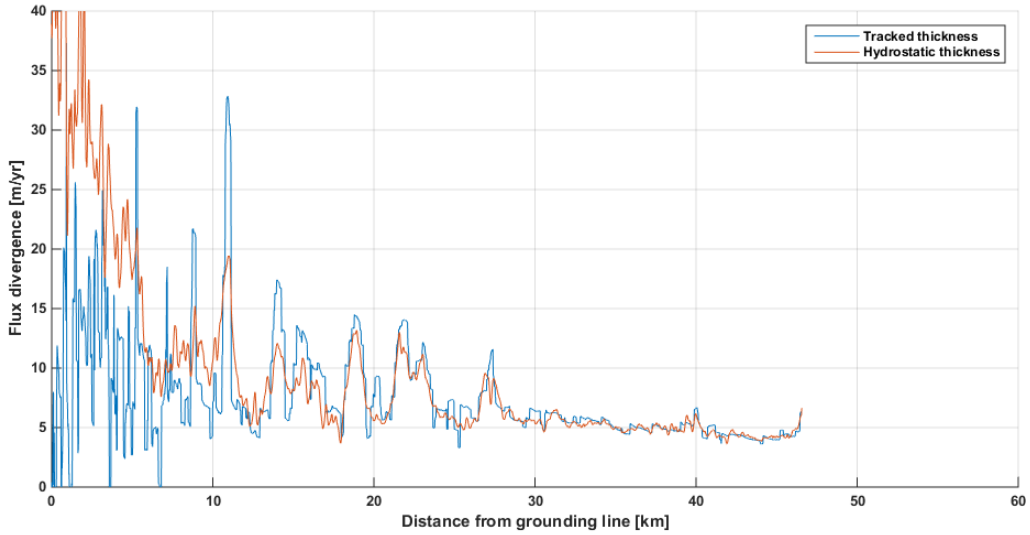

Figure 47. Petermann glacier mass flux divergence (steady-state mass balance) in 2014 using 2013-2014 estimated average velocity of 1.2 km/yr.

Total mass loss is a sum of the steady-state and non-steady-state mass losses. Figure 48 shows the total loss for the periods 2011-2013 and 2013-2014. The 2011-2013 data have been shifted based on the observed average velocity to highlight the alignment of significant melt features that have translated seaward over time. During the 2011-2013 period, the glacier was

not in steady state, while during 2013-2014 period the glacier was nearly in steady state. While in not in steady state, average thinning ranges from ~6 m/yr at the ice front to ~15 m/yr near the grounding line. While in steady state, these values decrease to ~4 m/yr at the ice front to ~12 m/yr near the grounding line. Significant variation in thickness loss occurs when approaching the grounding line. These variations are due to the presence of large crevasses where melt appears to occur both at the top and along the sides of the crevasse. This side-wall melt may be a combination of actual melt and stretching of the crevasses due to differential along-flow velocities. These large variations in thickness loss are often not seen in hydrostatic-based calculations as crevasses are often not in hydrostatic balance. Other results presented in the literature (Rignot and Steffen, 2008; Münchow and others, 2014) use a coarser resolution along-track spacing, dy = 50 m. While a finer along-track resolution, dy = 10 m, was used for this study, some smaller scale features may be still be lost or smoothed.

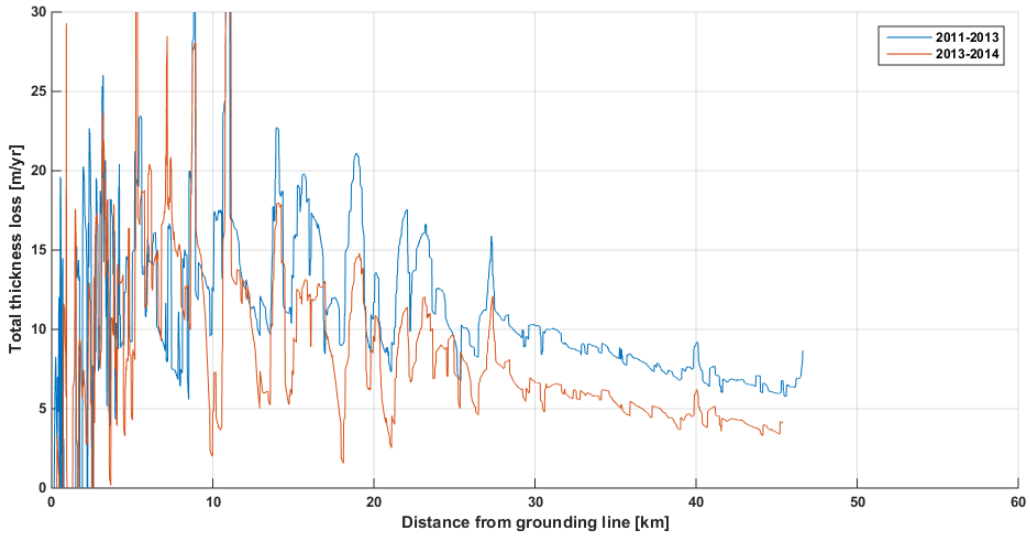

Figure 48. Total thickness losses, steady + non-steady thinning.

4.6 Surface and basal melt rates

To separate the surface net mass balance (accumulation + ablation) and basal net mass balance (melting + freezing), a stable internal layer was tracked and used as the origin plane. The ice-shelf was separated into two thicknesses, from the surface to the layer and from the latey to the bottom. The above analysis was repeated for these two thickness to evaluate the surface melt separate from the basal melt.

Figure 49 and Figure 50 show the surface melt and basal melt rates, respectively. Again, the 2011-2013 data have been shifted to highlight the alignment of melt features that have translated seaward with time. Surface melt rates for the 2011-2013 period ranged from ~1.1 m/yr at the ice front to ~5 m/yr at the grounding line. Surface melt rates were lower during the 2013-2014 period, ranging from ~0.4 m/yr at the ice front to ~4 m/yr at the grounding line. Average surface melts rates were 2.1 m/yr and 1.5 m/yr for the 2011-2013 and 2013-2014 periods, respectively. These values agree well with others reported in the literature [Rignot and other, 2001; Rignot and Steffen, 2008; Münchow and others, 2014]. Basal melt rates ranged from ~5 m/yr to ~17 m/yr during the 2011-2013 period and from ~3.5 m/yr to ~15 m/yr during the 2013-2014 period.

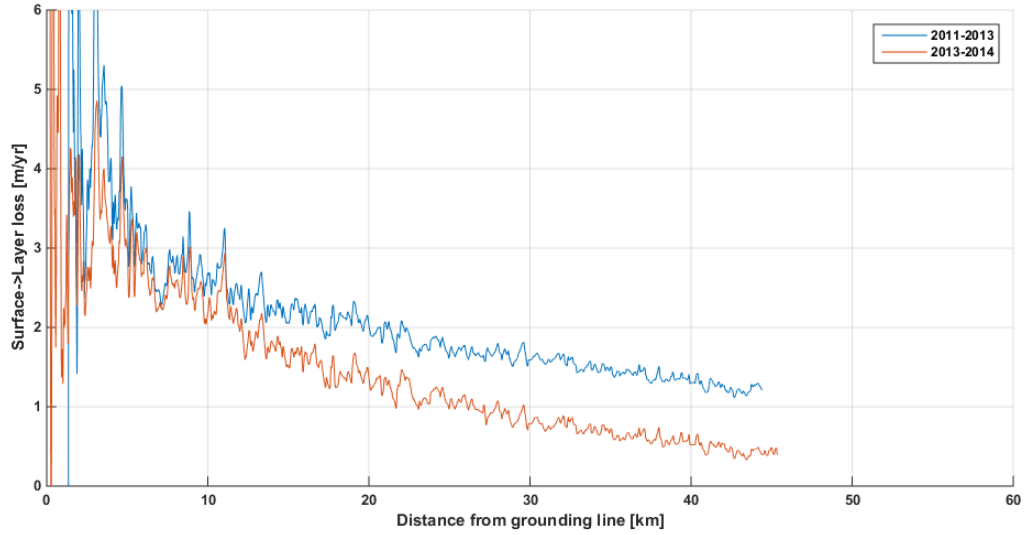

Figure 49. Total (steady + non steady-state) surface loss.

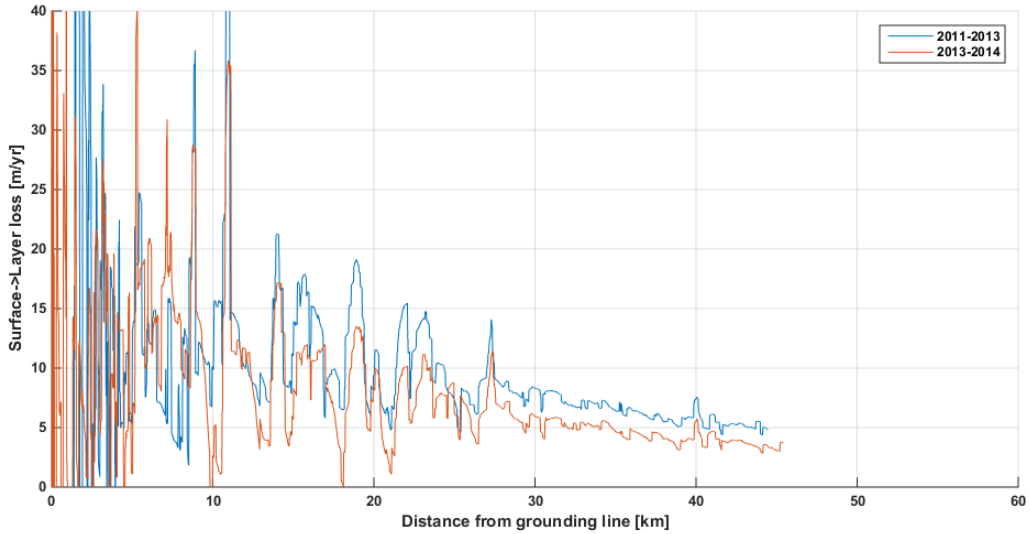

Figure 50. Total (steady + non steady-state) basal loss.

4.7 Velocity profiles

Shelf velocity as a function of along-track distance was examined in more depth. The surface profiles for each measurement pair (2011/2013 and 2013/2014) were cross-correlated. Each point along the profile was assigned the lag value with the strongest correlation for a neighborhood segment of each profile. The neighborhood window extended 5 km on either

side of the point in question; a maximum possible lag of 2.5 km was used. The same process was repeated for the basal profile. The section of the shelf that calved in 2012 was removed from the 2011 profile. Predicted surface and basal velocities differed on average by ~15 m/yr or ~1.3% of the mean shelf velocity; it can safely be assumed that any parcel of ice moved at the nearly the same velocity through the full depth. Figure 51 and Figure 52 show this correlation-based mean velocity for the time periods 2011-2013 and 2013-2014, respectively. A smoothed profile overlay was created using a 5 km window moving average. Velocity profiles mimic those reported in the literature [Rignot and Steffen, 2008; Münchow and others, 2014], where there is an increase in velocity up to roughly 12 km from the grounding line followed by a general decrease in velocity thereafter. Increases in velocity near the grounding line may influence the formation of basal crevasses through along-glacier stretching. Suspect crevasse side-wall melting and stretching/compression leads to some along-track ambiguity in the alignment of crevasses through correlation; this ambiguity leads to the “spikey” nature of the velocity profile.

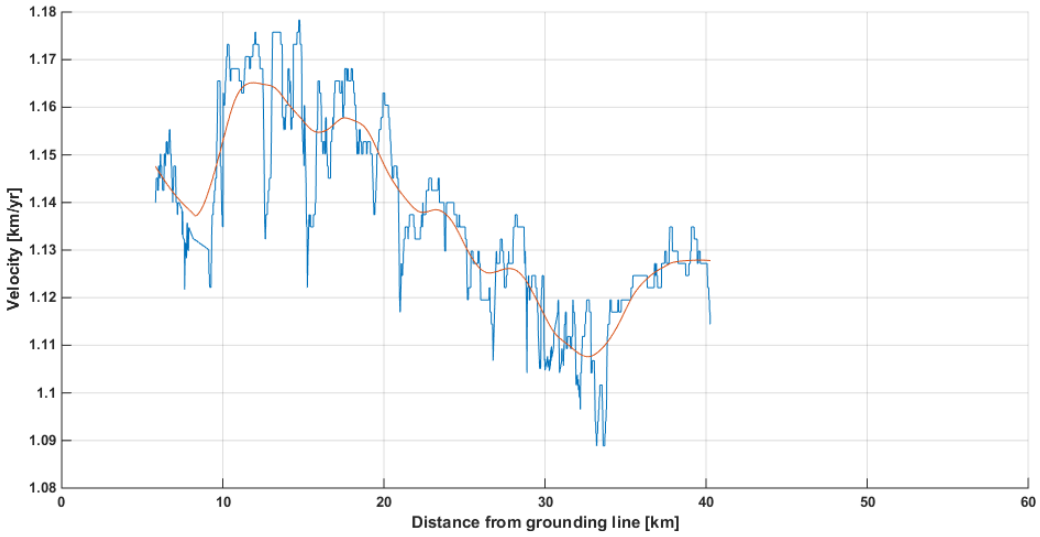

Figure 51. Mean velocity of Petermann glacier as calculated by correlating surface and basal features between 2011 and 2013. A smoothed curve is overlaid.

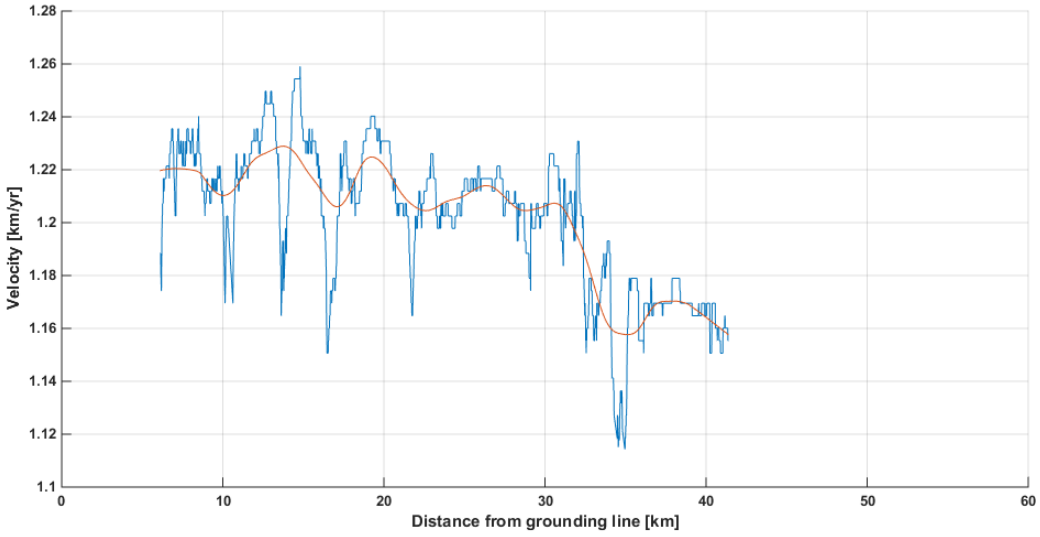

Figure 52. Mean velocity of Petermann glacier as calculated by correlating surface and basal features between 2013 and 2014. A smoothed curve is overlaid.

4.8 Summary and discussion

Melt rates for the Petermann glacier floating ice-shelf were examined. Changes in thickness were evaluated using radar-tracked surface and basal interfaces. This study uses UHF radar data with a vertical resolution of ~0.43 m in ice, providing a clear picture of the basal interface

and allowing for the tracking of a stable internal layer, which serves as the basis for the separation of surface from basal melt. Previous studies [Rignot and Steffen, 2008; Münchow and others, 2014] have also evaluated this ice-shelf using VHF radar data with a vertical resolution of ~5.6 m in ice. Many previous studies [Rignot and others, 2001; Münchow and others, 2014] evaluated ice-shelf mass loss by using fine-resolution surface altimetry and applying the hydrostatic condition to estimate thickness. Shelf along-track velocity was examined by correlating surface and basal features. Comparisons between years were done after removing the section of the shelf that calved in 2012.

Figure 53, Figure 54, and Figure 55 show the total radar-tracked versus hydrostatic shelf thickness for 2011, 2013, and 2014, respectively. Using the hydrostatic assumption does not accurately capture small-scale crevasses and, by extension, shows that these crevasses are not in hydrostatic balance. In general, the shelf appears to be in hydrostatic balance beyond 20 km from the grounding line. Between 10 and 20 km from the grounding line, the hydrostatic assumption appears to slightly overestimate the thickness of the shelf. Between 2 and 10 km from the grounding line, the hydrostatic assumption appears to greatly underestimate the thickness of the shelf. Results presented earlier show that the hydrostatic assumption overestimates year-to-year thickness losses within ~8 km of the grounding line.

All thicknesses, both radar-tracked and hydrostatic, were calculated assuming no surface snow or firn correction. Regardless of the thickness estimation method, a firn correction would result in a thinner estimate. The results presented have shown significant differences between the radar-tracked and hydrostatic thickness. No constant bias was found along the length of the ice-shelf, and a firn correction would need to be applied to both thickness estimation

methods; therefore, the differences between the radar-tracked and hydrostatic thickness estimates cannot be reconciled by simply including a firn correction.

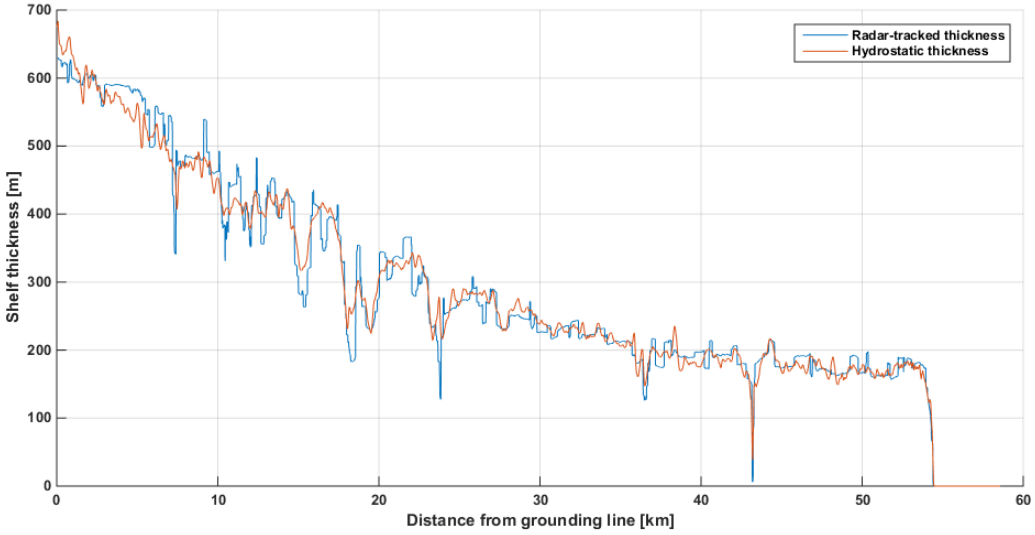

Figure 53. Petermann ice-shelf thickness, 2011, radar-tracked versus hydrostatic.

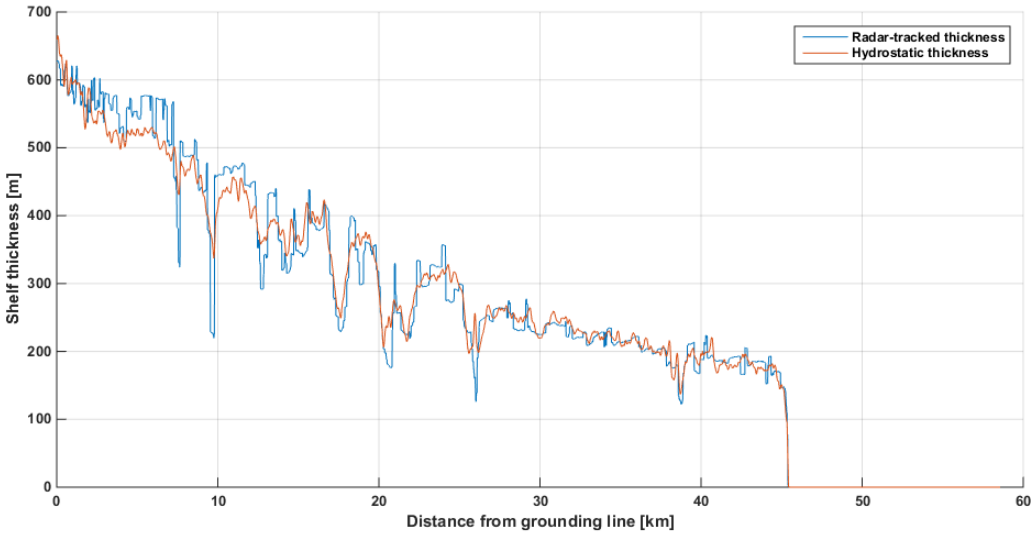

Figure 54. Petermann ice-shelf thickness, 2013, radar-tracked versus hydrostatic.

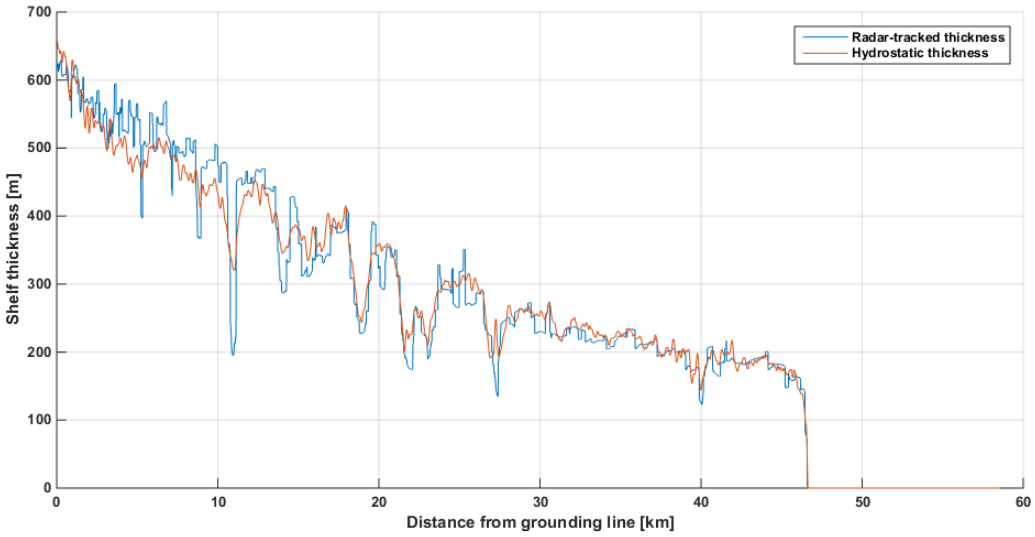

Figure 55. Petermann ice-shelf thickness, 2014, radar-tracked versus hydrostatic.

Table 5 summarizes the pertinent ice-shelf parameters determined by this study with comparison parameters from similar previous studies reported in the literature. Table 6 summarizes the average surface and basal melt rates measured with the UHF radar. Overall, flux divergence measurements compare well between methods and are fairly constant from year to year. Significant temporal variation in non steady-state melting is clearly the dominant factor in shelf mass loss. Results presented here and by Münchow and others [2014] suggest that the ice-shelf enters periods of significant non steady-state melting following large calving events, such as those observed in 2010 and 2012.

Table 5. Comparison of average ice-shelf melt parameters.

	Year	$v_0(\partial H/\partial y)$ [m/yr]	∂H/∂t [m/yr]	Total [m/yr]	Velocity [km/yr]
UHF radar-tracked thickness	2011-2013	7.6	4.1	11.7	1.14
	2013-2014	7.8	0.7	8.5	1.2
UHF radar hydrostatic thickness	2011-2013	7.3	7	14.3	
	2013-2014	7.4	1.1	8.5	
ATM-derived hydrostatic thickness [Münchow and other, 2014]	2007-2010	8	5	13	1.25
VHF radar thickness [Rignot and Steffen, 2008]	2002			7	1.1
Flux-gate [Rignot and others, 2001]	1999	8.4	0.8	9.2	

Table 6. Average surface and basal melt rates.

Year	Surface melt [m/yr]	Basal melt [m/yr]
2011-2013	1.8	9.7
2013-2014	1.2	7.5

The following items appear to be the major results of this analysis:

1. In general, the ice-shelf is in hydrostatic balance seaward of 20 km from the grounding line. Zones within 20 km of the grounding line where radar-tracked and hydrostatic thicknesses do not agree suggest that the shelf has some inertia following its decoupling from the bedrock and some time is required for it to reach a general hydrostatic equilibrium.
2. The basal interface of the ice-shelf is heavily crevassed, and hydrostatic equilibrium-derived thickness estimates do not fully capture the number and magnitude of the crevasses.
3. Seaward accelerations jumped from ~4m/yr^2 between 2002 and 2013 to 60 m/yr^2 from 2013 to 2014.

4. Steady-state melt rates appear to be relatively constant with time, but non-steady-state melt rates appear to jump significantly following a major calving event.

Chapter 5: 3D imaging of ice shelves

Three-dimensional tomographic imaging using the *MU*ltiple *SI*gnal *C*lassification (MUSIC) algorithm has been shown to image the ice-bed interface in 3D space using data collected using the CReSIS VHF depth-sounding radar [Paden and others, 2010]. For this study, the goal is to evaluate if this technique can be applied to image the ice-bed interface of shallow ice by using data collected with the aforementioned UHF radar. The technique, assumptions, and limitations will be discussed. Results from ground-based experiments in Antarctica will be presented. Parallel and perpendicular tracks will be used to verify the data for self-consistency.

For any particular ground/ice-penetrating radar that uses a chirped waveform, the three-dimensional position of a reflective target is ambiguous within a sphere centered at the phase center of the radar system. The initial coordinate system will describe the target position is a polar coordinated system: range, elevation angle (along-track angle from nadir), and azimuthal angle (cross-track angle from nadir). Directional antennas pointed nadir reduce the maximum extent of the along- and cross-track angle domains from ±180° to ±90°. The following general processing steps are used to resolve target ambiguity within this initial coordinate system: range migration, along-track resampling, along-track migration, cross-track direction of arrival estimation.

Many, including Goodman and others [1995] and Moses and others [2004], have discussed the challenges related to processing of wide-bandwidth, wide-aperture, synthetic aperture radar (SAR) data. Many of these issues arise from the shortcuts and approximations used in narrow-bandwidth, narrow-aperture, conventional SAR processing algorithms, which are only appropriate for the imaging of sets of isotropic point scattering centers. These shortcuts and

approximations include assuming the scattering does not have any frequency or viewing angle dependence, assuming far-field, plane-wave propagation. For wide-bandwidth and wide-aperture measurements, the angular-dependent and frequency-dependent nature of the scatters becomes significant and cannot be ignored, this is typically called fading. The choice of processing algorithm is critical to producing useful and accurate imagery under such circumstances. Frequency-wavenumber migration (f-k migration) is an effective and efficient processing method that accounts for these wide-bandwidth and wide-aperture issues and will be used for migration in the along-track dimension. Advanced parametric processing methods, such as the algorithm used for cross-track migration in this study, do not effectively account for these issues and is further discussed in Section 5.5. Recommendations for effective solutions are discussed in Chapter 6.

5.1 Range migration and along-track resampling

Prior to range migration, a boxcar averager is applied to the data. This is applied to reduce the data volume to ease the more computationally-intensive and time-consuming image processing later on, and to smooth the data based on the assumption that an average of a small number of adjacent points is a better measure of a signal than any of the individual points, improving the SNR. Following averaging and decimation, a Tukey window is applied to each record; a Tukey window is used instead of a Hanning window to preserve bandwidth. Range migration, also referred to as pulse compression or matched filtering, is performed by multiplying the data record with an ideal and windowed reference function in the frequency domain.

The along-track migration algorithm assumes that the data have been collected along a straight path. Manual identification will be used to separate straight (and quasi-straight) radar paths from turns to ensure that only straight radar paths are passed through the image processing steps. Since the along-track migration algorithm performs operations in the frequency domain via Fast Fourier transforms (FFTs), uniform spatial sampling is also required. For the ground-based system, the platform velocity is not constant and the radar PRF is not slaved to the platform velocity, therefore the along-track sampling is not uniform. Paden [2006] gave sufficient treatment to this problem by framing the issue as a complex spectral estimation problem. Three spectral estimation schemes were examined: matched filtering, linear minimum mean squared error estimation (MMSE), and spline interpolation. Results using simulated data showed that the MMSE and spline interpolation methods provided the lowest mean-squared error. The spline interpolation is better because of its computational efficiency and will be the method used to resample the radar data in the along-track.

5.2 Along-track migration

For a radar system whose nadir-pointing antenna has a beamwidth in the along-track dimension greater than zero, there exists ambiguity in the elevation angle of the received energy from the target because the only known position after pulse compression is the target range. This means that multiple targets that are at the same range from the radar, but lie at different depth and along-track distances will appear to come from the same location. This degrades the along-track resolution. By observing a family of targets (assuming those targets are stationary) from multiple radar positions in the along-track, their elevation angles can be determined from their phase histories, due entirely to range variations between successive

observations. This is the goal of along-track migration, also known as synthetic aperture processing, with the along-track motion forming the synthetic aperture. Fine along-track resolution can be achieved through along-track migration.

Frequency-wavenumber migration (f-k migration) will be applied here as it is more computationally efficient in comparison to space-time domain migration algorithms such as side-looking synthetic aperture radar (SAR). This advantage is primarily because the convolution operations performed in the space-time domain are more computationally intensive than the multiplicative operations performed in the frequency-wavenumber domain; f-k migration and space-time SAR are equivalent processing schemes carried out in their respective domains. The multi-dimensional FFT used for f-k migration requires that the data be sampled evenly in both space and time. The along-track resampling previously discussed evenly samples the data in the along-track space and the radar ADC provides uniform time sampling (depth dimension).

To explain the f-k migration algorithm, we begin by restricting the discussion to one dimension of travel. Assume a plane-wave is traveling in the positive x-direction. Since the direction of travel is unambiguous, the signal can be completely described by its frequency response and is recorded by a receiver positioned at x = 0, $s_0(t)$. If we were interested in the signal as it would be recorded at any point along the x-axis, $s_x(t)$, we would simply add the appropriate time delay based on the distance from the origin and the velocity, v, of the wave in the medium:

$$s_x(t) = s_0\left(t - \frac{x}{v}\right)$$

This corresponds to a phase shift in the frequency domain:

$$S_x(f) = S_0(f)exp\left(\frac{-j\omega x}{v}\right) = S_0(f)e^{jk_x x}$$

where $k_x = -\omega/v$, the angular wavenumber in the positive x-dimension. More broadly put, we can shift the signal at any point along the x-axis, and $S_x(f)$ by multiplying it with an appropriate phase shift, $e^{jk_x x}$. To find the value of the signal at zero-time, at a particular position x, we sum all of the frequency components together; this is essentially an inverse Fourier transform:

$$s_x(t=0) = \int_{-\infty}^{\infty} S_x(\omega)exp(j\omega \cdot 0)d\omega = \int_{-\infty}^{\infty} S_x(\omega)d\omega$$

Since our data will be discretized:

$$s_x(0) = \frac{1}{N}\sum_{n=0}^{N-1} S_x(n)exp(j\omega n \cdot 0) = \frac{1}{N}\sum_{n=0}^{N-1} S_x(n)$$

We can generalize this to three dimensions. The three-dimensional wavenumber is of the form:

$$\boldsymbol{k} = \frac{\omega}{v} = \sqrt{k_x^2 + k_y^2 + k_z^2}$$

Where k_x, k_y, and k_z in this case are defined in their respective right-hand Cartesian coordinate dimensions with the positive z direction pointing up (coming out the ice) and the positive x direction pointing in the positive along-track dimension (direction of travel). For this analysis, each cross-track receive channel will be migrated individually. This is driven by the choice of cross-track migration algorithm and will be discussed further in that section. It is known that the received signal originates from a yet-to-be-determined azimuth (cross-track) angle, but for the along-track migration, it is assumed that all energy is originating from nadir,

and this it can be assumed that $k_y = 0$. We can determine k_x based on the along-track sampling and solve for k_z:

$$k_z(\omega, k_x) = \sqrt{\left(\frac{\omega}{v}\right)^2 - k_x^2}$$

where k_z defines our incremental phase shift in the depth dimension, $e^{jk_z z}$.

The two-dimensional radar data matrix, in space (x) and time (depth), can be converted to the frequency-wavenumber domain with a two-dimensional FFT. Each element of the resulting matrix is associated with a particular ω and k_x. The f-k migration algorithm works by "moving" the radar through each possible target positions of interest (depths) using phase shifts (k_z) and then capturing the zero-time signal. If the zero-time signal is strong at a particular phase shift than it is interpreted to mean that there is a target at that location since the zero-time signal corresponds to zero range. An advantage of f-k migration over time-domain processing is that this phase shift is applied to all the elements in the synthetic aperture (x domain) at the same time; greatly reducing computational time. After performing a phase shift, all the frequency elements (columns) are summed to obtain the zero-time response for that depth; this is repeated for each depth, generating a time-wavenumber matrix. Since the final response needs to be in the time-space domain, an IFFT is taken in the x dimension. Another advantage of f-k migration is that is lends easily to incorporating depth dependent velocities of propagation seen in layered media such as firn. For each iteration, the necessary phase shift via k_z can be calculated by using the corresponding velocity of propagation for that depth.

The derivation of the f-k algorithm above only considers the travel time between the target of interest and the receiver, but we must also consider the travel time between the radar

transmitter and the target. Since the transmitter and receiver are collocated and both move the same along-track distance between records; this is effectively a doubling of the radar movement. We can account for this by cutting the velocity of propagation in half:

$$k_z(\omega, k_x) = \sqrt{\left(\frac{2\omega}{v}\right)^2 - k_x^2}$$

The f-k migration theory assumes that the collected signals are infinite in time (depth) and space (along-track); they have a finite bandwidth in the f-k domain. Since the recorded signals must be time limited in the fast-time (depth) domain and time limited in the slow-time (along-track) domain, there will be portions of the unfiltered f-k data matrix that correspond to non-physical signals or evanescent waveforms. Filtering will be used to overcome this issue. The frequency (depth) domain will be filtered to the radar bandwidth. The wavenumber (along-track, k_x) domain is filtered based on how much energy in the along-track dimension we want to migrate into the response of a particular target. The physical representation of this k-domain filter is the selection of a synthetic aperture length. For this study, the synthetic aperture length L_{SAR} can be approximated by:

$$L_{SAR} = \frac{\lambda R_{max}}{2\sigma_x}$$

where λ = 0.4 is the wavelength at the center frequency (750 MHz), σ_x = 1 m is the desired along-track resampling, and $R_{max} = 500/\sqrt{3.15}$ m is the maximum expected target range in air assuming a maximum range in ice of 500 m and the radar platform is located at the ice surface. The small distance the radar platform sits above the ice surface (~1 m) and the firn correction are assumed to be negligible.

Figure 56 provides a visual representation of the relationship between the wavenumber and the angle of the incident wavefront from a target displaced in the along-track dimension. The angle of arrival is:

$$\theta = \sin^{-1}\frac{k_x}{\boldsymbol{k}}$$

The maximum accepted angle of arrival, θ_{max}, is typically defined by the beamwidth of the receive antenna in the along-track dimension. θ_{max} is a function of frequency since the antenna beamwidth is also a function of frequency. If the antenna beamwidth is unknown, it can be estimated from the data by observing the tail ends of range hyperbolas. The restricted beamwidth provides a k-domain limit that is used to define the needed k-domain filter, with the maximum k value:

$$k_{max} = \boldsymbol{k}\sin\theta_{max}(\omega) = \frac{2\omega}{v}\sin\theta_{max}(\omega)$$

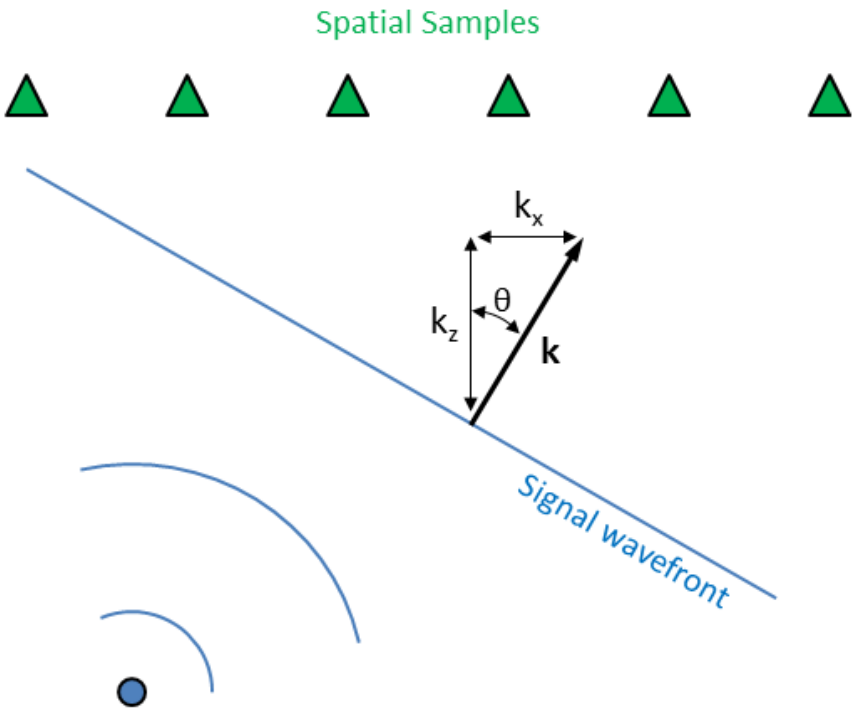

Figure 56. Relationship between wavenumber and angle of arrival.

5.3 Cross-track angle of arrival estimation

In the same spirit as the previous section, for a radar system whose nadir-pointing antenna has a beamwidth in the cross-track direction greater than zero, there exists ambiguity in the azimuth angle of the received energy from the target. While a synthetic antenna array is formed in the along-track direction as discussed above, a physical antenna array has been used in the cross-track direction. This problem can be view as a direction-of-arrival estimation problem and Figure 57 shows an illustration of the problem geometry. While a number of direction-of-arrival estimation algorithms exist, the MUSIC algorithm holds a level of superiority over both Fourier domain [Odendaal and other, 1994; Compton, 1987] and other parametric techniques [Proakis and Manolakis, 1996; Shendkar and others, 2013], under specific

conditions. The MUSIC algorithm will be applied in this study and these conditions will be discussed.

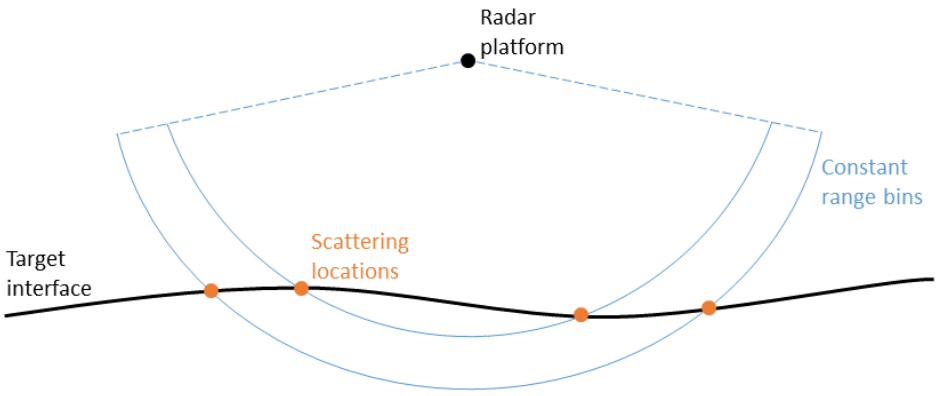

Figure 57. Illustration of the direction-of-arrival problem. A SAR-processed range bin includes only two scattering sources, assuming no layover or shadowing.

There are some data structure and radar parameters that must be considered, including the number of the phase centers, the number of scattering sources (mentioned above), and the SNR of the scatterers of interest. MUSIC algorithm simulations performed by Shendkar and others [2013] show that target angle of arrival estimate errors were less than 1° when using at least 7 phase centers when the scatter's pre-processing SNR is at least -13 dB. The original simulation threshold was 10 dB with 200 coherent integrations; this would translate to a threshold of 8 dB with 128 coherent integrations as used in this research. With a larger number of phase centers, a lower SNR threshold can be tolerated. Simulations suggest that an SNR as low at -12 dB (with 128 coherent integrations) can be tolerated when using 16 phase centers. For any given number of phase centers or post-processing gain, the algorithm is quite sensitive to the lower SNR limit, and accuracy degrades quickly below that limit. For the ground-based radar system used for this study, a 16 phase center antenna array is used with 128 along-track

coherent averages. Example SAR-processed radar data from the Pirrit Hills, Antarctica survey location is shown in Figure 58. Here the nearly specular surface return has been scaled and shifted to align with the peak basal interface return. Significant off-nadir (cross-track) backscatter energy can be seen at the basal interface.

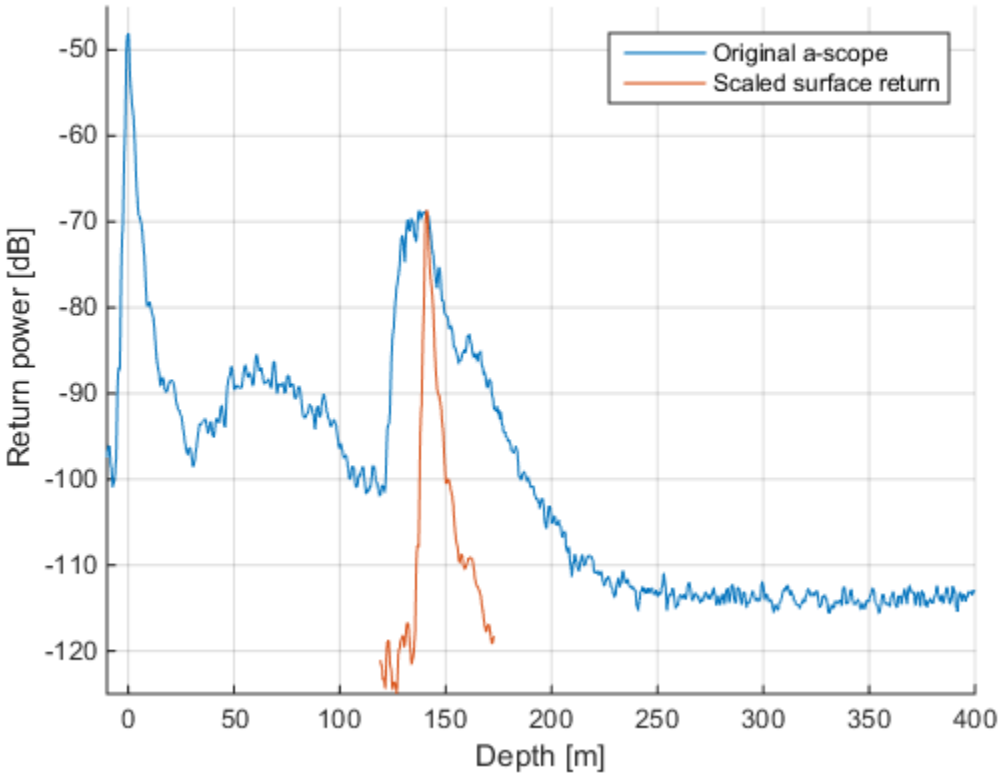

Figure 58. Example bed interface off-nadir backscatter energy from Pirrit Hills survey location.

The MUSIC algorithm is a noise subspace spectral estimator and works best when the number of signal sources is small compared to the number of measurements. The algorithm projects the noise subspace of the received signals into an angular domain using a steering vector defined by the antenna array spacing, steering nulls through the power spectral density (PSD). The reciprocal of this mapped PSD is a sharply peaked function of angle and the angle of

arrival of strong scatterers can be found by picking these peaks [Schmidt, 1986; Proakis and Manolakis, 1996]. The collected data can be modeled as [Schmidt, 1986]:

$$X = AF + W$$

where X is a column vector representing the collected data at a given along-track index and a given range index with M elements equal to the number of receive channels in the cross-track dimension. A is a steering matrix with M rows representing the relative position of the receiver and D columns representing all the possible incident signal directions. F is a column vector of length D representing all the possible incident signals. W is a column vector of length M representing the addition of environment and instrument-based noise. It is assumed that the noise signals W_i are uncorrelated with each other and uncorrelated with the incident signal space F_i. From here, the interest is to use statistical methods to highlight the similarities between the received signals. By taking advantage of the geometry of the receiving system, the statistical alignment of signals can be translated into a direction of arrival. The algorithm steps are:

1. Form the covariance matrix, $S = \overline{XX^*}$, of the received signal space.
2. Calculate the eigenvectors and eigenvalues of the covariance matrix. The eigenvectors "highlight" the correlated portions of the covariance matrix while the eigenvalues provide a numerical measure of this correlation.
3. Organize the eigenvectors by their eigenvalues from largest to smallest. The eigenvectors have the largest eigenvalues are considered part of the signal space and the eigenvectors with the smallest eigenvalues are considered part of the noise space.

4. Decide on the number of signals of interest, D. In this study we are interested in two signals: one from the left of the radar center axis, and one from the right. This is based on the assumption that our target of interest is the plane defining the base of the ice, that this plane has no layover or shadowing and is relatively rough enough to generate off-nadir backscatter, and that the plane is the strongest scatterer in the signal space (due to the large dielectric contrast between firn/ice and bedrock, or firn/ice and ocean) and selected range zone. The remaining signals, $N = M - D$, are considered part of the noise space, E_N. The algorithm works best when $D \ll M$ [Schmidt, 1986; Paden and others, 2010]. Each receive channel is separately SAR-focused so that for any given pre-MUSIC pixel, the energy should only be arriving from two directions: left or right, as seen in Figure 57.
5. Generate the MUSIC pseudo-spectrum. This pseudo-spectrum maps the noise space into the angular domain using the steering matrix, A, steering nulls through the noise space. The reciprocal creates a sharply peaked function of angle, θ [Schmidt, 1986]:

$$P_{MUSIC}(\theta) = \frac{1}{\left|a_{ij}(\theta)E_N\right|^2}$$

where E_N is an M x N matrix of the N noise eigenvectors each with length M and $a_{ij}(\theta)$ is the M x 1 steering matrix [Shendkar, 2013]:

$$a_{ij}(\theta) = exp\left(-(i-1)\frac{\omega d \sin\theta}{v}\right)$$

where $i = 1, 2, \ldots M$, $j = 1$, v is the velocity of propagation in the medium, and d is the spacing between antenna elements.

The MUSIC algorithm output falls within a normalized spatial frequency domain, F, spanning -0.5 to 0.5, that is converted to the actual angular domain, θ. Spatial frequency is related to spatial wavenumber by:

$$k_y = F\frac{2\pi}{\Delta y}$$

where Δy = 30 cm is the antenna separation in the cross-track array. In the same spirit as the f-k algorithm described above, spatial wavenumber can be converted to angle of incident via:

$$\theta = \sin^{-1}\frac{k_y}{k}$$

where $k = 2\pi/\lambda$, and λ = 28 cm is the wavelength at the snow/air interface. At Δy = 30 cm, the antenna array is undersampled and the absolute boundaries of the pseudospectrum span ±27.4°. For this study, a total of 64 equally spaced spatial frequency bins are used. The number of frequency bins is user defined and sets the cross-track resolution. Using the permittivity-derived propagation model described in step 8 below, the spatial frequency spacing corresponds to a nadir cross-track resolution of roughly 3-3.25 m at a depth of 300 m, and 6.2-6.5 m at a depth of 600 m.

6. Repeat the above process for each range index, the resulting rows can be stacked to create a cross-track angle versus range matrix. Figure 59 shows an example of this pseudospectrum. As expected, the algorithm loses some fidelity near nadir, likely due to layover caused by interface roughness. However, two distinct lines form to the left and right as the range shell extends outward at higher angles. For any particular scattering source of interest, such as an ice-bedrock interface, an acceptable selection zone can be

defined around the expected interface return and the maximum within that range zone can be selected. From here, the maximum signal can be selected for each column (angle of arrival) to form a surface that is defined by range and angle of arrival.

7. Repeat the above process for each along-track index.
8. Translate the resulting angle of arrival to a meaningful position in the Cartesian coordinate system. When using Fourier techniques, such as f-k migration, this is done automatically since the calculation of each phase shift accounts for the change in the velocity of propagation in the medium; this is not automatically handled in the MUSIC algorithm processing and the change in the velocity of propagation through the surface interface and the firn must be account for by other means. This is achieved by generating a lookup table constructed using a forward modeling approach that applies Snell's law at each boundary of a discrete velocity of propagation model. The lookup table is constructed so that a depth and cross-track position can be found when the range/time and direction of arrival are known. This local x-y-z coordinated system (along-track, cross-track, depth) is further converted into latitude, longitude, and elevation above the ellipsoid using the recorded GPS and derived heading information.

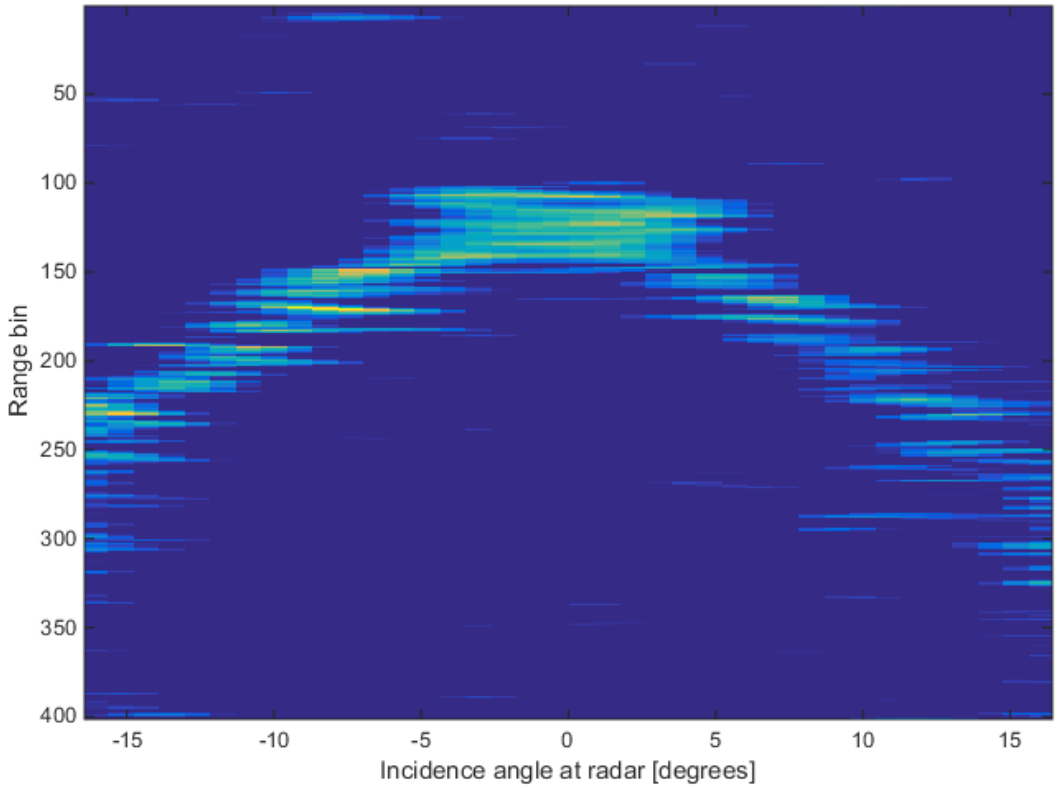

Figure 59. Example of MUSIC pseudospectrum.

5.4 Application to field data

For this study, the discussed technique has been applied to two data sets. Both data sets were collected using the ground-based radar system. The first set was collected in the region of the Pirrit Hills in central West Antarctica. Located at 81°17'S, 85°21'W, the Pirrit Hill is an isolated group of nunataks located south of the Ellsworth Mountains and roughly 530 km to the east of the West Antarctica Ice Sheet (WAIS) Divide camp in central West Antarctica. The focus of the study was to map the depth, extent, and orientation of a ridge extending under the ice from an exposed nunatak. A grid was collected on 01/21/2013 with 11 lines perpendicular to the suspected ridge with 1 line along the suspected ridge peak. Each of the cross-ridge lines are separated by ~50 m and the total extent of the grid is 580 m by 1 km. A second data set was

collected on the Kamb Ice Stream near the Siple Coast, West Antarctica. Located at 82°56'S, 152°48'W, the Kamb Ice Stream, also known as Ice Stream C, is located south of the Siple Dome camp on the Siple Coast and is a major contributor to RIS. A square-shaped track, 2 km on a side, was collected on 01/03/2014, roughly 35 km from the edge of RIS.

Each of the cross-ridge tracks and the along-ridge track were SAR-processed, MUSIC-processed, geocoded, and gridded separately to allow for self-consistency verification. Permittivity profile data from the WAIS core were used to generate the propagation model for both the SAR and MUSIC processing. It is assumed that the firn properties and accumulation history observed at WAIS Divide are similar to the conditions observed ~530 km to the east at the Pirrit Hills survey location. Measured and modeled data of the Thwaites and Pine Island glacier catchments presented by Medley and others [2014] suggest that ice conditions are likely similar at WAIS core and the Pirrit Hills survey location. Permittivity profile data from Siple Dome were used to generate the propagation model for Kamb Ice Stream track.

After MUSIC processing and maximum value selection, two stages of filtering are applied to the data. First, a manual filtering method is used to identify and remove obvious point errors. These errors are often single pixels or small groups of a few pixels where the elevation differs by 50 m or more from the surrounding values. The values of these removed pixels are replaced with a linear interpolated value from the surrounding pixels. Following this manual filtering stage, a 5 bin along-track by 3 bin cross-track median filter is applied to the data to further reduce errors and has an averaging affect. Significant backscatter energy was observed in the pseudospectra up to ±16° and higher angles of arrival were trimmed from the data matrices.

This sets the swath width at approximately 31.4 m at a depth of 100 m in ice, and grows to approximately 189 m at a depth of 600 m in ice.

After filtering, the data are geocoded. Up to this point the data have been defined based on the location of the radar phase center within the Earth-Centered, Earth-Fixed (ECEF) coordinate system. ECEF is a simple Cartesian coordinate system with its origin (0,0,0) at the center of the earth, the z-axis passing through the north pole, the x-axis passing through the equator and prime meridian, and the y-axis passing through the equator and 90°E to complete the right hand system. At any particular along-track position, the interface of interest is defined by the range of that interface at each of the angles of arrival produced by the MUSIC algorithm. This family of arrival angles lies within a plane perpendicular to the along-track heading. It is assumed that this plane always passed through the ECEF origin (i.e. the antenna array's direction of maximum directivity is always pointed normal to the geoid). Knowing the radar phase center location and the heading of the platform (derived from GPS), the angles of arrival and ranges of the signals of interest can be converted to points within the ECEF coordinate system using the generated lookup table described in Section 5.4. Standard conversion equations are then used to convert the ECEF data to latitude, longitude, and elevation of the imaged surface above the geoid.

5.5 Results and discussion

After geocoding, the resulting array of points is equally spaced in the local along- and cross-track dimensions, but has a scattered nature overall due to heading changes along the often not-perfectly-straight ground tracks. To allow for direct comparison between imaged elevations of neighboring tracks, master grids were defined for each location and data from

each track segment is interpolated to those grids. These master grids set the final image resolution or posting. A resolution of 0.0001° was chosen in both latitude and longitude. This translates into a latitude resolution (posting) of approximately 11.1 m and a longitude resolution (posting) of approximately 1.7 m. Composite mosaics were created for each location. A 7x7 median filter was applied to the each mosaic to further reduce point errors and create a smoother appearance.

Figure 60 and Figure 61 show isotropic and top views, respectively, of the composite mosaic for the data collected near an exposed nunatak in the Pirrit Hills region, West Antarctica. The exposed nunatak is positioned just off the top left corner of Figure 61. The along-ridge track, running roughly top to bottom in Figure 61, was chosen based on the best guess of the under-ice ridge position. It appears that the actual ridge axis is oriented ~35° off the data track. Elevations within the collected data range from 750 m to 1200 m above the geoid. The ice surface is ~1300 m above the geoid.

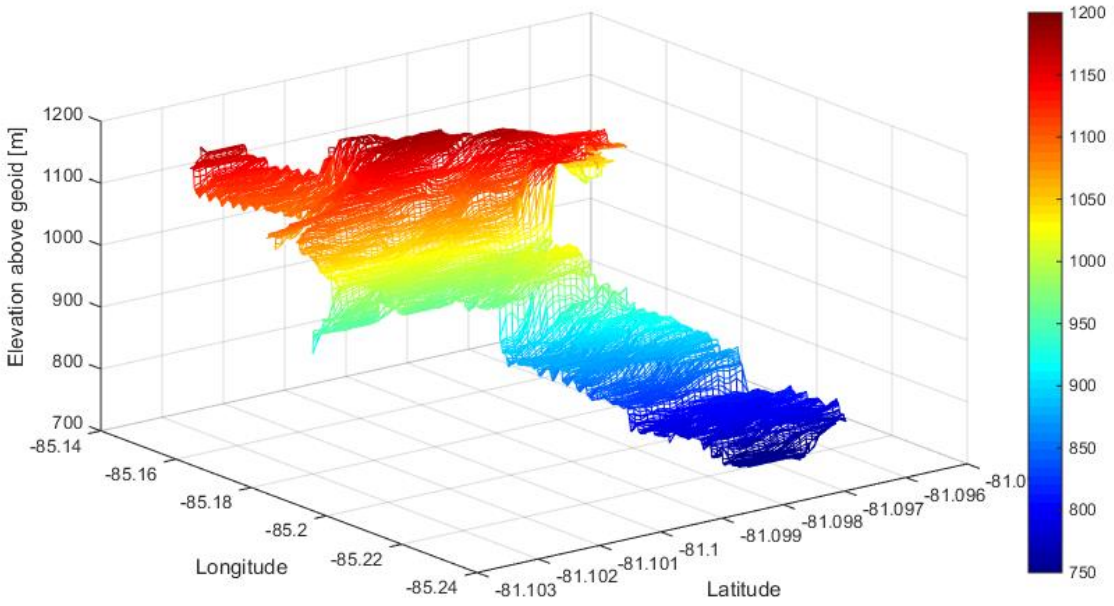

Figure 60. Isotropic view of topography mosaic created from data collected near the Pirrit Hills, West Antarctica.

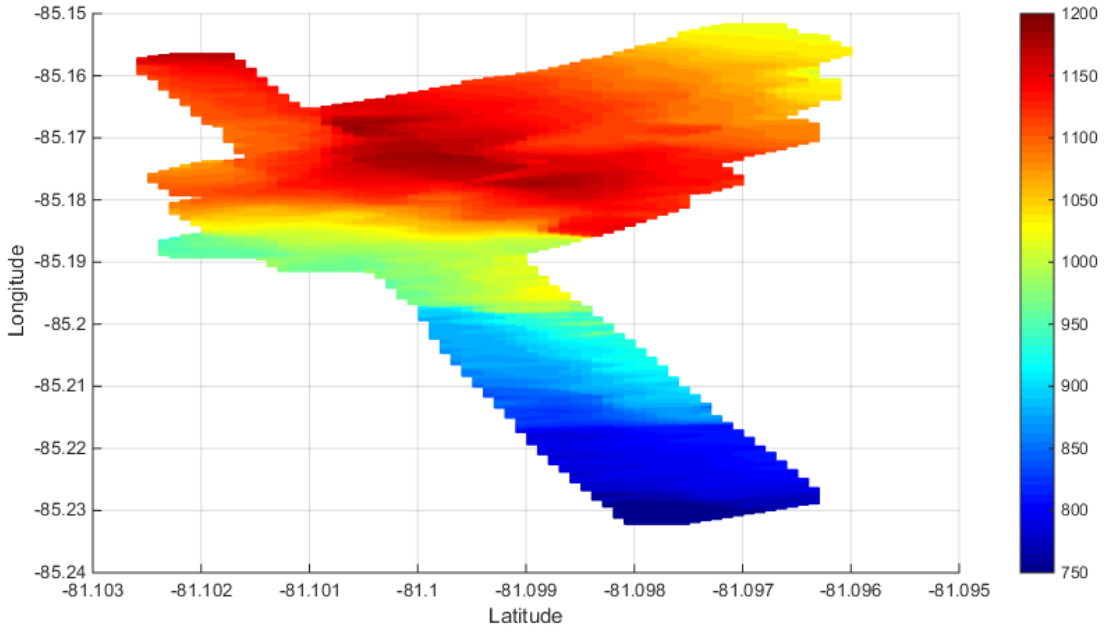

Figure 61. Top view of Pirrit Hills topography mosaic.

Figure 62 and Figure 63 show isotropic and top views, respectively, of the composite mosaic for the data collected on the Kamb Ice Stream, West Antarctica. Red arrows annotations show

the dominate flow direction on the ice stream. There appear to be persistent “grooves” in the ice/bedrock interface parallel to the direction of flow. These grooves are easily seen in the tracks running parallel to the flow. Undulations seen in the cross-flow tracks may also suggest the presence of grooves running parallel to the stream flow. The bedrock in this location is below the geoid, ranging between 490 and 540 m below the geoid. The ice surface elevation is ~150 m above the geoid. The survey path begins in the top left corner of Figure 63 and proceeds counterclockwise as indicated by the black arrows. This path places the right side of the radar sled always on the outside of the square track. During field operation, there was a failure in the operation of the transmit-antenna selection switch preventing ping-pong operation. As a result, target interfaces were only illuminated from the right side of the antenna array. The results seen in Figure 63 appear to indicate a bias to the right side of the array. This is most apparent where there are steep elevation changes in the cross-track dimension where illumination from only the right side of the imaged swath leads to a shadowing effect. This effect is characterized by a very sharp contrast in neighboring elevation values with the shallower interface elevations on the right side of the track.

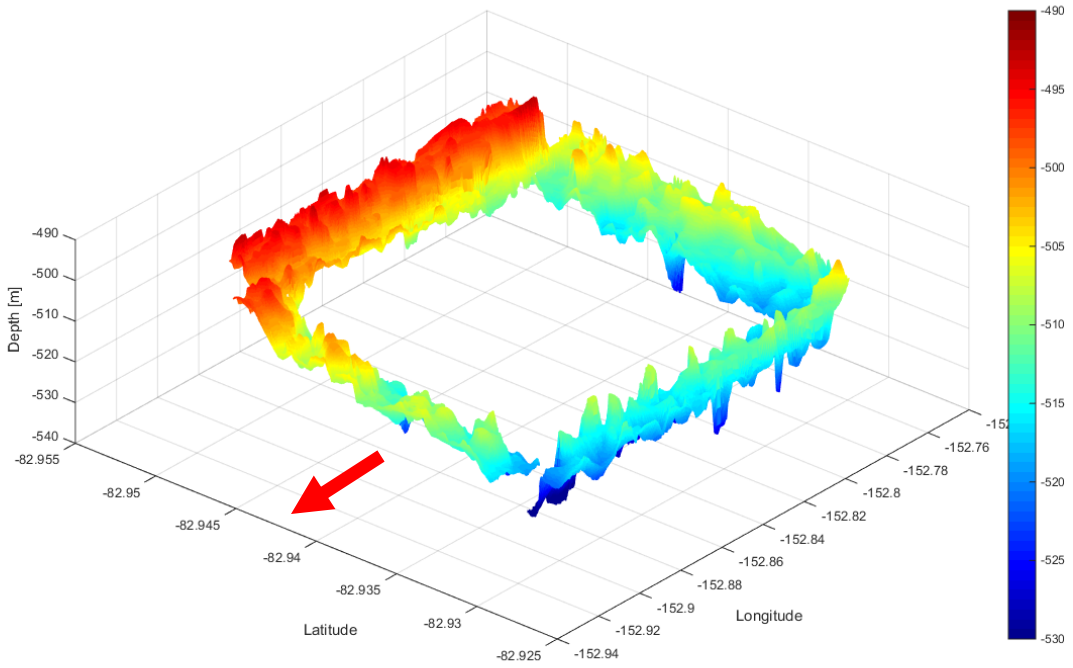

Figure 62. Isotropic view of topography mosaic from data collected on the Kamb Ice Stream, West Antarctica. Red arrow indicates ice stream flow.

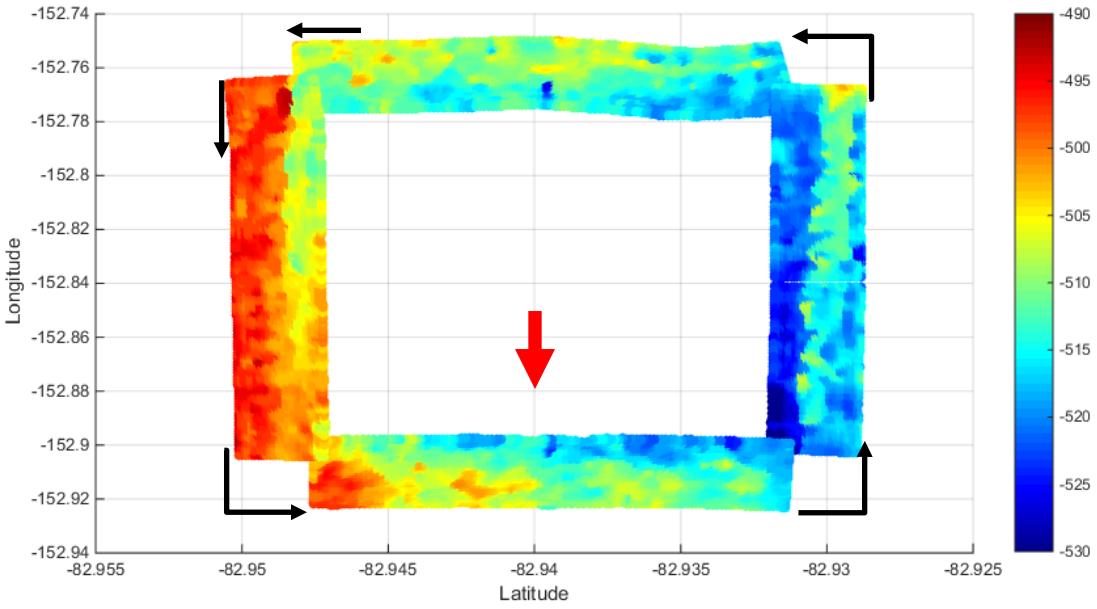

Figure 63. Top view of Kamb Ice Stream mosaic. Red arrow indicates ice stream flow. Black arrows indicate the survey path, beginning in the top left corner.

Differences in elevation in overlapping portions were calculated to provide insight into the validity of the 3D processing algorithm. Figure 64 shows the elevation estimate error for the overlapping portions of the cross-ridge tracks for the Pirrit Hills data set. The uneven nature of the overlap is a result of the non-straight-line and unevenly spaced tracks. Error values range from 0 to 70 m. The inset histogram shows the error distribution. Only ~5% of the overlapping region has an error on the order of the radar range resolution (43 cm in ice), with ~25% of the overlapping region having an error within an order of magnitude of the range resolution. Figure 65 shows the elevation estimate error for the portions of the dataset where the cross-ridge tracks overlap the along-ridge track. The cross-ridge tracks (orange) and the along-ridge track (blue) have been overlaid for clarity. Again, errors range from 0 to 70 m, and the inset histogram shows the error distribution. Only ~2% of the overlapping region has an error on the order of the radar range resolution, with ~10% of the region having an error with on order of magnitude of the range resolution.

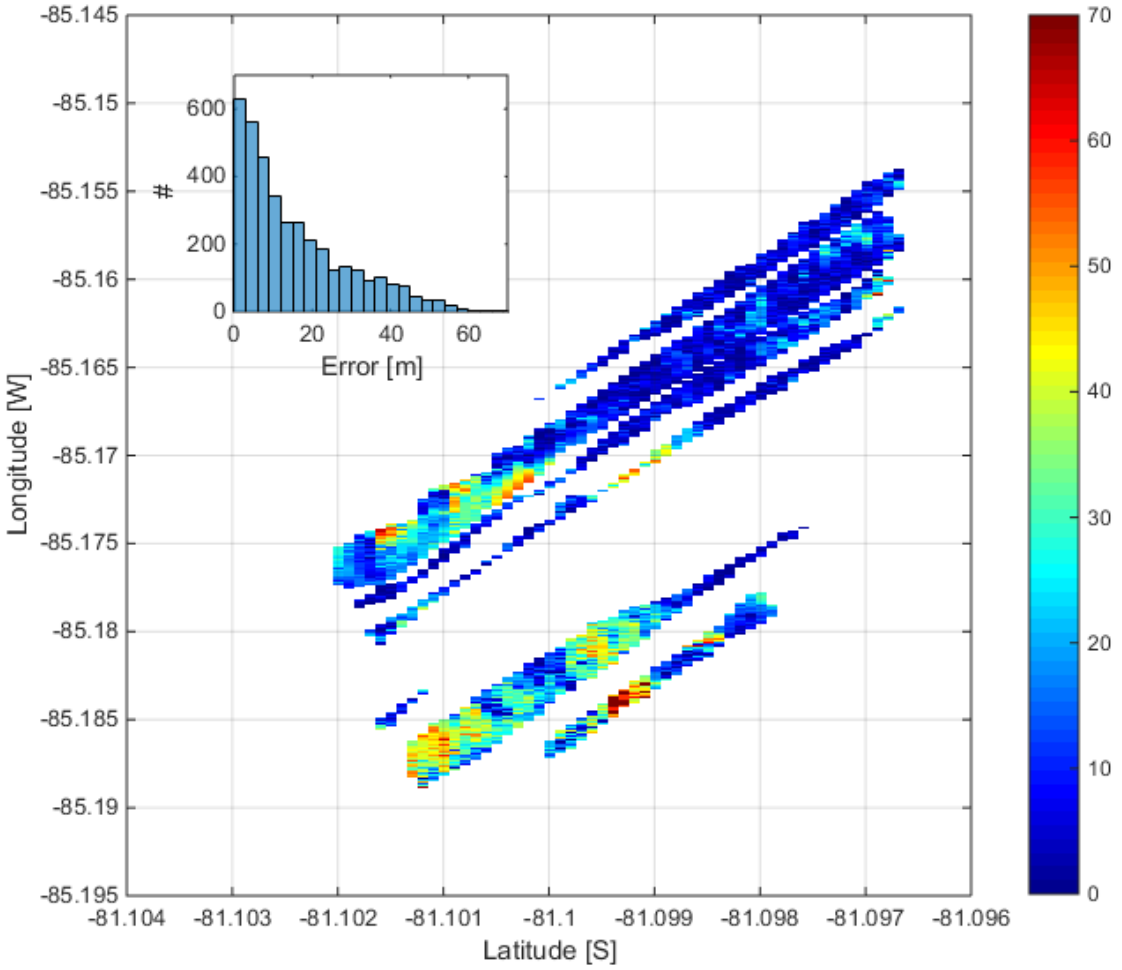

Figure 64. Elevation estimate error for overlapping portions of the cross-ridge tracks for the Pirrit Hills data set. Inset shows histogram of error values.

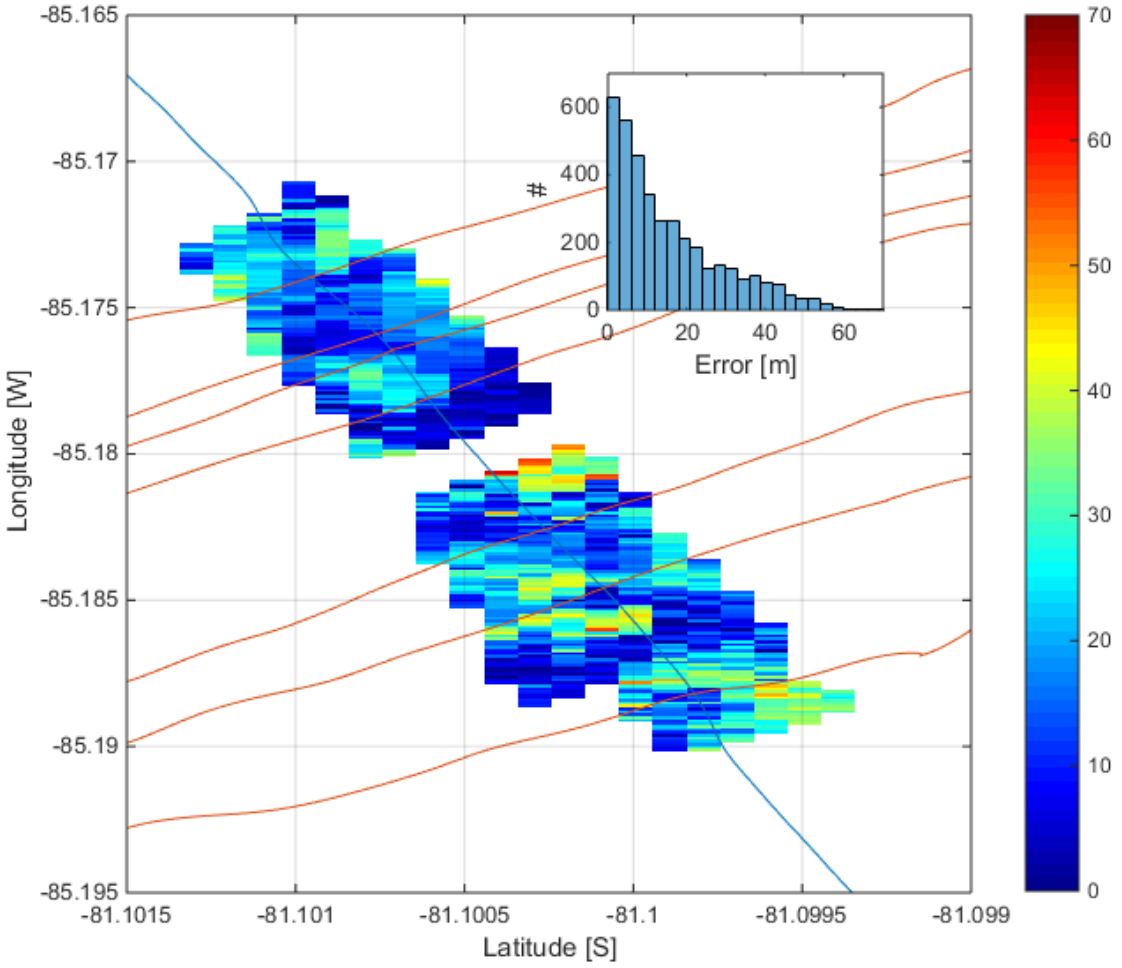

Figure 65. Elevation estimate error where cross-ridge tracks overlap along-ridge track for the Pirrit Hills data set. Inset shows histogram of error values. Track annotations provided to clarity, orange = cross-ridge, blue = along-ridge.

It appears that many of the significant errors are two orders of magnitude more that the range resolution (>43m) are focused near areas where there appear to be large changes (>100 m) in basal elevation over a short distance (<50 m). This suggests that these large errors may be attributed to shadowing.

Similar results appear during error analysis of the Kamb Ice Stream (KIS) track. Figure 66 shows the elevation estimate error for the overlapping corners of the KIS track. For three

corners of the track, there appear to be reasonable elevation agreement, averaging within an order of magnitude of the radar range resolution. However, one corner of the track showed significant error between overlapping portions. A closer investigation of the MUSIC pseudospectra in this portion of the track show that after the turn (the vertical track on the right side of Figure 63), there were no dominant returns at higher incident angles to the left of the radar within the predetermined range selection zone. In this particular location, the maximum selecting routine selected relatively weak returns at the higher incident angles that were at a deeper range bin, likely erroneously. This situation suggests that a return power threshold in the maximum finding routine may be beneficial, but applying this hypothesis to other locations, especially errors in the Pirrit Hills grid, was inconclusive.

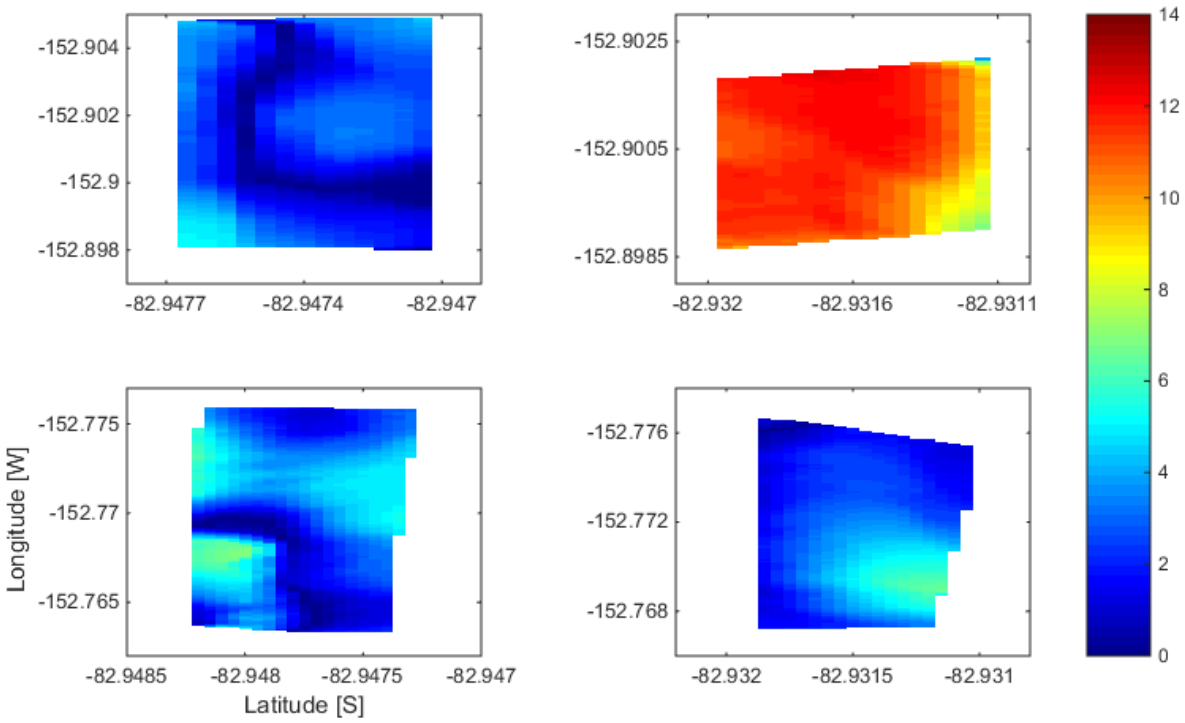

Figure 66. Elevation error for overlapping sections at corners of the Kamb Ice Stream square track.

In the large scale, the 3D algorithm appears to be able to image interface topography with rather coarse resolution. Some features are clearly distinguishable. There is a ridge that exists within the data grid collected in the Pirrit Hills region and we can ascertain its shape and orientation. The data from KIS appear to show grooves carved in the bedrock that are parallel with the ice stream flow; this is a feature that we would expect to see. On the small scale (on the order of the radar resolution) features are present in the data, but the error analysis shows that if these features are viewed from different orientations, the nature of their backscatter changes. This is to be expected of a distributed target. As stated earlier, the MUSIC algorithm performs best when the number of observations is much larger than the number of expected targets. The assumption is that these targets are distinct from their surroundings and from each other, exhibiting the nature of point targets, such as formations that form natural dihedrals/trihedrals. Such targets create distinct, narrow peaks in the calculated pseudospectra. By contrast, the targets of interest within these data are distributed (or extended) targets. Any defined bin (along-track position, range shell, cross-track angle) is made up of a family of scattering centers whose backscatter response can be described by:

$$V = \sum_i v_i e^{-j\phi_i}$$

The total received signal is the summation of a family of small signals with randomly distributed voltage and phase. These individual signals constructively and destructively interfere with each other to produce the observed signal. This interference is a function of the observation geometry; this is called fading. With traditional SAR techniques, the effects of fading can be reduced by increasing the number of independent samples of the target. Two

approaches exist for obtaining independent samples: change the observation frequency or change the observation geometry. These two techniques manifest in the range and along-track processing. Using a chirped signal provides independent samples via changes in frequency (range dimension), and using a moving platform in the along-track direction provides independent samples via changes in observation geometry (along-track dimension). A cross-track antenna array is intended to provide independent samples in the cross-track dimension; however, the MUSIC algorithm does not treat these observations in this manner and therefore cannot reduce fading in the cross-track dimension. MUSIC (and other parametric and subspace signal processing techniques) is not effective at providing reliable, fine-resolution imaging of distributed targets whose fading characteristics are a strong function of the observation geometry. The ice/bedrock interface is such as target. Traditional Fourier techniques can be applied in the cross-track dimension. To obtain fine angular resolution in the cross-track requires a large number of antenna elements, often a difficult physical limitation.

Chapter 6: Conclusions and recommendations for future work

Ice shelves are sensitive indicators of climate change and play a critical role in the stability of ice sheets and oceanic currents. Many aspects of shelf stability can readily be observed including surface changes, velocity, and loss through calving; however, mass loss through basal melting has been found to be a significant contributor the shelf mass balance and is not easily observed, even by indirect means. The basal component of mass balance has often been inferred via the assumption of hydrostatic equilibrium. Early, relatively low spatial resolution ice-penetrating radar measurements provided the first look at the ice-shelf basal interface and brought into question the validity of the hydrostatic assumption. This work uses data from an airborne UWB UHF radar, which was improved as a part of this work, to provide fine-resolution detail of the ice-shelf basal interface. Repeat flights and internal layer mapping allowed basal melt rates to be tracked. Ultimately, wide-swath interface imaging is desired, and to this end, the efficacy of a 3D imaging algorithm was evaluated. Specifically, a technique for estimating ice-shelf basal melt rates using airborne radar data while separating the effects of ice motion and surface accumulation was demonstrated, and 3D images of bed topography were constructed from radar data using parametric processing techniques. The efficacy of the processing algorithm using overlapping data lines was evaluated. A summary of the work performed, conclusions drawn, and recommendations for future work will be presented in this chapter.

6.1 Summary and Conclusions

A well-rounded discussion of the UWB UHF radar development and performance was presented in Chapter 2. While the radar system was originally conceived based on the

necessity of measuring near-surface layering, it was found that the radar was capable of addressing a wider range of glaciological issues. The existence of englacial interfacial horizons at 300 MHz bandwidth indicate that changes in conductivity are the main cause of reflections from these interfaces below the firn-ice transition. The ability to image deep englacial horizons, and in some instances even firn horizons, is dependent on ice temperature and surface scattering. Ice attenuation rates are highly temperature dependent. All observed deep reflections were recorded in the north-central, interior regions of the ice sheet where the ice is sufficiently cold. A steady drop in recorded interface reflectivity was often observed along flight lines traveling from the interior of the ice sheet toward the edge. A lack of deep reflections was observed in southern interior Greenland. Scattering mechanisms, such as the rough and heavily crevassed surfaces of glaciers and their catchments, also reduced the ability to image deep interfaces. Interface imaging may also be a function of aircraft pitch and is therefore related to the along-track antenna beamwidth, as layering often disappears during periods of significant pitching maneuvers. For example, during level flight on the Petermann Glacier, the rough surface of the floating ice-shelf still revealed firn layering, but this layering disappeared during the climb up the glacier, which was marked by significant aircraft pitching. The presence of liquid water, either on the surface or at depth, also severely limits or impedes the retrieval of deeper reflections. However, this does provide an opportunity to use the radar and its data for the purpose of detecting liquid water, as presented by Rodriguez-Morales and others [2013] and Forster and others [2013].

Data were primarily collected from ideally stratified regions, making it easy to track interfaces across long horizontal distances. However, most of the East Antarctic Ice Sheet

(EAIS) is covered with unconformable stratigraphy [Arcone and others, 2012a; Arcone and others, 2012b]. Results collected over the Pine Island Glacier catchment were presented, which exhibited significant undulations and layer pinching. This could give insight into the ability of the radar to map the unconformed horizons within the EAIS. Many of the regions of unconformable stratigraphy have surface undulations with wavelengths of 2-5 km and amplitudes of 2-8 m [Arcone and others, 2012a; Arcone and others, 2012b]. With surface slopes considerably shallower than those presented in Figure 24, we would not expect the same visibility degradation. We would expect the radar to perform similarly when imaging the EAIS, resolving interface spacing to 55 cm, even in the presence of unconformities.

Analysis showed that radar data-derived reflectivity profiles can be used to estimate: firn density profiles, the thickness of zones with differing compaction mechanisms, and the depth of the firn-ice transition. The analysis was done over cold, interior regions of the ice sheet where we can easily calibrate our data using a link budget approach with established ice surface densities and attenuation rates. This approach may give insight into the change in density profiles and compaction mechanisms over short horizontal distances, such as along glacial streams and in regions of unconformities, such as the EAIS.

Accurate estimation of ice attenuation rates is highly dependent on accurate knowledge of the ice and interface properties. The calculation was simplified by finding a single, depth-averaged loss between two known interfaces. There is high confidence in the attenuation rates calculated for floating ice shelves, since both the surface and basal interface had flat regions, providing strong specular reflections. The calculated attenuation rates matched well with other published rates for RIS. Two particular parameters presented a

challenge to attenuation rate calculation: the reflectivity of the surface interface and the roughness of the basal interface. When possible, nearby published surface densities were used to estimate surface reflectivity. Where published surface densities were not available, knowledge of the surface properties were used to estimate the surface reflectivity. Estimations were verified with a link budget analysis. The basal interface reflectivity was shown to be dependent on the interface slope. Finding areas that are sufficiently flat within the radar footprint can prove to be difficult in regions with glacial streams where ice movement roughens the bedrock, or ice shelves where the basal interface is characterized by blocks of ice of varying thickness, as is the case with Petermann Glacier. Using an antenna or antenna array that generates a smaller ground footprint will improve the accuracy of both interface depth and reflectivity estimations, further improving attenuation rate calculations.

Melt rates for the Petermann glacier floating ice-shelf were examined in Chapter 3. Previous studies of the Petermann ice-shelf have relied on surface elevation measurements coupled with the hydrostatic equilibrium assumption or relatively course resolution VHF radar. Here, the application of a UWB UHF radar with relatively fine resolution revealed a complex basal interface and significant deviations from hydrostatic equilibrium. Using the hydrostatic assumption does not accurately capture small-scale crevasses and, by extension, shows that these crevasses are not in hydrostatic balance. In general, the shelf appears to be in hydrostatic balance beyond 20 km from the grounding line. Between 10 and 20 km from the grounding line, the hydrostatic assumption appears to slightly overestimate the thickness of the shelf. Between 2 and 10 km from the grounding line, the hydrostatic assumption appears to greatly underestimate the thickness of the shelf. Results presented earlier show that the

hydrostatic assumption overestimates year-to-year thickness losses within ~8 km of the grounding line. All thicknesses, both radar-tracked and hydrostatic, were calculated assuming no surface snow or firn correction. Regardless of the thickness estimation method, a firn correction would result in a thinner estimate. The results presented have shown significant differences between the radar-tracked and hydrostatic thickness. No constant bias was found along the length of the ice-shelf and a firn correction would need to be applied to both thickness estimation methods; therefore, the differences between the radar-tracked and hydrostatic thickness estimates cannot be reconciled by simply including a firn correction.

Repeat airborne data tracks were collected in 2011, 2013, and 2014. A consistent, bright internal layer was tracked and assumed to be stable over the 3-year observation period from 2011 to 2014. Thickness changes were tracked from year to year and the internal layer was used to separate surface melt from basal melt. Shelf along-track velocity was examined by correlating surface and basal features and was used to remove ice motion from the melt rate estimates. Melt rate estimates were separated into their steady-state (melt as a function of mass advection) and non-steady-state (melt as a function of time) components. The average steady-state melt rates were found to be fairly stable and consistent with observations reported in the literature. Significant variation was observed in the non-steady-state melt rates, with large jumps following major calving events.

The following items appear to be the major results of this analysis:

1. In general, the ice-shelf is in hydrostatic balance seaward of 20 km from the grounding line. Zones within 20 km of the grounding line where radar-tracked and hydrostatic thicknesses do not agree suggest that the shelf has some inertia following its decoupling

from the bedrock and some time is required for it to reach a general hydrostatic equilibrium.

2. The basal interface of the ice-shelf is heavily crevassed, and hydrostatic equilibrium-derived thickness estimates do not fully capture the number and magnitude of the crevasses.
3. Seaward accelerations jumped from ~4m/yr^2 between 2002 and 2013 to 60 m/yr^2 from 2013 to 2014.
4. Steady-state melt rates appear to be relatively constant with time, but non steady-state melt rates appear to jump significantly following a major calving event.

Chapter 4 focused on evaluating the performance of 3D image generation of basal topography using the MUSIC algorithm. Multi-channel data sets were collected using a ground-based version of the UWB UHF radar. Field experiments were conducted in the Pirrit Hills region of West Antarctica in January of 2013 and in the Siple Coast region of West Antarctica in January of 2014. Data collection in the Pirrit Hills region focused on attempting to image the depth, position, and orientation of an under-ice ridge in connection with an exposed nunatak. Data collection in the Siple Coast region included multiple small survey locations located mostly on ice streams; one such location on the Kamb Ice Stream (KIS) was selected for study. Both data sets were selected because they exhibited significant off-nadir backscatter. Grid lines in the Pirrit Hills data set were chosen based on a best-guess estimate of the under-ice ridge orientation with multiple tracks crossing perpendicular to the ridge and one track attempting to follow along the ridge peak. A simple square track was collected on the KIS with two sides of the square oriented parallel to the stream flow.

Results of the topography tracking algorithm showed that there was general success in mapping the large scale features. In the Pirrit Hills data, an under-ice ridge is clearly visible and it was found that its orientation is ~35° off of the estimated orientation. Observed elevations spread from 750 m to 1200 m above the geoid, with surface elevations at ~1300 m. The ridge appears to have a gentle slope on its south side and a steeper slope on its north side. In the KIS data, groove features oriented parallel to the ice stream flow vector were observed. This is an expected feature at the bedrock interface of a moving ice stream as the flow of the ice carves into the bedrock.

Each parallel or perpendicular track of a data set was processed individually and portions where the elevation estimates overlapped were compared to verify the efficacy of the imaging algorithm on the small-scale. It was found that the processing algorithm is unable to consistently reproduce elevation estimates when observing the target interface from different tracks. Rarely were elevation estimates reproducible on the order of the radar range resolution. Significant elevation errors, two orders of magnitude greater than the radar range resolution, were often seen in spots where there appear to be sizable elevation changes over short horizontal distances on the large-scale ("cliffs"), suggesting that these significant errors may be a result of shadowing or layover. Clearly the algorithm is not able to unambiguously resolve small-scale features. The accuracy of the MUSIC algorithm relies heavily on the radio brightness of target of interest (SNR) in relation to its surrounding and neighboring targets. For example: the radar casts a footprint on the target interface. The width of the footprint in the along-track is defined by the SAR processing (1 m) and the width in the cross-track is defined by the antenna's cross-track beamwidth. Assuming the aforementioned ±30° nadir beamwidth,

one air/ice refraction at the surface produces a ±16.4° nadir beamwidth in ice and a footprint width of 294 m at a depth of 500 m. MUSIC divides this footprint into equal cross-track width bins. The number of bins is defined by the user, for this study 64 bins were used, resulting in a theoretical nadir cross-track bin width of 4.6 m. The number of bins could be increased to a point of diminishing returns, hence the term "super-resolution." The MUSIC algorithm then evaluates the received energy coming from these 64 cross-track bins and selects the strongest signals as target locations (angles of arrival). The number of strongest targets to be selected is defined by the user; in the case of this study, the number of targets selected was two: one from the left and one from the right. The interface being imaged in these data is a distributed target. The constructive/destructive interference of the signals arriving from a particular range/along-track/cross-track-angle bin may or may not produce a distinct response from its neighbors, resulting in erroneous peak angle of arrival selection (or no peak selection at all). MUSIC performs best when the target to be imaged is distinct in the same manner as a point target.

6.2 Recommendations for future work

One possible approach to producing single-pass, fine-resolution topographic images of distributed targets, such as the ice/bedrock or ice/water interfaces, appears to be through post-flight array signal processing. This imaging scheme would rely on one broad-beam transmit channel (or two broad-beam transmit channels, in a ping-pong formation, one from the left and one from the right) with a multi-channel receive array. Achieving resolution on the order of the range or the along-track resolution will require a very large cross-track antenna array. Other approaches include real-time cross-track scanning (on transmit, receive, or both)

and multi-beam arrays where grating lobes are purposefully created. These phased-array approaches often involved more complex feed networks involving switches and phase-shifters; however, a Butler matrix or Rotman lens may be employed. Post-processing may become burdensome with these approaches, especially for the multi-beam technique in the presence of sloped interfaces, as near-nadir beams may be corrupted by layover. Here we'll discuss a system similar to the current UHF radar configuration with 1-2 "floodlight" transmit channels, a receive array, and post-flight array signal processing (i.e. digital beamforming).

"Pushbroom"-style imaging could be achieved with a variety of airborne platforms. This is illustrated in Figure 67. The number of cross-track antenna array elements is driven by the platform choice. Tightly-space flight line grids provide substantial swath overlap and can be easily accomplished using available UAV platforms, such as the CReSIS Meridian [Donovan and others, 2008; Hale and others, 2009], NASA SIERRA [Fladeland and others, 2011], and L-3 Viking 400. With 20 cm element spacing ($\lambda/2$ at 750 MHz), the 8 m wing span of the CReSIS Meridian could accommodate 36 elements, and the 6 m wing span of the NASA SIERRA and L-3 Viking 400 could accommodate 28 elements.

Less agile, yet highly-proven aircraft such as the P-3 Orion, Basler BT-67, and de Havilland Twin Otter could also accommodate large antenna arrays. Such platforms would be able to collect multiple data lines along outlet glaciers and fjord-constrained ice shelves, such as Petermann glacier in northwest Greenland.

The previously discussed elliptical dipole and PCB dipole arrays could be scaled up in number to provide a large cross-track array. Scaling one of these arrays up to 36 or more elements, with their $\lambda/2$ element spacing (20 cm at 750 MHz), creates an array with a length in

excess of 7 m. A recently developed wideband 16-element VHF/UHF (150-600 MHz) array with much narrower element spacing has successfully collected data using a Basler BT-67. The array measures 3.6 m in length, 80 cm wide, and has a ground plane spacing of 16 cm. Scaling this array to UHF operation (600-900 MHz or 550-950 MHz) would reduce the array length for 16 elements to 0.98 m; the original array length of 3.6 m could accommodate up to 58 elements. Ground plane spacing could potentially be reduced to as small as 4.4 cm meaning that elements could easily be integrated into custom UAV wings. Subsequent tuning of the elements (and ground place spacing) may be necessary to compensate for the effects of the internal wing structure and skin material.

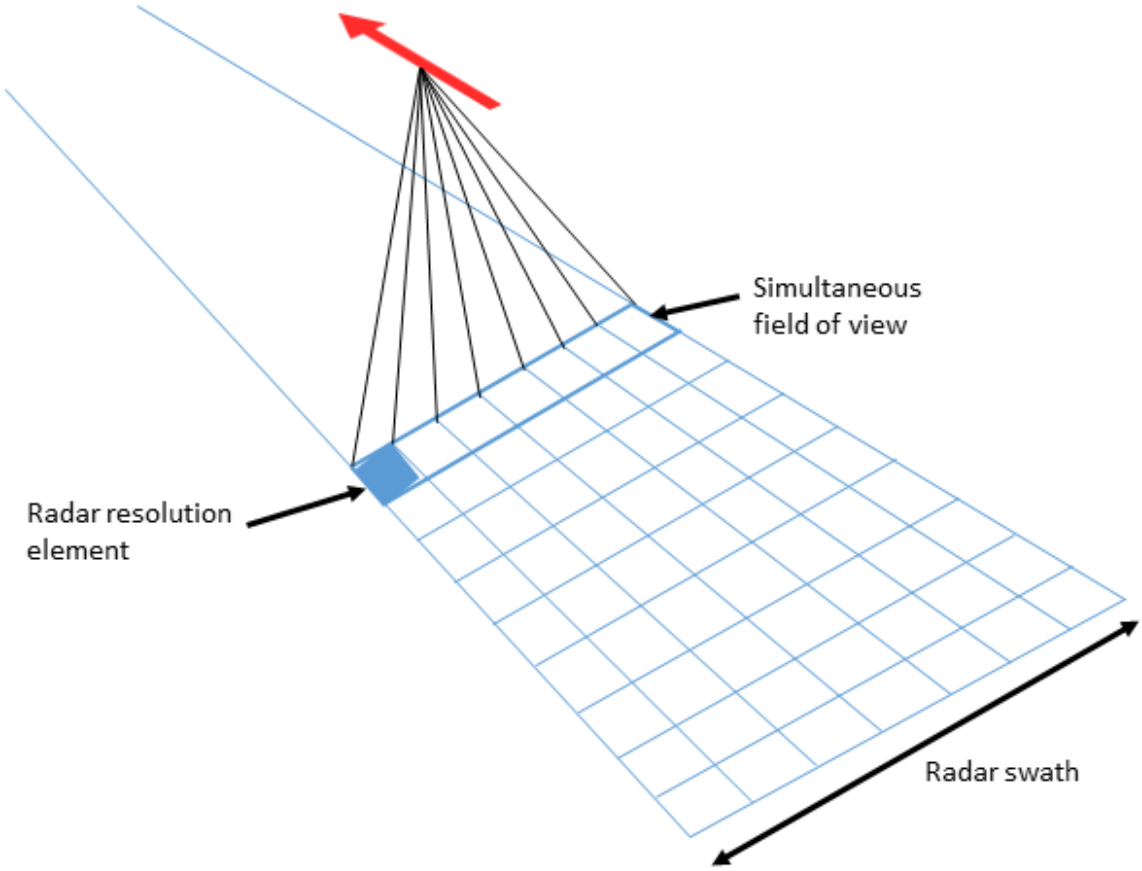

Figure 67. "Pushbroom"-style interface imaging.

Figure 68 shows a diagram of the off-nadir beam geometry for this imaging configuration. The beam-limited footprint criteria is defined by:

$$v\tau > h \tan \theta_{max}$$

where h is the platform height, θ_{max} is the half beamwidth of the antenna, τ is the pulse width, and v is the velocity of propagation in the medium of interest. Using the radar parameters of this study (v = speed of light (c), h = 500 m, τ = 2.048 μs, and θ_{max} = 30°), the radar footprint is beam-limited for the surface interface with a maximum footprint radius of 614.4 m. If a single air/ice refraction is assumed for the surface, Snell's Law reduces θ_{max} = 16.4° and the velocity of

propagation is reduced to $v = c/\sqrt{3.15}$; the maximum beam-limited footprint is reduced to 346.2 m. With h = 500 m, a footprint radius of 288.7 m is formed, leaving an additional 346.2 – 288.7 = 57.5 m of horizontal propagation available within the ice until the footprint is no longer beam limited. This additional propagation is 57.5/tan 16.4° = 195 m in depth. This is quite shallow; we would like to be able to maintain a beam-limited footprint to a depth of ~600 m (the depth of PG at the grounding line). Maintaining a beam-limited footprint to a depth of at least 600 m in ice (under the above operating conditions) would require limiting the maximum steering angle to ±22°.

For a broadside array, the half-power beamwidth (θ_B in Figure 68) of a steered beam (at θ_N in Figure 68) is approximated by:

$$\theta_B = \cos^{-1}\left[\cos\theta_N - 0.443\frac{\lambda}{Nd}\right] - \cos^{-1}\left[\cos\theta_N + 0.443\frac{\lambda}{Nd}\right]$$

where N is the number of elements in the array and d is the element spacing [Balanis, 2005]. If we consider an array of 36 elements, spaced at λ/2, the beamwidth at nadir is θ_B = 2.82° and the beamwidth at a squint angle of 22° is θ_B = 7.64°. At a platform altitude of 500 m, these correspond to surface footprint widths of 24.6 m at nadir and 77.4 m at 22° squint.

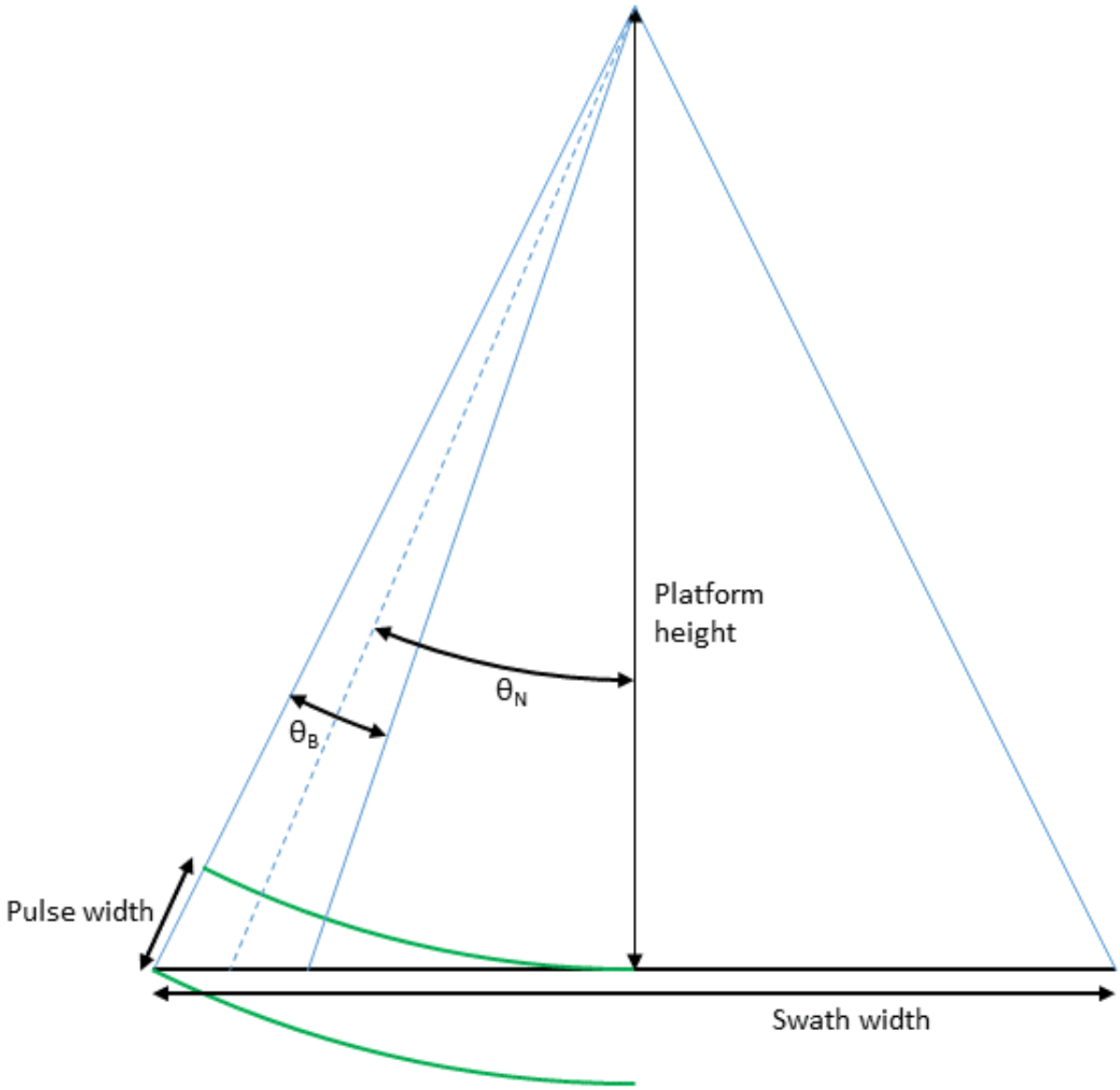

Figure 68. Off-nadir beam geometry.

One potential method for processing the imaged scene is through interferometry. Two data lines will need to be collected separated by a known baseline; this is easily accomplished with modern GPS tracking, as the baseline at each point is always known with a high degree of precision. Persistent scatters in the scene can be used to co-register the resulting two SAR images. For example, when imaging an ice shelf such as Petermann, crevasses may be used to

co-register the two scenes. From here, phase differences between the two scenes can be calculated, forming an interferogram from which the interface height can be calculated. Separate interferograms can be formed for the ice-shelf surface, an internal layer, and the basal interface to generate topographic maps of each interface. Finally, time separated measurements and glaciological mass balance calculations can be employed to determine melt rates, as was done in Chapter 3.

References

Allen C (2008) A brief history of radio echo sounding of ice. *Earthzine* (http://www.earthzine.org/2008/09/26/a-brief-history-of-radio-echo-sounding-of-ice)

Balanis CA (2005) Antenna Theory, *Wiley-Interscience*, **3**

Bamber JL and Bentley CR (1994) A comparison of satellite-altimetry and ice-thickness measurements of the Ross Ice Shelf, Antarctica. *Annals of Glaciology*, **20**, 357-364

Bamber JL, Gomez-Dans JL, and Griggs JA (2009) A new 1 km digital elevation model of the Antarctic derived from combined satellite radar and laser data – Part 1: data and methods. *Cryosphere*, **3**(1), 101-111

Bindschadler R, Vaughan DG, and Vornberger P (2011) Variability of basal melt beneath the Pine Island Glacier ice shelf, West Antarctica. *Journal of Glaciology*, **57**(204), 581-595 (doi: 10.3189/002214311797409802)

Church JA, Clark PU, Cazenave A, Gregory JM, Jevrejeva S, Levermann A, Merrifield MA, Milne GA, Nerem RS, Nunn PD, Payne AJ, Pfeffer WT, Stammer D, and Unnikrishnan AS (2013) Sea Level Change. *Climate Change 2013: The Physical Basis. Contribution of Working Group I to the Fifth Assessment Report of the Intergovernmental Panel on Climate Change*

Compton RT (1987) Two-dimensional imaging of radar targets with the MUSIC algorithm. *The Ohio State University ElectroScience Lab Technical Report 719267-14*

Corr HFJ, Jenkins A, Nicholls KW, and Doake CSM (2001) Precise measurements of changes in ice-shelf thickness by phase-sensitive radar to determine basal melt rates. *Geophysical Research Letters*, **29**(8). (doi: 10.1029/2001GL014618)

Doake CSM (2001) Ice-Shelf Stability. *British Antarctic Survey*, 1282-1290 (doi: 10.1006/rwos.2001.0005)

Doerry AW (2007) Anatomy of a SAR Impulse Response. *Sandia Report SAND2007-5042*

Dominguez R (2012, updated 2014) IceBridge DMS L1B Geolocated and Orthorectified Images. *NASA DAAC at the National Snow and Ice Data Center (NSIDC)*. (http://nsidc.org/data/iodms1b.html)

Donovan WR, Hale RD, and Liu W (2008) The Design and Structural Analysis of the Meridian Unmanned Aircraft. *49th AIAA/ASME/ASCE/AHS/ASC Structures, Structural Dynamics, and Materials Conference*, AIAA-2008-2261 (doi: 10.2514/6.2008-2261)

Dupont TK and Alley RB (2005) Assessment of the importance of ice-shelf buttressing to ice-flow, *Geophysical Research Letters*, **32**, L04503 (doi: 10.1029/2004GL022024)

ESA (2007) EVISAT RA2/MWR Product Handbook. *European Space Agency*

Fladeland M, Sumich M, Lobitz B, Koyler R, Herlth D, Berthold R, McKinnon D, Monforton L, Brass J, and Bland G (2011) The NASA SIERRA science demonstrations programme and the role of small-medium unmanned aircraft for earth science investigations. *Geocarto International, Special Issue: Unmanned Airborne Systems (UAS) for Remote Sensing Applications*, **26**(2), 157-163 (doi: 10.1080/10106049.2010.537375)

Gomez-Garcia D (2014) Sidelobe improvement through predistortion. *Internal CReSIS Report*

Goodman RH (1975) Radio Echo Sounding on Temperate Glaciers. *Journal of Glaciology*, **14**(70), 57-69

Goodman R, Tummala S, and Carrara W (1995) Issues in Ultra-Wideband, Widebeam SAR Image Formation. *IEEE International Radar Conference*, pp. 479-485

Griffiths HD (1991) The effect of phase and amplitude errors in FM radar. *IEE Colloquium on Time-Bandwidth Product Waveforms in Radar and Sonar*, pp. 9-1

Griggs JA and Bamber JL (2009) A new 1 km digital elevation model of Antarctica derived from combined radar and laser data – Part 2: validation and error estimates. *Cryosphere*, **3**(1), 113-123

Griggs JA and Bamber JL (2011) Antarctic ice-shelf thickness from satellite radar altimetry. *Journal of Glaciology*, **57**(203), 485-498

Grosfeld K, Blindow N, and Thyssen F (1994) Bottom Melting on the Filchner-Ronne Ice Shelf, Antarctica, Using Different Measuring Techniques. *Polarforschung*, **67**, 3-17.

Gogineni S, Tammana D, Braaten D, Leuschen C, Akins T, Legarsky J, Kanagaratnam P, Stiles J, Allen C, and Jezek K (2001) Coherent radar ice thickness measurements over the Greenland ice sheet. *Journal of Geophysical Research*, **106**(D24), 33761-33772 (doi: 10.1029/2001JD900183)

Gudmandsen P (1975) Layer echoes in polar ice sheets. *Journal of Glaciology*, **15**(73), 95-101

Hale RD, Donovan WR, and Keshmiri S (2009) UAS Cryospheric Remote Sensing in the Center for Remote Sensing of Ice Sheets. *AUVSI Unmanned Systems North America 2009*.

Harrison CH (1973) Radio echo sounding of horizontal layers in ice. *Journal of Glaciology*, **12**(66), 383-397

Herron MM and Langway CC (1980) Firn Densification: An Empirical Model. *Journal of Glaciology*, **25**(93)

Higgins AK (1991) North Greenland glacier velocities and calf ice production. *Polarforschung*, **60**(1), 1-23

Horgan HJ, Walker RT, Anandakrishnan S, and Alley RB (2011) Surface elevation changes at the front of the Ross Ice Shelf: Implications for basal melting. *Journal of Geophysical Research*, **116**, C02005 (doi: 10.1029/2010JC006192)

Hörhold MW, Kipfstuhl S, Wilhelms F, Freitag, J, and Frenzel A (2011) The densification of layered polar firn. *Journal of Geophysical Research*, **116**, F01001 (doi: 10.1029/2009JF001630)

Jacobs SS, Hellmer H, Doake CSM, Jenkins A, and Frolich R (1992) Melting of ice shelves and the mass balance of Antarctica. *Journal of Glaciology*, **38**(130), 375-387

Jacobs SS, Jenkins A, Giulivi CF, and Dutrieux P (2011) Stronger ocean circulation and increased melting under Pine Island Glacier ice shelf. *Nature: Geoscience Letters*, **4**, 519-523 (doi: 10.1038/NGEO1188)

Johnson HL, Münchow A, Falkner KK, and Melling H (2011) Ocean circulation and properties in Petermann Fjord, Greenland. *Journal of Geophysical Research*, **116**(C1), C01003 (doi: 10.1029/2010JC006519)

Joughin I, Smith BE, and Holland DM (2010) Sensitivity of 21st century sea level to ocean-induced thinning of Pine Island Glacier, Antarctica. *Geophysical Research Letters*, **37**, L20502 (doi: 10.1029/2010GL044819)

Joughin I, Smith B, Howat I, and Scambos T (2011, updated 2014) MEaSUREs Greenland Ice Velocity: Selected Glacier Site Velocity Maps from InSAR, W80.75N. *NASA DAAC at NSIDC* (doi: 10.5067/MEASURES/CRYOSPHERE/nsidc-0481.001)

Kanagaratnam P (2002) Airborne radar for high resolution mapping of internal layers in glacial ice to estimate accumulation rate. Department of Electrical Engineering and Computer Science: Ph.D. Dissertation, University of Kansas

Klauder JR, Price AC, Darlington S, and Albersheim WJ (1960) The theory and design of chirp radars. *Bell System Technical Journal*, **39**(4), 745-808.

Kowatsch M and Stocker HR (1982) Effect of Fresnel ripples on sidelobe suppression in low time-bandwidth product linear FM pulse compression. *IEE Proceedings*, **129**(1), 41-44

Krabill WB, Abdalati W, Frederick EB, Manizade SS, Martin CF, Sonntag JG, Swift RN, Thomas RH, and Yungel JG (2002) Aircraft laser altimetry measurements of elevation changes of the Greenland ice sheet: technique and accuracy assessment. *Journal of Geodynamics*, **34**(3-4), 357-376 (doi: 10.1016/S0264-3707(02)00040-6)

Krabill WB (2014, updated 2015) *IceBridge ATM L2 Icessn Elevation, Slope, and Roughness.* Version 2. Boulder, Colorado USA: NASA DAAC at the National Snow and Ice Data Center (http://nsidc.org/data/ilatm2.html)

Lewis C (2010) Airborne UHF radar for fine resolution mapping of near-surface accumulation layers in Greenland and West Antarctica. Department of Electrical Engineering and Computer Science: Masters Thesis, University of Kansas

Lewis C, Gogineni P, Rodriguez-Morales F, Panzer B, Stumpf T, Paden J, and Leuschen C (2015) Airborne UHF Radar for Mapping Near Surface Internal Layers and Measuring Shallow Ice Thickness. *Journal of Glaciology*, **61**(225), 89-100

Lingle CS, Brenner AC, and Zwally HJ (1990) Satellite altimetry, semivariograms, and seasonal elevation changes in the ablation zone of West Greenland. *Annals of Glaciology*, **14**, 158-163

Medley B, Joughin I, Smith BE, Das SB, Steig EJ, Conway H, Gogineni S, Lewis C, Criscitiello AS, McConnell JR, van den Broeke MR, Lenaerts JTM, Bromwich DH, Nicolas JP, and Leuschen C (2014) Constraining the recent mass balance of Pine Island and Thwaites glaciers, West Antarctica, with airborne observations of snow accumulation. *The Cryosphere*, **8**, 1375-1392 (doi: 10.5194/tc-8-1375-2014)

Miller H and Schwager M (2000) Density of ice core ngt37c95.2 from the North Greenland Traverse. *PANGAEA* (doi: 10.1594/PANGAEA.57798)

Moses RL, Potter LC, and Cetin M (2004) Wide angle SAR imaging. *Proceedings of SPIE*, **5427**, 164-175

Münchow A, Padman L, and Fricker HA (2014) Interannual changes of the floating ice shelf of Petermann Gletscher, North Greenland, from 2000 to 2012. *Journal of Glaciology*, **60**(221) (doi: 10.3189/2014JoG13J135)

Neal CS (1979) The dynamics of the Ross Ice Shelf revealed by radio echo-sounding. *Journal of Glaciology*, **24**(90), 295-307

Nick FM, Luckman A, Vieli A, van der Veen CJ, van As D, van de Wal RSW, Pattyn F, Hubbard AL, and Floricioiu D (2012) The response of Petermann Glacier, Greenland, to large calving events, and its future stability in the context of atmospheric and oceanic warming. *Journal of Glaciology*, **58**(208), 229-239 (doi: 10.3189/2012JoG11J242)

Nick FM, Vieli A, Andersen ML, Joughin I, Payne A, Edwards TL, Pattyn F, and van de Wal RS (2013) Future sea-level rise from Greenland's main outlet glaciers in a warming climate. *Nature*, **497**(7448), 235-238 (doi: 10.1038/nature12068)

Odendaal JW, Barnard E, and Pistorius CWI (1994) Two-Dimensional Superresolution Radar Imaging Using the MUSIC Algorithm. *IEEE Transactions on Antennas and Propagation*, **42**(10), 1386-1391

Orsi AH, Johnson GC, and Bullister LL (1999) Circulation, mixing and production of Antarctic Bottom Water. *Progress in Oceanography*, **44**, 55-109

Paden JD, Allen CT, Gogineni S, Jezek KC, Dahl-Jensen D, and Larsen LB (2005) Wideband Measurements of Ice Sheet Attenuation and Basal Scattering. *IEEE Geoscience and Remote Sensing Letters*, **2**(2), 164-168

Paden JD (2006) Synthetic Aperture Radar for Imaging the Basal Conditions of the Polar Ice Sheets. Department of Electrical Engineering and Computer Science: PhD Dissertation, University of Kansas.

Paden J, Akins T, Dunson D, Allen C, Gogineni P (2010) Ice-sheet bed 3-D tomography. *Journal of Glaciology*, **56**(195), 3-11

Panzer B, Gomez-Garcia D, Leuschen C, Paden J, Rodriguez-Morales F, Patel A, Markus T, Holt B, Gogineni P (2013) An ultra-wideband, microwave radar for measuring snow thickness on sea ice and mapping near-surface internal layers in polar firn. *Journal of Glaciology*, **59**(214), 244-254 (doi: 10.3189/2013JoG12J128)

Paterson WSB (1994) The Physics of Glaciers, *Elsevier Science*, **3**

Pritchard HD, Ligtenberg SRM, Fricker HA, Vaughan DG, van den Broeke MR, and Padman L (2012) Antarctic ice-sheet loss driven by basal melting of ice shelves. *Nature: Letters*, **484**, 502-505 (doi: 10.1038/nature10968)

Proakis JG and Manolakis DG (1996) Digital Signal Processing, *Prentice Hall*, **3**

Rasmussen SO, Abbott PM, Blunier T, Bourne T, Brook E, and 19 others (2013) A first chronology for the North Greenland Eemian Ice Drilling (NEEM) ice core. *Climate of the Past*, **9**, 2713-2730 (doi: 10.5194/cp-9-2713-2013)

Rignot E (1996) Tidal motion, ice velocity and melt rate of Petermann Gletscher, Greenland, measured from radar interferometry. *Journal of Glaciology*, **42**(142), 476-484

Rignot E, Gogineni S, Joughin I, and Krabill W (2001) Contribution to the glaciology of northern Greenland from satellite radar interferometry. *Journal of Geophysical Research*, **106**(D24), 34007-34019 (doi: 10.1029/2001JD900071)

Rignot E and Jacobs SS (2002) Rapid Bottom Melting Widespread near Antarctic Ice Sheet Grounding Lines. *Science*, **296**, 2020-2023 (doi: 10.1126/science.1070942)

Rignot E and Steffen K (2008) Channelized bottom melting and stability of floating ice shelves. *Geophysical Research Letters*, **35**(2), L02503 (doi: 10.1029/2007GL031765)

Rodriguez-Morales F, Gogineni S, Leuschen CJ, Paden JD, Li J, Lewis CS, Panzer B, Gomez-Garcia Alvestegui D, Patel A, Byers K, Crowe R, Player K, Hale RD, Arnold EJ, Smith L, Gifford CM, Braaten D, and Panton C (2013) Advanced Multi-Frequency Radar Instrumentation for Polar Research. *IEEE Transactions on Geoscience and Remote Sensing* (doi: 10.1109/TGRS.2013.2266415)

Rott H, Rack W, Skvarca P, and De Angelis H (2002) Northern Larsen Ice Shelf, Antarctica: further retreat and collapse. *Annals of Glaciology*, **34**(1), 277-282

Schoof C (2007) Ice sheet grounding line dynamics: steady states, stability, and hysteresis. *Journal of Geophysical Research*, **112**, F03S28 (doi: 10.1029/2006JF000664)

Schmidt RO (1986) Multiple Emitter Location and Signal Parameter Estimation. *IEEE Transactions on Antennas and Propagation*, **34**(3), 276-280

Schultz BE, Zwally HJ, Shuman D, Hancock D, and DiMarzio JP (2005) Overview of the ICESat Mission. *Geophysical Research Letters*, **32**(21), L21S01 (doi: 10.1029/2005GL024009)

Shendkar TS, Sinmunic D, and Zentner R (2013) Comparison of DoA Estimation Algorithms in SDMA System. *Automatika*, **54**(2), 199-209

Shepherd A, Wingham D, Wallis D, Giles K, Laxon S, and Sundal AV (2010) Recent loss of floating ice and the consequent sea level contribution. *Geophysical Research Letters*, **37**, L13503 (doi: 10.1029/2010GL042496)

Shepherd A, Wingham D, and Rignot E (2004) Warm ocean is eroding West Antarctic Ice Sheet. *Geophysical Research Letters*, **31**, L23402 (doi: 10.1029/2004GL021106)

Ulaby F, Moore R, and Fung A (1986a) Microwave Remote Sensing: Active and Passive, *Artech House*, **2**

Ulaby F, Moore R, and Fung A (1986b) Microwave Remote Sensing: Active and Passive, *Artech House*, **3**

Vaughan RG, Scott NL, and White DR (1991) The theory of bandpass sampling. *IEEE Transactions on Signal Processing*, **39**, 1973-1984 (doi: 10.1109/78.134430)

Weedon WH, Chew WC, and Mayes PE (2000) A step-frequency radar imaging system for microwave nondestructive evaluation. *Progress In Electromagnetics Research*, **28**, 121-146

Wilhelms F (2001) Permittivity of ice core ngt37C95.2 from the North Greenland Traverse. *PANGAEA* (doi: 10.1594/PANGAEA.58022)

Zwally HJ, Schultz B, Abdalati W, Abshire J, Bentley C, Brenner A, Bufton J, Dezio J, Hancock D, Harding D, Herring T, Minster B, Quinn K, Palm S, Spinhirne J, and Thomas R (2002) ICESat's laser measurements of polar ice, atmosphere, ocean, and land. *Journal of Geodynamics*, **34**(3-4), 405-445